MICROSTRUCTURES AND MULTIFUNCTIONAL MICROSYSTEMS BASED ON HIGHLY CROSSLINKED POLYMERS

A Dissertation
Presented to
The Academic Faculty

by

Srikanth Singamaneni

In Partial Fulfillment
of the Requirements for the Degree
Doctor of Philosophy in the
School of Polymer, Textile, and Fiber Engineering

Georgia Institute of Technology
August 2009

MICROSTRUCTURES AND MULTIFUNCTIONAL MICROSYSTEMS BASED ON HIGHLY CROSSLINKED POLYMERS

Approved by:

Dr. Vladimir V. Tsukruk, Advisor
School of Polymer, Textile, and Fiber Engineering
Georgia Institute of Technology

Dr. Ken Gall
School of Materials Science and Engineering
Georgia Institute of Technology

Dr. Anselm Griffin
School of Polymer, Textile, and Fiber Engineering
Georgia Institute of Technology

Dr. Seung Soon Jang
School of Materials Science and Engineering
Georgia Institute of Technology

Dr. Yonathan Thio
School of Polymer, Textile, and Fiber Engineering
Georgia Institute of Technology

Date Approved: June 23, 2009

Dedicated to my dad, Venkateswarlu Singamaeni, who taught me the value of self-discipline and motivated me to get here today

ACKNOWLEDGEMENTS

Whenever I think of Prof. Vladimir Tsukruk and his impact on my life, I recall the famous Sanskrit sloka ***"Guru Bramha, Guru Vishnu, Guru Devo Maheswaraha"***, which says that Guru (mentor) is the highest cosmic principle and stands above the Brahma, Vishnu and Shiva (Hindu trinity) and that the teacher is God himself. Prof. Tsukruk gave me this valuable opportunity when I had no credentials, background or knowledge in the field of Materials Science and Engineering. I owe my life to this wonderful mentor, who nurtured creativity, raised curiosity, and fostered the desire to discover in me. I would also like to thank all the member of my committee for their valuable suggestions and comments on this work.

It is only because of the congenial environment and the helpful nature of all the members of SEMA lab that my PhD tenure has been effortless journey. I would like to thank former members of SEMA group, Dr. Jiang, Dr. Lemieux, Dr. Peleshanko, Dr. Ornatska, Dr. Ko, Dr. Lin, and Dr. Zimnitsky for their valuable guidance in the initial stages of my PhD. I am especially grateful to the current members of SEMA lab, Dr. McConney, Sehoon, Maneesh, Dr. Gunawidjaja, Dr. Kharlampieva, Kozlovaskaya, Whitney and Seth. I would like to thank our collaborators Prof. E. L. Thomas, Prof. M. C. Boyce, Dr. J.-H. Jang, Dr. K. Bertoldi from MIT and Dr. T. J. Bunning and Dr. R. Naik from AFRL. I would like to acknowledge the financial support from NSF and AFOSR for supporting this work.

Special thanks are due to my family without whose support this effort would not have been possible. It is difficult to express how grateful I am to my parents (Venkateswarlu and Padma) and my brother (Sridhar) for all the sacrifices they made to enable me have the best opportunities throughout my life. A special friend (who is also my wife) deserves unlimited credit for putting up with my emotions, endless love, and support. Finally, I would like thank my friends, Mr. Giridhar Vejendla, Dr. Sridevi Krishnamurthy and Mr. Somnath Metla for showing the beautiful colors of life.

TABLE OF CONTENTS

LIST OF TABLES

Page

LIST OF FIGURES

Page

LIST OF SYMBOLS AND ABBREVIATIONS

α	Linear thermal expansion coefficient
k	Spring constant
E	Elastic modulus

SUMMARY

In summary, work presented in this dissertation elucidates the novel physical and thermal properties of thin and ultra-thin films of crosslinked polymer and organized microstructures with a special emphasis on surface and interfacial effects and the structure-property relationships. Two major crosslinked polymer coatings have been thoroughly investigated: polymer microstructures fabricated by multi-laser interference lithography (IL), and plasma polymer coatings. We unveiled intriguing thermal properties of plasma polymer films originating from the physical state and exploiting the same for the design of ultrasensitve chemical sensors. The work emphasizes that the non-equilibrium state of the ultrathin films, which can be extremely powerful which can tapped for ultrasensitve sensors or actuators.

A novel paradigm of surface coatings, single and bi-component periodic, porous crosslinked polymeric structures, has been introduced and thoroughly studied. Surface, interfacial, and mechanical properties of these novel class crosslinked polymer coatings clearly demonstrate the enormous potential of the IL microstructures as organized multicomponent polymer systems. When subjected to external or internal stresses the periodic porous structures can exhibit a sudden and dramatic pattern transformation resulting in remarkable change in the photonic, phononic and mechanical properties of these structures. Furthermore, the confinement of these instabilities to localized regions results in complex hierarchical structures. The two polymer coatings (plasma polymers and IL microstructures) with complementary attributes (such as periodic structure, vertical stratification, residual internal stresses, and high surface and interface tunability) will enable us to understand and design novel multifunctional polymer coatings.

CHAPTER 1

INTRODUCTION

1.1 Background

Micro and nano electro-mechanical systems are gaining increased attention as a promising platform for ultrasentive physical, chemical and biological sensing. Demanding microscale applications involving microfabricated structures and microdevices incorporating polymeric materials require highly engineered surfaces and interfaces tailored to control surface elasticity, adhesion, friction, chemical, and thermal properties. Thus, coatings featuring designed multiphases are critical for many prospective applications in environmental monitoring, actuators, nanofiltration, unmanned vehicles, microsatellites, and other microelectromechanical systems.[1,2] Necessary smart coatings for these applications should include several design components which include surface mechanical, adhesive, and thermal properties. While the general principles of such coatings are well understood and exploited[3], the absence of well-defined shape and organization combined with a high level of spatial *polydispersity* (a wide distribution of geometries, sizes, and aggregation types) preclude the fine-tuning of the design of advanced multifunctional coatings.

Combining hard and soft polymer components provides multifunctional materials and coatings with synergetic properties and is frequently utilized for design of advanced polymeric composites.[4] For instance, a strong matrix serves as a load-bearing skeleton for structural integrity, while the soft component can be responsible for the adhesion control. As is known, to achieve proper multiphase structure in conventional composite materials, a complex monitoring of the kinetics of phase separation is required, combined with multiple processing stages (e.g.,

adding a new component). Although a certain control of spatial scale, morphology, microstructure, and shape is achieved with temperature-composition variation, the resulting composites usually possess high variations of feature dimensions, topology, and composition. These variations make it difficult to prevent a wide fluctuation of physical properties. While such a behavior affects the macroscopic properties of bulk composites, it can be even more critical for microstructural materials with dimensions comparable to the microphase domains (e.g., polymer MEMS).

Significant efforts have been made to design, prepare, characterize, and understand the structure-properties relationships of such stimuli responsive materials (SRM) in a bulk state or thin films either as ultrathin surface layers, or in free-standing state.[5,6,7] SRMs are defined as materials that undergo relatively large, reversible and *abrupt* physical, chemical, or structural changes in response to small external changes in the local environmental conditions.[8] It has been demonstrated that the reorganization of these materials on a molecular scale translates to dramatic changes in bulk and surface properties, thus, creating switchable, or responsive, materials with controlled wettability, mechanical response, heterogeneity, charge, adhesion, and chemical functionality, all of which can be potentially exploited for both sensing and microactuation.[9,10]

One of the important applications of the multifunctional polymer coatings is their deployment as sensitive layers in physical and chemical sensors. The typical design includes a transduction system functionalized with a sensitive layer, which exhibits a physical change in the presence of an external stimulus. The physical response of the sensitive layer is translated to readable signal by the transducer. Although there are several aspects that contribute to an efficient sensor system, the choice of responsive materials can help to optimize several key attributes critical for their ultimate performance, specifically high sensitivity, selectivity, fast response time,

and wide dynamic range. Due to their fast dynamics and substantial molecular mobility, macromolecular chains will sense, respond, and minimize the interfacial free energy with the local environment via structural changes in the backbone and side chains forming excellent choice as sensitive coatings. Adaptive and responsive soft materials with tunable properties that are readily controlled by environmental conditions (temperature, ionic strength, pH, electrical field) represent a critical, and now well-matured field in nanotechnology. These materials are considered outstanding candidates for assembling “smart” or “intelligent” active structures, and thus are instrumental for sensor designs which require an agile response to minute disturbances.

In terms of the coatings related to microsensor systems, some of the common issues reported to date for sensors are limited detection range, slow response time, long recovery period, and fast saturation (limited dynamic range). While the efforts so far have been primarily dedicated to fine tune the chemical attributes of the sensitive layers for enhancing the sensitivity and selectivity, we address the problem from a different view point. The physical properties (mechanical properties, interfacial adhesion, and residual stress) of the sensitive layers, which are often overlooked, are extremely important for multifunctional coatings. The sensor and actuation microsystems are only one of the many areas where the multifunctional coatings are extremely important. The ability to fine tune the surface mechanical and chemical attributes is expected to make a much broader impact in various areas of micro and nano electromechanical systems.

1.2. Materials

Two different classes of crosslinked polymers are investigated in the present study: photopolymerized (epoxy based polymer, SU8) and plasma polymerized. The chosen systems provide complementary abilities and properties to achieve a multifunctional coating platform. For example, photo polymerizable materials offer the ability to achieve unique structural organization by combining with conventional lithographic techniques while the plasma polymerization offers wide choice in chemical species that can be polymerized and excellent adhesion to a wide variety of substrates.[11]

1.2.1. Photo Polymerizable Materials

In general, photoresists that are used in conventional lithography can also be used for interference lithography as the process steps involved in both the techniques are essentially the same. They are usually divided into two groups: negative resists and positive resists. SU8 is a

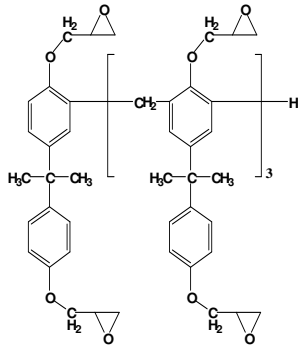

Figure 1.1: Chemical structure of SU8

popular epoxy type, near UV (365 nm) negative photoresist (chemical structure shown in Figure 1.1) in which the regions exposed to light become insoluble to the developer due to cationic photopolymerization. It has many advantages, such as chemical amplification, which increases

the sensitivity; mechanical robustness, which allows access to high aspect ratio structures; and wide processing latitude with respect to radiation wavelengths. This insolubility in the photoresists is usually achieved by either 1) an increase in molecular weight, or 2) photochemical rearrangement to form new insoluble products. To increase molecular weight, photo-initiators are generally used that can generate free radicals or strong acids to facilitate polymeric cross-linking or the photopolymerization of monomeric or oligomeric species. Without an increase in molecular weight, negative patterns can be achieved by the photochemical

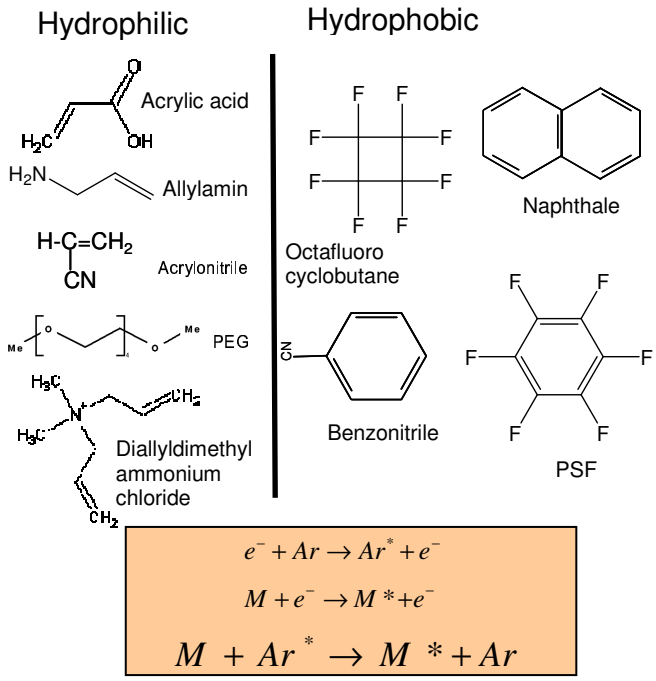

Figure1.2: Chemical structures of a few monomers amenable plasma polymerization. Summary of the chemical reactions in plasma polymerization

formation of hydrophobic or hydrophilic groups which provide differential solubility between the exposed and unexposed regions of the resist film.

1.2.2. Plasma Polymerizable Materials

Plasma vapor enhanced chemical deposition (PECVD) is an attractive method to fabricate thin solid films. The whole PECVD process is an economic, easy-to-control and room-temperature process, and does not use hazardous solvents. Plasma polymerization allows the deposition of ultra thin polymers films in a dry (solvent-less) process making it compatible with lithographic microfabrication methods, finding applications in sensing devices, MEMS, and optical devices, nanoscale photonics or as biocompatible interfaces. Plasma polymerization offers a unique advantage of the ability to polymerize almost any volatile monomers (few examples shown in Figure 1.2), some of which are impossible otherwise.

The chemical reactions during the plasma polymerization (shown in Figure 1.2) are significantly different from those observed in conventional polymerizations.[12] Excited species, free radicals, electrons and ions react with each other to produce high molecular weight and highly crosslinked network structures.[13] Furthermore, the composition and chemical structure of the PECVD products can be manipulated by suitable selection of both the initial monomers and the careful control of the processing conditions. [14] Due to their highly crosslinked structure, these films possess smooth surface and dense bulk morphologies, which results in robust mechanical properties and strong thermal, chemical and environment resistances. One of the special features of plasma polymerization is that these films can be coated on, and have very good adhesion to, a variety of substrates, including polymers, metals, and ceramics, with different geometries.

1.3. Polymer micro and nanostructures and hybrid functional systems

1.3.1. Ultrathin uniform polymer films

Ultrathin polymer films can be fabricated by a variety of techniques which include drop casting, spin coating, dip coating and polymerization on the substrate. Spin coating is a common technique which results in extremely uniform films (over few cm^2) over a wide variety of substrates. The thickness of the polymer films can be controlled (2 nm-few microns) by controlling the concentration of the solution, speed of rotation and the molecular weight of the polymer. On the other hand, polymerization of organic molecules on the surface of the substrate to form ultrathin films is another attractive technique. The thickness of the films is typically controlled by the rate of deposition and the deposition time. The physical properties of the films (such as elastic modulus, glass transition temperature, thermal behavior) critically depend on the type of deposition and thickness of the films.

Owing to the increasing applications of polymer films with nanoscale thickness, it is imperative to fully characterize the physical properties in these films, which could be significantly different from the bulk properties due to the surface and interfacial effects. Interactions with the substrate and high specific surface area (film/ air and film/substrate) can cause peculiar properties of the ultrathin polymer films.[15,16,17,18,19,20,21,22] In a recent study the glass transition of a free standing and supported PS film was found to vary significantly with thickness.[23,24] Other studies have unveiled several interesting phenomena such as the depth dependent glass transition temperature and thickness dependent thermal expansion. [25,26,27,28,29,30] It has been reported that substrate interactions alter the thermal properties of ultrathin poly-(2)-vinylpyridine films.[31] A non monotonic thermal behavior was observed in ultrathin polycarbonate films with a

negative and positive thermal expansion below and above glass transition temperature respectively.[32]

1.3.2. 2D and 3D periodic microstructures

Interference lithography (IL) is a technique that allows one to create 1D, 2D, and 3D periodic patterns by using coherent beams of light. The inherent periodicity present in the light is exploited to create structures using this technique. Essentially IL involves the formation of a stationary spatial variation of intensity created by the interference of two or more beams of light.

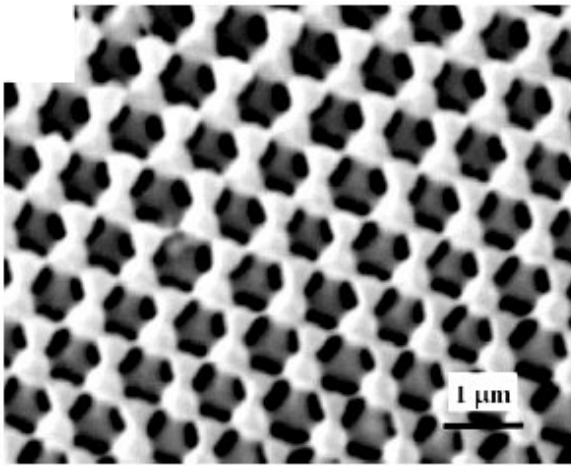

Figure 1.3: 3D periodic SU8 microframe with R3m symmetry fabricated by interference lithography

The pattern that emerges out of the intensity distribution is transferred to a light sensitive medium, such as a photoresist, to yield periodic structures. Figure 1.3 shows a periodic polymeric structure fabricated by IL technique. In general, the interference of *n* beams of coherent light results in *(n-1)* dimensional periodic patterns. The spatial variation of the intensity that determines a periodic structure is given by the equation below,[33]

$$I(r) = \vec{E}^2 = \vec{E} \cdot \vec{E}^* = \sum_{l=1}^{n} \sum_{m=1}^{n} E_l \cdot E_m{}^* \exp[i(k_l - k_m) \cdot r] \propto \sum_{l=1}^{n} \sum_{m=1}^{n} a_{lm} \exp[iG_{lm} \cdot r],$$

where E_i is the intensity of the beam, k_i is the wave vector, r is the position vector, a_{lm} is the Fourier coefficient and G_{lm} the Fourier expansion vector for a periodic structure. The pattern that emerges out of the intensity distribution is transferred to a light sensitive medium, such as a photoresist, to yield periodic polymer structures as was discussed in the materials section (Section 1.2.1).

1.3.3. Bimaterial Microsystems

In spite of the active developments of various transduction mechanisms, which include but are not limited to mechanical, electrical, optical, acoustic, electro-optical, and electrochemical methods, the field of sensor design and engineering has witnessed a continued search for the ideal signal transduction mechanism to maximize the transduction efficiency. While atomic force microscopy (AFM), introduced in the mid 80's, is an important milestone in nanoscience and technology, it also fueled a revived interest in microfabrication, and a plethora of applications of micromechanical structures.[34] AFM has long relied on MCs as transducers for its numerous imaging modes[35,36] including topographical, electric potential, magnetic, and force imaging. As a natural succession to their application as force transducers in AFM, MCs were selected as a new platform for transduction in sensing technology more than a decade ago.[37] Ever since, the technology has emerged to find important applications for MC-based sensors in chemical, biological, and thermal sensing.

There are a number of cantilever configurations (e.g., with and without intrinsic stress, silicon vs. polymer, “diving boards” vs V-shaped) designed for various applications (thermal sensing, IR sensing, chemical sensing, or biosensing). Within each sensing paradigm, there are different implementation principles - e.g., for chemical sensing, one can sense induced stress, weight change, reflectance change, and so on. The change of stress can be measured by piezoresistive elements, piezoelectric elements, MOS transistor, or light beam deflections, to name a few. The microscopic levers can be fabricated into various geometries with specific coatings using a vast range of semiconducting and metallic materials to optimize stiffness (kb/T noise), conductivity, reflectance, and Q factor. It is a huge challenge to cover existing accomplishments and future trends in a whole sub-field of microcantilever-based sensing. However, detailed discussion of the full range of possible cantilever designs is not the subject of this review. We focus mainly on materials aspect of their design which is critical for ultimate sensing applications.

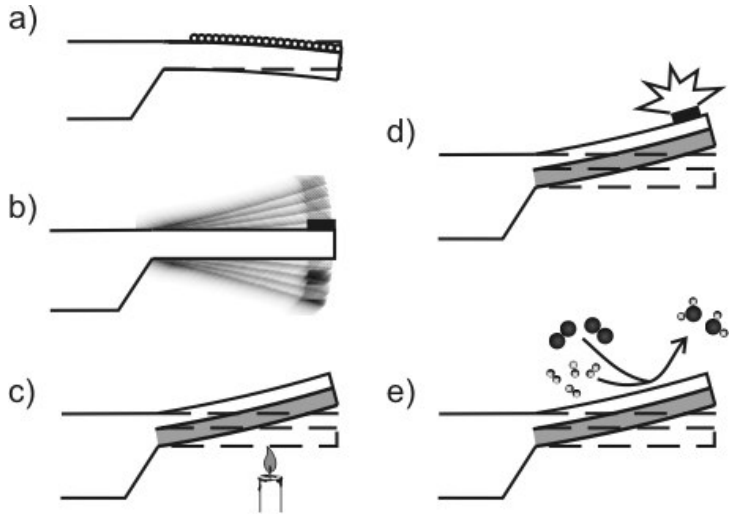

Figure 1.4: Schematic representation of various modes of operation of MCs: (a) Surface stress due to absorption of molecules causing static deflection; (b) Dynamic resonance frequency shift mode due to change in effective mass; (c) Heat sensing mode due to differential thermal expansion; (d) Deflagration of explosive on the heated MC surface; (e) catalytic reaction on the cantilever surface.

To provide sensing ability to microcantilever beams, their top and bottom surfaces must be coated in a chemically well-defined way to provide a functional surface capable of reacting with the target molecules and a passivated surface that will not significantly react with the target molecules thus creating differential stresses.

Basic modes of operation and detection:

There are two basic modes of operation of MC-based sensors namely, static (physical deflection of the MC) and dynamic (change in resonance frequency/phase) as well as several ways to initiate cantilever reaction such as, e.g., heat (deflection due to differential thermal expansion) or chemical reaction (Figure 1.4). In another example, adsorption of molecules onto the surface of the MC causes a bending due to increasing interfacial stress. Each mode differs from other in terms of the principle of transduction, functionalization, and detection mechanisms. Here we briefly introduce major modes of operation and highlight the design considerations specific to each mode.

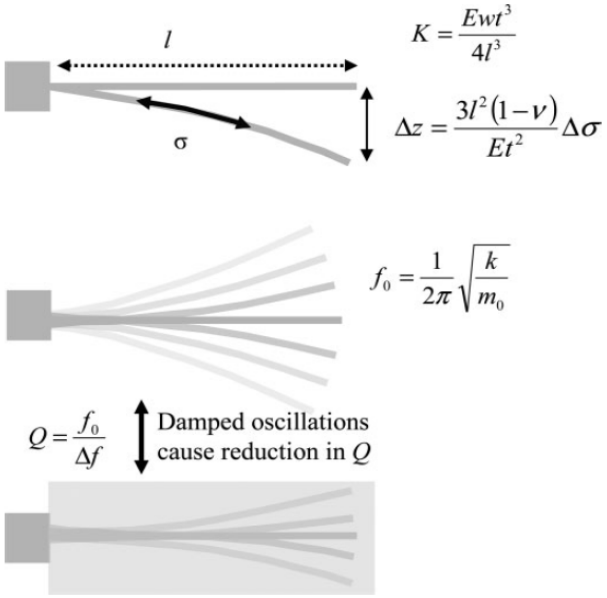

Figure 1.5: Schematic representation of MC deflecting in static mode under surface stress (a); MC oscillating at fundamental frequency f_o (b); and viscous damping for under-liquid operation (c) along with corresponding parameters.

The asymmetry of a functionalized top surface and a passivated bottom surface is especially important for the static deflection mode. The MC flexural behavior is controlled by the spring constant *k* of the cantilever, which is defined by material properties and MC geometrical dimensions. For a rectangular microcantilever of length *l*, thickness *t* , and width *w* , the spring constant *k* is calculated as follows:

$$k = \frac{Ewt^3}{4l^3} \qquad (1)$$

where *E* is Young's modulus (E_{Si} = 1.3 × 10^{11} N/m^2 for Si(100)). Typical spring constants for common MCs of several hundred micron length and a thickness below 1μm fall in the range of 0.001 to 0.1 N/m. Actual spring constants can be calculated and measured for various complicated shapes and compositions by using a range of theoretical and experimental approaches as has been discussed elsewhere.[38,39]

Assuming that uniform surface stress, $\Delta\sigma$ over the whole area of the cantilever is the cause for bending, the shape of the bent microcantilever can be approximated as part of a circle with radius R given by Stoney's equation [40,41]

$$\frac{1}{R} = \frac{6(1-\nu)}{Et^2}\Delta\sigma \qquad (2)$$

where *v* is the Poisson's ratio (v_{Si} = 0.24). For a given deflection, the surface stress change (schematically represented in Figure 1.5(a)) can be derived by using (2), which is however valid only for a surface layer much thinner than the beam itself (<20%).[40] There have been several attempts to modify Stoney's equation for thicker layers, the accuracy of which have been reviewed in a recent article.[42]

Static deflection operation (constant deflection at a given constant stress) is possible in various environments such as vacuum, ambient, and fluidic. In a gaseous environment, molecules adsorb on the functionalized sensing surface and form a molecular layer, provided there is affinity for the molecules to adhere to the surface. Static-mode operation in liquids, however, usually requires rather specific sensing layers, based on molecular recognition, such as DNA hybridization or antigen-antibody recognition as will be discussed below.

Polymer sensing layers frequently show a partial selectivity, because molecules from the environment diffuse into the polymer layer at different rates, mainly depending on the size and solubility of the molecules in the polymer layer. By selecting polymers expressing a wide range of hydrophilic/hydrophobic ligands, the chemical affinity of the surface can be manipulated to bind various molecules through intermolecular forces such as ionic bonds, hydrogen bonds and van der Waals forces.

By oscillating a MC at its eigenfrequency (f_0, the resonance frequency of an oscillating microcantilever is constant if its elastic properties remain unchanged during the molecule adsorption/desorption process and damping effects are negligible), information of adsorption or desorption of mass can be obtained under the prerequisite that the molecules on the surface might be in a dynamic equilibrium with molecules from the environment.

The corresponding mass changes can be determined by tracking the change in eigen frequency (Δf_0) of the microcantilever during mass adsorption or desorption (as shown schematically in Figure 1.5(b)). In this dynamic mode, MC is used as a microbalance, with added mass on the surface causing the resonance frequency to shift to a lower value. The mass change on a rectangular cantilever during molecular adsorption is related to the resonance frequency shift according to [43]

$$\Delta m = \frac{k}{4\pi^2 n} \times \left(\frac{1}{f_0^2} - \frac{1}{f_1^2}\right) \qquad (3)$$

where n is a geometric parameter and equals 0.24 for rectangular cantilevers and f_1 the eigenfrequency after the mass change.

Mass-change determination can be combined with variable but controlled temperature to facilitate "micromechanical thermogravimetry".[44] In the mass-balance mode, the sample under investigation is mounted at the apex of the cantilever, however, its mass should not exceed several hundred nanograms. In the case of adsorption or desorption (or decomposition processes), mass changes in the low picogram range can then be detected in real time.

Dynamic mode works efficiently in the gas phase where the quality factor remains virtually unchanged as compared to vacuum (the resonance frequency shifts by a few percents). However, in liquid environment, this approach suffers from substantial damping of the cantilever oscillation due to high viscosity of the surrounding medium increasing drag forces significantly (by several orders of magnitude). This damping results in a low quality factor $Q = \frac{f_0}{\Delta f}.$, where Δf is the full width half maximum of the frequency spectrum. The dramatic drop in the quality factor is usually observed from the typical range of 100-1000 in air to values below 50. Under these conditions, the resonance frequency shift is difficult to track with high resolution and thus the overall sensitivity decreases dramatically. While in air a frequency resolution of below 1 Hz is easily achieved for common cantilevers, resolution values of only about 20 Hz is considered very good for measurements in liquid environment. Moreover, in the case of damping or changes of the elastic properties of the cantilever during the experiment, e.g. stiffening or softening by adsorption of a molecule layer, the measured resonance frequency will not be

exactly the same as the eigenfrequency, and the mass derived from the frequency shift will be inaccurate.

A novel design for interrogation of solution eliminating these difficulties has been very recently reported by Burg et al.[45] The authors suggested the fabrication of the MCs with microfluidic channels embedded into the cantilever. The fluid continuously flowing through the channel to deliver the analyte species causes a change in the resonant frequency of the suspended microchannel due to binding of the analyte to the complementary species without compromising on the cantilever performance. A transient flow of the particle through the channel results in temporal dips in the resonance frequency depending on the position of the particles along the channel. An excellent quality factor of 15,000 was reported for a microresonator channel filled with water or air and the ability to detect single biomolecules and nanoparticles in fluid with a mass resolution reaching 300 attograms was demonstrated.[45] It is important to note that the typical quality factor for a MC submerged in liquid is more than two orders of magnitude smaller. This new design paradigm has the potential to significantly improve the applications of MCs for fluidic environment.

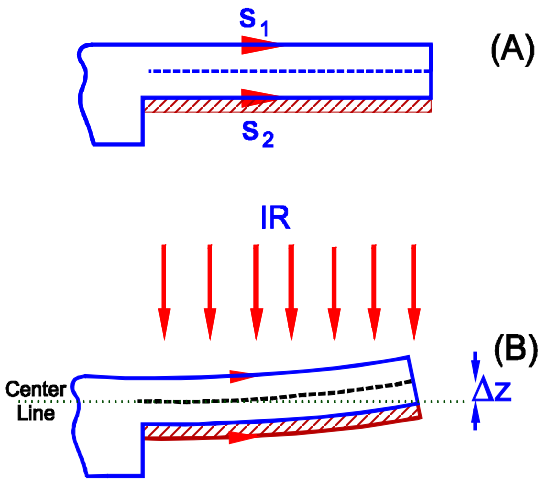

Figure 1.6: Schematic representation of the bimaterial structure applied for IR imaging: (a) bimaterial MC in rest; (b) static deflection of the MC due to the differential thermal expansion.

Bimaterial MCs comprised of two layers exhibit bending with change in temperature due to thermal expansion differences (Figure 1.6). This very well-known phenomenon is frequently referred to as the "bimetallic effect" and corresponding structures are called bimorphs.[46,47] In reference to the MC based sensors this mode of operation is frequently referred to as 'heat mode'.[37] Due to the differential thermal expansion, silicon nitride cantilevers, for example, with a thin gold film on one side undergo measurable bending in response to extremely small temperature changes due to the differential stress in the cantilever generated by dissimilar thermal expansion of the silicon nitride cantilever and the gold coating (Figure1.6).[15] Heat change can be either caused by external influences, such as change in environmental temperature (thermal detection), or occuring directly on the surface by catalytic reaction, or initiated by the thermal material properties of a sample attached to the apex of the cantilever (micromechanical calorimetry).

The steady state deflection of the tip of a bimaterial cantilever in response to a temperature change, ΔT, is given by [47]

$$\Delta z = \frac{3l_b^2}{t_1 + t_2}\left[\frac{\left(1+\frac{t_1}{t_2}\right)}{3+\left(1+\frac{t_1}{t_2}\right)^2+\left(1+\frac{t_1}{t_2}\frac{E_1}{E_2}\right)\left(\frac{{t_1}^2}{{t_2}^2}+\frac{t_2}{t_1}\frac{E_2}{E_1}\right)}\right](\alpha_1-\alpha_2)\Delta T \qquad (4)$$

where l_b is the bimaterial microcantilever length, t_1 and t_2 are the thickness of the coating and the microcantilever substrate, α_1 and α_2 are the thermal expansion coefficients of the coating and microcantilever, and E_1 and E_2 are the corresponding Young's moduli. As shown in Figure 1.6, Δz refers to the vertical deflection of the centerline of the microcantilever, at its outmost (right) end.

It can be concluded from Equation (4) that the Δz linearly depends upon difference in thermal expansion coefficients and temperature gradient. The deflection also can be maximized by designing MCs with proper geometry in addition to selecting appropriate bimaterial layers. Although the thickness of each layer as well as the overall length of the cantilever have a dramatic effect on the displacement magnitude, optimization of the cantilever design can not be achieved based on the condition of the maximum displacement alone. For example, the amplitude of cantilever deflection increases as the square of the bimaterial length, l_b. However, as the cantilever length increases so does the thermal noise which limits the achievable resolution. However, the best sensitivity of the cantilever heat mode is orders of magnitude higher than that of traditional thermal methods performed on milligram samples, as it only requires nanogram amounts of sample and achieves nanojoules[48] to picojoules[49,50] sensitivity.

Transduction mechanisms: A number of different phenomena acting concurrently might cause MC static and dynamic response. For instance, as was discussed above, differential thermal expansion of the cantilever substrate and coating layer results in the bending of the bimaterial

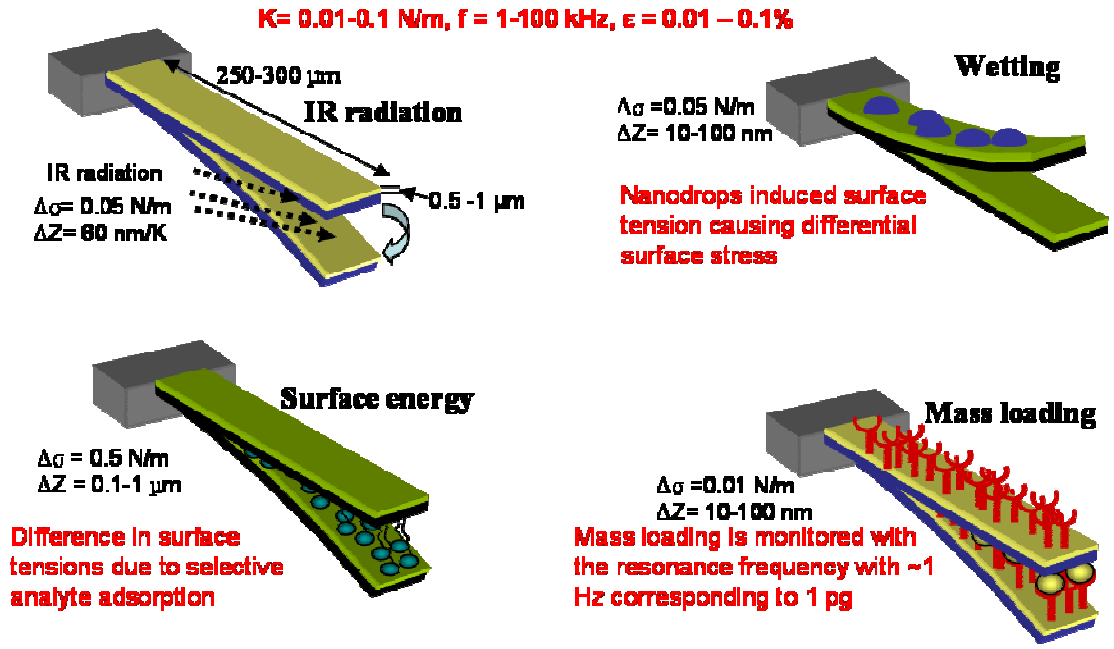

Figure 1.7: Schematic representation of the transduction mechanisms of MC based sensors with the typical range of the surface stress and the deflection achieved in each case for typical MC dimensions.

cantilever which can reach 60 nm per degree (Figure 1.7). However, the differential thermal expansion can be caused by other reasons such as radiation induced background heating or an exothermic reaction caused by analyte adsorption. Alternately, the changes of the differential surface energy can be caused by preferential adsorption of the analyte due to mass change without any reaction or the surface tension stress due to the liquid phase on one side of the cantilever (capillary phenomenon).

Here, we will briefly discuss the role and level of contributions in the cantilever bending of different factors. Figure 1.6 summarizes the most common transduction mechanisms with

typical attributes such as the stress and deflection of the MC or the resonance frequency shift. The estimation of the linear stresses developed and corresponding typical cantilever deflections have been estimated by using the Stoney's equation and literature data available.

In the capillary phenomenon, the liquid droplets adsorbed on the surface of the cantilever apply normal forces on the cantilever due to the vertical component of the surface energy of liquid-vapor interface. It has been recently experimentally demonstrated that the vertical component ($\gamma_{LV} \sin\theta$) of the surface energy, which is neglected for immovable surfaces in the Young's equation, can cause significant deflection of freely suspended structures but, generally, the static deflection caused by this phenomenon does not exceed 100 nm. [51]

The differential surface stress due to preferential adsorption of the analyte is the primary transduction mechanism for MCs functionalized with SAMs and metals where coatings have special affinity to the analyte molecules while the other surface remains largely insensitive to them. Differential stress can be as high as 0.5 N/m resulting in large static deflections approaching 1000 nm, both high values far exceeding any other contributions (Figure 1.7). Moreover, dimensional changes in the sensitive materials (e.g. polymer layers) due to the sorption of the analyte molecules termed as swelling or deswelling might result in even larger interfacial stress (as high as few MPa in some cases discussed below) in the bimaterial structure causing the bending of the entire structure by many microns clearly overshadowing other contributions.

Adsorption and desorption of the analyte on the surface and bulk of the functional coating result in change in the effective mass. The overall stress developed is not very high (below 0.01 N/m) and the deflection is modest (around 10 nm in most cases) and are difficult to detect (Figure

1.7). Biomolecular interactions (DNA hybridization, protein conformation changes, antibody-antigen interactions) also cause a shift in resonance frequency or cantilever deflection due to differential surface stress.[52] This deflection originates from osmotic pressure when biomolecules bind closely packed on one surface of the lever. Practical deflection measurements thus typically rely on high surface density of receptor molecules and close packing of bound analyte rather than on just added mass effect. The resonance frequency of the microcantilever decreases as mass is bound to the surface with typical sensitivity approaching 1 pg. Changes in resonance frequency are typically concurrent with deflection of the cantilever.

Numerous methods have been developed for the monitoring the MC deflection in context of their application as force transducers. The detection schemes employed can be classified broadly as optical (optical lever and interferometry) and electrical schemes (piezoresisitve, piezoelectric, capacitance, electron tunneling). The optical lever technique in which light is reflected from the back of the MC onto a position sensitive photodetector is similar to the readout scheme widely used in commercial AFM systems.[53] The deflection of the cantilever is thus translated in photodiode output voltage which, with proper calibration, can be converted into actual z-deflection. This technique, which offers a detection limit better than 1Å and is mainly limited by thermal vibrations, was successfully adapted for the detection of static and dynamic signals in MC based sensors. This method has been extended to cantilever arrays using multiple lasers.[54] Light from eight individual light sources can be coupled into an array of multimode fibers and guided onto the sensor array. Reflected light is directed to a position-sensitive detector (PSD) and the photocurrents are converted into voltages. In recent study, the eight light sources were switched on and off individually and sequentially detected by time-multiplexing.[55]

Apart from the disadvantages such as requirement of precise alignment, low opacity and low turbidity medium of operation, the primary drawback of this approach is the limited bandwidth which makes it extremely difficult to extend it to arrays of cantilevers and nanomechanical resonant structures. In contrast, optical interferometry offers higher bandwidth measurement and has been introduced as a MEMS-based technique which shows a great promise for the readout approach for large MC arrays. [56,57]

Piezoresistivity of a material (e. g. doped silicon) under external strain has been translated to monitor the deflection of the MCs. [58,59,60] Piezoresisitive detection method obviates the need for a complex alignment procedure which is often a serious problem in optical based detection methods. It is also important to note that piezoresistance method facilitates the measurement of huge deflections while the optical detection method is limited to a smaller range (typically few microns). However, in addition to the lower resolution (typically 0.5 to 1nm) compared to the optical technique, the primary disadvantage of the piezoresistive detection method is the continuous thermal drift due to the heat generated by the current flow through the piezoresistor on the cantilever which might interfere with the long-term stability of MC response.

The other important electrical method is the self-sensing piezoelectric cantilevers in which a piezoelectric material (such as ZnO) is deposited on the MCs.[61,62,63] This detection mechanism takes advantage of the piezoelectric effect, where a change in mechanical stress (cantilever bending) causes the induction of transient charges finally translated into a change in voltage. Although this approach offers freedom from the bulky optical instrumentation and inconsistencies of laser alignment, it requires additional steps in the fabrication process to integrate a piezoelectric material into the MC thus making microfabrication process more expensive and cumbersome.

Another approach of cantilever deflection, capacitance method, is based on the principle that the change in the distance between the capacitor plates which effectively changes the overall capacitance of the device. The deflection of the MC is measured by the changes in the capacitance between a conductor electrode and the MC substrate.[64,65] Despite its simplicity, this method suffers from undesired interference effects and the change in the dielectric medium between the capacitor plates which also changes the capacitance along with gradual discharge.

Very recently, Dravid and coworkers have introduced a novel method for the detection of the deflection of MCs where they have embedded a metal oxide semiconductor field effect transistor (MOSFET) in the base of the MC substrate.[66] The surface stress caused by the deflection of the MC results in an increase in the channel resistance due to the change in carrier mobility. Although the detection limit or maximum resolution (about 5 nm) currently achieved by the technique cannot even closely match that of the optical methods (<0.1 nm), the technique offers the unique advantage of obtaining arrays of MCs with built-in detection elements enabling seamless monolithic integration.

While soft materials are the best active sensing materials they do not always provide the best platform for microfabrication and miniaturization.[67] On the other hand, whereas semiconductors and metal oxides are the traditional active materials in sensing applications, they are not always versatile enough to provide multifunctional behavior. Conversely, inorganic materials are well established in microdevices and microfabrication. Incorporation of SRM into sensory systems brings a desirable diversity in signal transduction principles, tailorability, and multifunctionality that these traditional materials cannot offer. A combination of metal nanoparticles with responsive polymer shells, surface brushes, or multilayered layer-by-layer films was demonstrated to be prospective hybrid structures for sensing applications. [68,69,70,71,72,73,74,75,76,77]

Thus, hybrid structures, which consist of these two very diverse material components, should be considered as a strong design paradigm for responsive materials and structures.

Although most of soft-material based sensors exhibit performance, in terms of sensitivity, that surpasses that of sensors made of traditional inorganic materials, they have several drawbacks, currently limiting their usefulness for demanding sensing applications. The primary negative aspect of most of soft-matter-based sensors is the thickness of the sensing layer, which must be typically on the order of several micrometers to provide sufficient sensitivity. This exceeding dimension limits the incorporation of these sensing layers into micro and nano-scale sensors. Even the so-called "ultrathin" sensors still usually have 300+ nm thick films in the best (thinnest) cases.[78,79] Moreover, such coatings are commonly applied to electrodes [79] by a photo-patterning process that involves complicated photolithography.[80]

Besides the size, construction, and robustness issues, the traditional sensors are usually engineered to sense only one specific analyte or employ only one detection mode (either pH or humidity), and it is unclear whether they can be fabricated to be more diverse. Thus, these designs are typically "niche" sensors and are only useful if one specific type of response must be determined. However, in real-life applications with a number of external stimuli to be monitored, this is not practical. For example, weapons or threat sensing applications require a single sensor that can reliably sense several different gases and chemicals simultaneously and provide selective response. It is useless if a sensor reads "all clear" to VX nerve gas because it does not sense the thiolate group, but the user drops dead to mustard gas because the sulfonium salt that attacks the skin could not be detected. Clearly, sensors must be designed and fabricated to be as dynamic as possible, and capable of responding to diverse environmental stimuli.

In the last decade, MC-based sensors have proved to become a versatile tranduction platform for various physical, chemical, and biological sensors. The complementary signals obtained from MCs in the form of static deflection, resonance frequency shift, and change in the Q-factor enable unambiguos detection of trace amounts of organic vapors, explosives, chemical and biological warfare agents with extreme accuracy. Apparently, such a spur of activities and results needs to be systemized and evaluated.

Modification of MCs with thin polymer layers is probably the most common approach employed in applications involving chemical vapor sensing. Various methods such as drop casting[81,82,83,84], spin coating[85,86], inkjet printing[87], spray coating[88,89], capillary painting[90], plasma polymerization[91], *in situ* polymerization[92,93,94,95], *grafting to* via SAM functionalization[96], and matrix assisted pulsed laser evaporation (MAPLE)[97] have been adapted for modifying MCs.

While the response of the MCs coated from SAMs is due to the differential surface stress caused by changes in surface energy, the major contribution to the response of MCs coated with polymer layers is due to the solvation forces and swelling of the polymer layers. The sorption of the analyte molecules into the polymer film (swelling) results in relatively large differential stresses as compared with traditional SAM coatings. It is important to note that the magnitude of the response, the response time, and the selectivity of the MC sensors all scale with the thickness of the polymer layer. Various effects such as electrostatic, osmotic, solvation, and steric contribute towards the response of the polymer layers to the variable chemical environment. For instance, Thundat et al have demonstrated a humidity sensor based on silicon nitride MCs modified with hygroscopic phosphoric acid and 23 nm gelatin layers.[98] In the case of the cantilevers coated with phosphoric acid, the MCs exhibited a decrease in the resonance frequency with increasing relative humidity due to the increase in the effective mass of the MC. On the other hand, the gelatin coated MCs

exhibited an increase of the resonance frequency (explained as a change in *k* of the cantilever) correlated with a static deflection of the cantilever.

Drop casting, one of the most common methods for MC functionalization with polymer layers, involves micropipetting small droplets (few µl) of polymer solution on the cantilever and allowing solvent evaporation which leaves a thin polymer film on the cantilever. Although the technique is simple and easy to adapt, it provides almost no control over microstructure or thickness of the polymer film and hence results in poor reproducibility. Spray coating of the polymer solution also suffers from poor reproducibility and results in not very robust bimaterial MCs. Spin coating of the polymers usually results in uniform films with controlled thickness (optimized by the spinning conditions and concentration of the polymer solution). However, spin coating the cantilever with polymer layers usually causes an unwanted deposition on the passive side of the MC substrate reducing differential stress not to mention the potential damage of the MC. A two step process, spin coating followed by focused ion beaming etching, has been commonly adapted to functionalize the MC on a single side. Although the technique results in a single side coating of the functional layer, it is time consuming and costly and not suited for functionalizing arrays of MCs with different polymers.

As mentioned earlier, plasma polymerization is a solventless (dry) process, resulting in organic films with high solvent, scratch, and corrosion resistance combined with excellent thermal and chemical stability.[99,100] The underlying mechanism of plasma polymerization involves in organic species undergoing fragmentation in plasma, resulting in excited sub-monomer species, free radicals, and ions that can react with each other in the plasma zone, or at the nascent surface layer. Depending upon parameters, these species can remain in a charged state inside the layer (charged polymer layer) or bond to each other to produce highly crosslinked organic films.[101] Plasma polymerization offers the unique advantage of being able to polymerize numerous organic species, such as

saturated alkanes, unsaturated alkenes, thiophenes, siloxanes, and fluorocarbon compounds. It is worth to note that many of the resulting chemistry of these coatings are unique and often impossible to fabricate by traditional wet chemistry techniques.

Obviously, to retain the bimaterial-induced bending effect, the plasma polymerization must be controlled so that only one side of the MC is modified. This can be done in single step, in-vacuum process, as opposed to the conventional wet-fabricated coatings discussed earlier. One of the other advantages of the plasma polymerization technique is the excellent adhesion of the coatings to numerous substrates, which is highly desirable for stress transfer to the MC. The physical properties of the plasma polymerized organic films, such as the degree of crosslinking, the elastic modulus, internal (residual) stress, thermal expansion, adhesion, and surface morphology can be controlled by adjusting deposition parameters.[102] This control includes rate of deposition of the monomer, power of plasma source, pressure in the chamber, and flow gas type and rate, as have been comprehensively reviewed by Yasuda. [103]

Selection of the responsive polymer coating which is highly sensitive and selective (at least partially) is the most important design criterion of polymer based MC sensors. It is important to note that selectivity, response time, and reversibility are dictated by the thermodynamics and kinetics of the responsive material interacting with the analyte molecules, which frequently leads to a compromise between high selectivity, typically associated with strong interactions, and complete reversibility requiring weak interactions. Although no systematic studies on this subject exist in the context of MC based sensors with various polymeric coatings, significant efforts in understanding the correlation between the analyte origin and the polymer coating has been done for popular piezoelectric devices such as surface acoustic wave (SAW) microsensors and thickness shear mode (TSM) resonators.[104,105]

For instance, the partition coefficient which is defined as the ratio of the concentration of the solute (analyte molecules) in the sensitive coating to the concentration of the analyte in the vapor phase is the single most important parameter in the selection of the sensitive layer in these sensors. Indeed, experimental results prove that the shift in the resonance frequency of the SAW devices is directly proportional to the partition coefficient. [106] Linear solvation energy relationship (LSER) has been applied to compute the partition coefficients of the analyte/coating layer by taking hydrogen bonding, dipolarity, polarizability and dispersion effects into account thus providing a rich database for selection. [107,108] The readers are referred to an excellent review on the subject for further insight. [109]

It is reasonable to suggest that the design principles established in these gravimetric devices can form good initial guidelines for designing MC based sensors; however, care should be taken while adapting these material selection schemes without modification. For example, it is known that elastomeric materials are advantageous compared to glassy materials in SAW devices due to the better reversibility and faster responsive time. It is also known, however, that the higher the elastic modulus of the coating layer the greater the differential stresses and thus higher static deflection in MC based sensors making elastomeric materials not very suitable for bimaterial designs with high sensitivity. Thus, for bimaterial MCs, structure design rules need to be optimized in accordance to the specific requirements.

It is also important to remember that the magnitude of the response, the response time, and the selectivity of the MC sensors inevitably scale with the thickness of the coatings. In recent study, Betts et al. have addressed the issue of the sensitivity and selectivity of MCs coated with poly(cyanopropylsiloxane) (SP-2340) of different thickness.[110] The authors have observed a general trend of decreasing signal to noise ratio (SNR) for various organic vapors with increasing film thickness. The selectivity factor defined as the ratio of the response to analyte

vapor to a standard interfering vapor (pentane in this case) exhibited a modest increase (50%) as well when thickness was increased from 50 nm to 100 nm followed by a slight decrease for thicker coatings. Even more recently, Lochon et al have shown that the sensitivity (measured in terms of a frequency shift) of poly(etherurethane) coated MCs increases linearly with thickness of the coatings (1-20 μm).[111] However, the thermal noise of the MCs also increased significantly for MCs with the thicker coating making the detection limit to stay constant or even worsening with the increase in the coating thickness. Moreover, they have also shown that the increase in the coating thickness causes an increase in the response time, a highly undesirable output. In other study, Zhao et al have reported the coating thickness dependence of PS coated MC bimaterial structures.[112] They have shown that the interfacial tension, which remains constant for coatings with different thicknesses dominates the thermal response of the bimaterial MCs for thinner coatings (<20 nm) while for higher thickness the thermal expansion coefficient dictates the resulting static deflection.

CHAPTER 2

GOALS AND OBJECTIVES

2.1 Goals

Goal of the work presented in this dissertation is to elucidate the novel physical and thermal properties of thin and ultra-thin films of crosslinked polymer and organized crosslinked polymer microstructures with a special emphasis on surface and interfacial effects and the structure-property relationships of these nanoscale structures (Figure 2.1). The acquired knowledge

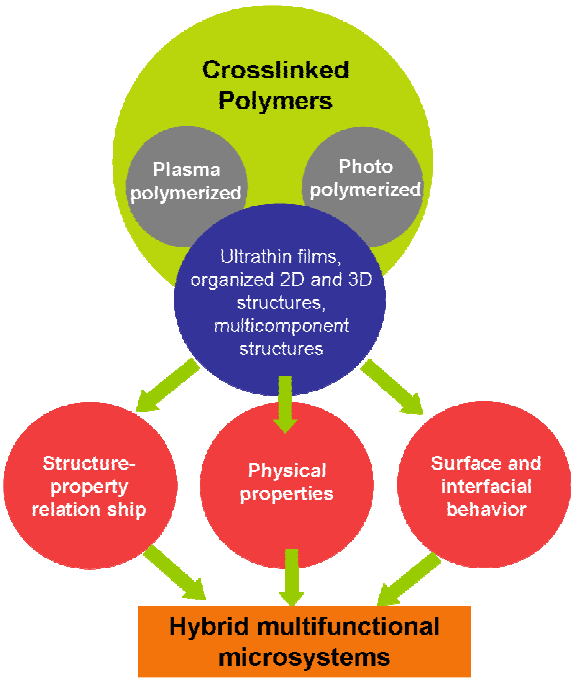

Figure 2.1: Summary of the intermediate and final goals of the study

might be applied to develop a functional microsensor system based on organized crosslinked polymers. In this study, we focus on two major crosslinked polymer coatings: polymer microstructures fabricated by multi-laser interference lithography (IL), and plasma polymer coatings. The two polymer coatings with complementary attributes (such as periodic structure,

vertical stratification, residual internal stresses, and high surface and interface tunability) will enable us to understand and design novel multifunctional coatings.

The key technical objectives are summarized as follows:

- Fabrication of ultrathin crosslinked polymer films using plasma polymerization and interference lithography and investigation of mechanical and thermal properties.
- Interference lithography microfabrication of thin (few microns) polymer coatings with different geometries from hard (glassy) and compliant (rubbery) polymeric materials on various relevant substrates (silicon, glass, polymers) using direct chemical grafting.
- Study the role of internal stress and interfacial effects on the physical properties of ultrathin polymer films.
- Develop routines to fabricate organized bicomponent coatings combining a strong skeleton with a second soft phase such as elastomeric rubbers, hydrogels, and solid or fluidic lubricants.
- Comprehensive characterization of the bicomponent polymer coatings and their surface and interfacial properties using a range of analytical, surface, scattering, and microscopic tools.
- Understanding nano-micro-macroscale mechanical properties of polymer microstructures of different types and spatial scales by combining surface force microscopy, buckling testing, tensile and shear measurements in conjunction with finite element analysis modeling.
- Demonstrate the feasibility of exploiting the polymer coatings to design and implement functional microsystems such as highly sensitive sensors and actuators.

2.2 Overview

The work presented here unveils the novel physical and thermal properties of crosslinked polymer thin and ultra-thin films and organized crosslinked microstructures with a special emphasis on surface and interfacial effects and the structure-property relationships. The unique

physical properties of the ultrathin crosslinked polymers was used develop a functional microsensor system based on organized crosslinked polymers. In this study, we primarily focused on two major crosslinked polymer coatings: polymer microstructures fabricated by multi-laser interference lithography (IL), and polymer coatings obtained using plasma polymerization. The two polymer coatings with complementary attributes (such as periodic structure, vertical stratification, residual internal stresses, and high surface and interface tunability) will enable us to understand and design novel multifunctional coatings.

A comprehensive and critical review of the literature relevant to the field of multifunctional polymer coatings and microcantilevers based sensors is presented ***chapter 1***. The chapter highlights the state of the field and issues which remain unresolved and which need further investigation.

The current chapter (***Chapter 2***) describes the goals and specific technical objectives the work discussed in this dissertation. It also provides an overview and organization of the entire dissertation.

C***hapter 3*** describes the key experimental techniques employed to study the structural, physical, chemical and sensing properties of the various material systems investigated. The chapter describes fabrication techniques such as plasma polymerization and interference lithography and characterization techniques, namely, atomic force microscopy including the surface force spectroscopy, ellipsometry, and confocal Raman microscopy. Apart from this discussion of the general techniques, each chapter includes an experimental section which describes the specific experimental routines employed for the particular study.

Chapter 4 describes an unusual thermal behavior of ultrathin plasma-polymerized polymer films deposited on silicon wafers. We have observed various intriguing features in the thermal behavior of ultrathin plasma polymer films such as non-linear thermal expansion and hysteresis between the heating and cooling cycles. Furthermore, a large, reversible negative thermal expansion of plasma polymerized polyacrylonitrile (ppPAN) and polytrimethyl silyl acetonitrile (ppPTSA) in the normal direction was observed. This unusual negative thermal expansion (NTE) behavior is suggested to be caused by the presence of high residual stress in the polymer film, which is common for plasma polymerized materials combined with developed grainy surface morphology. The residual stresses arise because of the wedging effect during the deposition process, where the high-energy fragments wedge in the existing film. In fact, for some plasma-polymerized polymers, we estimated in-plane compressive stress to be as high as 50 MPa, which is close to/exceeds the yield strength of polymeric materials. These large residual stresses in the plasma polymers are extremely useful for creating a microsystem with latent energy which can be employed for rapid and large response to external stimuli (discussed later).

In next level of complexity, we have investigated the physical properties of organized single and bicomponent crosslinked microstructures, which are described in ***chapter 5***. The crosslinked microstructures are fabricated using multi-laser beam interference lithography (IL). The microstructures exhibit unique length scale dependent mechanical properties due to the intermediate croslinking density and nanoscale dimensions of the struts. In order to create organized bicomponent structures from the microstructures obtained IL technique, we have investigated two independent techniques, namely, capillary assisted infiltration and *in situ* polymerization. AFM imaging and nanomechanical measurements on the SU8-PB binary microcomposites confirmed the templated periodic distribution of the glassy and rubbery microphases. The unique feature of the organized glassy/rubbery structures is that the crack

follows the selected lattice direction fracturing the PAA phase inside of cylindrical pores. Indeed, in the case of the randomly distributed rubbery microphases, there are multiple random pathways in which the crack can propagate through glassy phase dissipating the least amount of mechanical energy and causing the macroscopic failure of the random microstructure. In contrast, for the organized bi-component rubbery-glassy structures discussed here, the crack's pathway through the rubbery-filled pores is predetermined by the matrix symmetry (square lattice in this case), which could possibly maximize energy dissipation during crack propagation. Such organized glassy-rubbery microcomposites fabricated with IL can find novel high-demanding applications, which require precise control of the mechanical elastic and plastic behavior at micro and nanoscale.

In the process of fabrication of organized glassy/rubbery structures, yet another intriguing observation is the mechanical instabilities in the periodic porous crosslinked microstructures which are summarized in ***chapter 6***. The onset of buckling instabilities during the polymerization of additional rubbery component inside cylindrical pores leads to a dramatic pattern transformation. Owing to the elasto-plastic nature of the porous structure, the transformed pattern is frozen and stable as opposed to the elastomeric counterparts, which return to the pristine structure once the external pattern is removed.

Furthermore, localized polymerization of acrylic acid within cylindrical pores resulted in confined mechanical instabilities leading to a complex hierarchical porous structure comprised of regularly collapsed pores with alternating orientation. Moreover, we have observed a controlled transformation when the polymerization can be confined in two dimensions to highly localized areas which include only two to three neighboring pores. On the other hand, complete transformation with highly collapsed pores can be achieved when the transformation is confined

in only one dimension. We have also demonstrated the replication of the topographical features of the transformed pattern in other polymers using the CTL process.

The acquired knowledge of the crosslinked polymer sytems was employed to design a microcantilever based chemical sensor discussed in ***chapter 7***. The latent energy of the plasma polymer stored as residual stress was exploited for large bending of the bimaterial microcantilever. In the best example, plasma polymerized methacrylonitrile coated silicon cantilever exhibited a deflection of nearly 200 µm for a 60% change in relative humidity enabling a resolution of 0.00005% RH. There are several factors that contribute to the outstanding response of our cantilevers, including the unique nanoporous morphology, minute thicknesses, crosslinked nature, and the strong interfacial adhesion of these nanocoatings.

CHAPTER 3

EXPERIMENTAL DETAILS

This chapter is intended to give a general overview of the experimental technique, procedures, and equipment that were utilized throughout the work presented here. Specific experimental techniques are detailed in each of the individual chapters. After explaining general sample preparation procedures, overviews will be given of the characterization equipment and procedures.

3.1. Synthesis and Fabrication

3.1.1. Plasma polymerization

All the monomers (styrene, acrylonitrile, methacrylonitrile, naphthalene etc) are purchased from

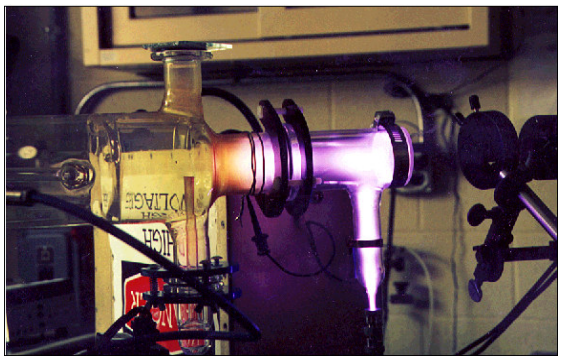

Figure 3.1: PECVD facility at WPAFB specially designed for deposition of organic species.

Aldrich (purity greater than 99%), and are directly used for the plasma polymerization. The PECVD chamber (in Dr. Timothy J. Bunning's lab at Wright-Patterson Air Force Base (WPAFB)) is custom built (shown in Figure 3.1).[113] Argon (50-200 cm^3/min, 99.999%), used as the noble

gas for generating a plasma, flows into a 10-cm diameter reactor at 0.02-0.5 Torr vacuum through a capacitively coupled radio frequency (RF, 13.56 MHz) discharge of 20 to 45W power.

The plasma density is controlled to approximately 108 cm^{-3} in the afterglow region. The precursor gas/vapor is added 10 cm downstream from the plasma generation zone. The substrate is located about 1-3 cm further downstream from the precursor inlet. The distance between the substrates and the inlet of precursor materials can be changed as per the requirements. Precursor flow rates of 0.5 and 1.125 cm^3/min are utilized for the coatings.

3.1.2. Interference lithography

2D and 3D patterns are fabricated using multi-beam holographic interference lithography using

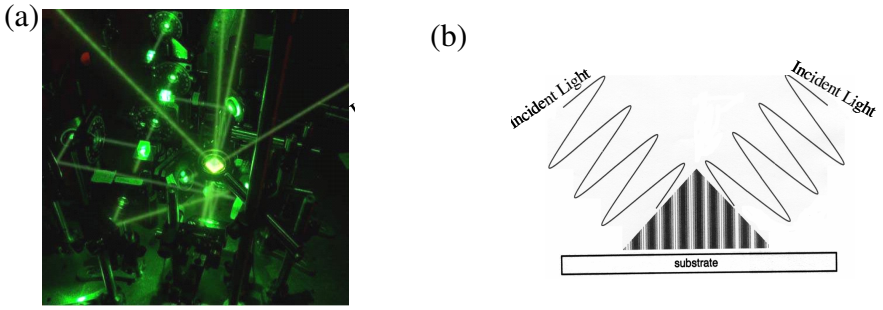

Figure 3.2: (a) Multiple laser beam setup at MIT and (b) Schematic of IL photopatterning.

the setup in Prof. Edwin L. Thomas' lab at MIT.[114,115] The fabrication procedure involves the interference of three equal intensity laser beams and the transfer of the resultant intensity pattern into an SU8 photoresist platform via laser-initiated cationic polymerization (Figure 3.2). The materials platform consists of Epon-SU8 (Shell) as a photoresist (a multifunctional epoxy derivative of a bisphenol-A Novolac), cyclopentanone (Aldrich) as a solvent for spin-on of the film, rubrene (Aldrich) as a photosensitizer which absorbs the visible light and electron transfers to an onium salt, octoxyphenylphenyliodonium hexafluoroantimonate (OPPI) (UCB Radcure) as

a photoacid generator, and tributylamine to compensate the non-zero background of the interference intensity. These compounds are first dissolved in cyclopentanone and then mixed with SU8 in a weight ratio of rubrene:OPPI:SU8=0.2:2:100, respectively. To increase the adhesion between the glass substrate and SU-8 layer, a 1 μm thick buffer layer of SU8 is spin-coated (2,000 rpm, 1 min) and baked (5 min, 95℃). It is then flood-exposed under the UV lamp and hard-baked at 180℃ for 15 min. This layer effectively improved adhesion of the patterned SU-8 layer to the substrate and prevented delamination during the developing process.

Next, the SU-8 solution in cyclopentanone is spin-coated on top of this existing SU-8 film at a spin speed of 1000 rpm. The coated photoresist is then soft baked at 95ºC for 10 min. The exposure is done using a 532 nm Nd:YAG laser with an intensity of 0.3 W for 10 seconds to give a total exposure dose of 5-10 J/cm^2 over areas with diameter larger than 4 mm (setup at Prof. Edwin L. Thomas Lab, MIT shown in Figure 3.2). After baking the film at 65 ºC for 5 min, the resultant cationic photopolymerization only takes place in regions that are exposed to high intensities of light. The uncured regions are developed away in PGMEA (propyleneglycol monomethylether acetate) and the film is finally rinsed with isopropyl alcohol to yield the 2D porous photopatterned structure.

3.1.3 Bimaterial microcantilevers

Microcantilevers and a corresponding large silicon wafer are coated simultaneously for each deposition condition. The microcantilevers (MicroMasch USA) are rectangular shaped with the following dimensions: L = 300μm; W= 20μm; T = 0.7 – 1.3μm as verified by SEM. The tips are either bare silicon, or silicon with a 60 nm Au layer. Spring constants varied from 0.01 to 0.2 N/m, measured by tip on tip method.[116] The cantilevers are mounted on a silicon wafer, and placed in the PECVD reaction chamber so that only one side of the cantilever was coated.

3.2. Characterization techniques

The research involves in the application of a wide range of characterization techniques for the comprehensive study of the relevant physical and chemical properties. Chemical composition of the plasma polymerized films was probed using Fourier transformed infrared spectroscopy performed using a Perkin-Elmer Spectrum 2000 FT-IR spectrometer in transmission mode. Contact angle measurements were performed on various crosslinked polymer surfaces using KSV CAM 100. Optical images of the microcantilever deflections were obtained using a Leica MZ16 microscope in reflection mode. Some of the techniques which are specific to the current research in that they are either custom built or tailored for specific requirements will be briefly described.

3.2.1. Ellipsometry

Ellipsometry was performed using spectroscopic ellipsometer M2000U (Woolam). Ellipsometry is a non-destructive optical technique, which deals with the measurement and interpretation of changes of the polarization state of polarized light undergoing oblique reflection from a sample surface.[117] The quantities measured by an ellipsometer are ellipsometric angles Ψ and Δ which are related to the complex ratio of the Fresnel reflection coefficients R_p and R_s for light polarized parallel (p) and perpendicular (s) to the plane of incidence such as

$$\rho = R_p / R_s = \tan \Psi \exp(i \Delta) \qquad (3.1)$$

The complex reflectance ratio ρ is completely determined by an amplitude ($\tan \Psi$) and a phase (Δ).[118,119] These changes are related to a transformation of a shape and orientation of the ellipse of polarization, respectively. In order to deduce unknown parameters of a sample under investigation, a model for the sample structure is first constructed with initial estimates of the parameters. These parameters (e.g. thickness and refractive index) are then varied to generate

a set of calculated Ψ^{exp} and Δ^{exp}. The initial parameters of the model parameters are transformed finally into true parameters of the sample, such as thickness and optical constants.

Because of the high accuracy of ellipsometry to measure thin film thickness (within ±0.1 nm from the same location), this technique is used to measure the linear thermal expansion coefficient of organic thin films. In this case, the sample is mounted on a heating stage that is placed on the Ellipsometer stage. The sample is heated, allowed to equilibrate for 10-20 minutes, and the thickness is measured, and this is repeated at each temperature interval. The expansion coefficient (α) is then obtained with the usual formula: $\alpha = L_0\Delta T/\Delta T$. Each value of α obtained by this method was obtained from averaging three cycles together, only after the sample was annealed for 24 hours at 50° - 100°C in a vacuum oven.

3.2.2. Scanning Electron Microscopy (SEM)

A field-emission scanning electron microscopy (FESEM, LEO 1530) was used to investigate the morphology of the pristine and transformed morphologies of the microframe structures. For SEM, the samples were mounted on SEM stubs by using conductive carbon tape and gold sputtered (5-10 nm). The typical operating voltage was maintained between 5-7 KeV.

3.2.3. Atomic Force Microscopy (AFM)

The morphology and nanomechanical properties of various organic and inorganic surfaces with nanometer resolution have been obtained using both the Dimension 3000 and the Multimode microscopes (Veeco Inc., Santa Barbara). The key element of AFM is the ultrasensitve force sensor, which is a microcantilever with a sharp tip that deflects when interacting with the surface of the sample. This deflection is detected by either optical (photodiode, interferometer) or electrical (capacitance, tunneling) methods. The result is a three-dimensional map of the sample surface with nanometer resolution allowing for quantitative analysis of the surface

roughness.[120] The topographical imaging can be performed in various modes which include contact, tapping and non-contact modes.

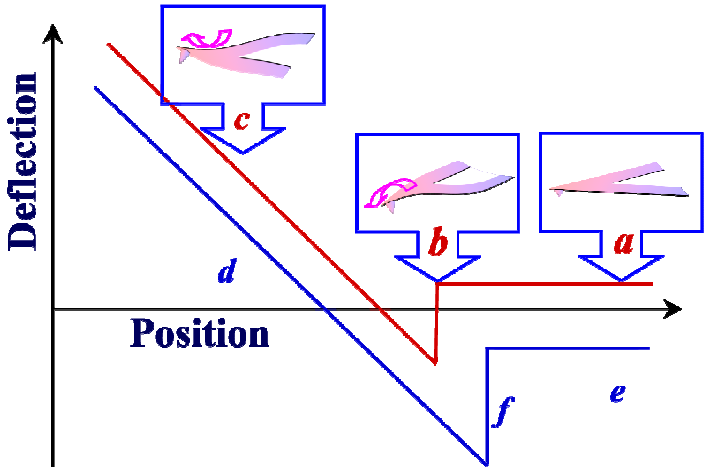

Figure 3.3. Components of an FDC: Segment (a) the tip approaches the surface; segment (b) is the jump to contact on the surface; during segment (c), the upward deflection of the tip is occurring from pressing on the surface; withdrawal of the tip takes place during (d). If both (c) and (d) are not straight, plastic and elastic deformation behavior can be arrived at. Finally, at segment (f), the tip snaps out of contact with the surface when the restoring forces of the cantilever exceed the adhesion between tip and sample.

Tapping mode AFM allows for the high resolution imaging of soft polymeric and biological samples without damage to tip or sample since contact with the surface is minimized. This is achieved by using specially designed probes that oscillate above the surface at their resonant frequencies of 100 – 500 kHz (typically ~300 KHz).

Apart from high resolution topographical imaging, probing the nanomechanical properties with unprecedented spatial resolution is another unique capability of AFM that has been extensively here. The technique, termed as surface force spectroscopy (SFS), involves in elastically indenting and retracting the AFM tip into the surface for quantifying adhesion and elastic properties of heterogeneous surfaces of polymer layers on the nanoscale.[121, 122] This mode utilizes the force distance curve (FDC) (Figure 3.3) of the AFM.[123] A single FDC records the

forces felt by the tip as it approaches to and retracts from a point on the sample surface. SFS allows a 16 x 16, a 32 x 32, or a 64 x 64 array of FDCs at unique XY coordinates over a pre-set sample area.[124] Thus, it essentially is a series of elastic indentations into the polymer layer. This allows for mapping of the mechanical properties (adhesion, elastic modulus) of polymer surfaces with nanometer scale resolution, while obtaining topographical information simultaneously. The applied normal load and speed of the nanoindentations are critical parameters to control in force volume.

Data collected is processed using a micromechanical analysis (MMA) software package developed in our lab, which provides means for calculation of localized elastic modulus, depth profiling of the elastic modulus, adhesive forces, and surface histograms of elastic moduli and adhesive forces from experimental images as described elsewhere.[125] The MMA utilizes Hertzian, Johnson-Kendall-Roberts (JKR), and Sneddon models of solid contacting bodies to derive this data. For absolute quantitative results of the adhesion and elastic modulus from force volume data, the normal spring constant of the cantilever as well as the radius of the tip are extremely critical. Spring constants of cantilevers are determined by tip-on-tip method in which a series of force curves are obtained by pressing the cantilever with unknown spring constant against a cantilever with known spring constant.[126, 127] Tip radii are evaluated by scanning a reference gold nanoparticle specimen in combination with deconvolution procedure also included in the MMA software.[128, 129]

3.2.4. Chemical sensing measurements

To test the response of the microcantilever sensors to water vapor, the sensors are placed inside an environmental chamber in which humidity content could be controlled within 0.1% ('control' sensor mounted inside the humidity box) and the setup for humidity monitoring (as shown in Figure 3.4).

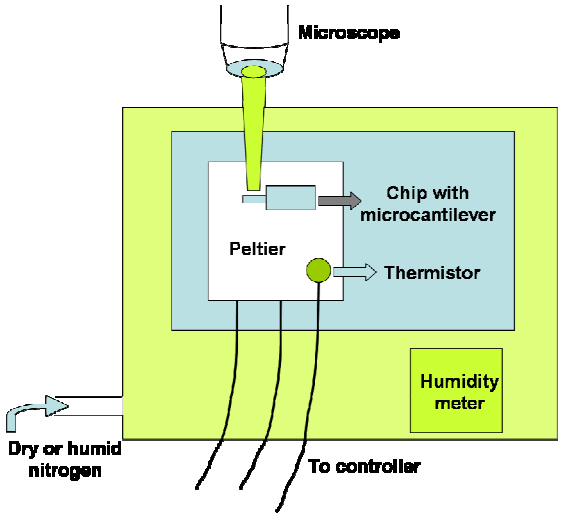

Figure 3.4: Schematic of the environmental chamber employed for chemical sensing.

At the bottom of the Plexiglas chamber, an inlet valve allowed the controlled flow of water vapor by bubbling dry nitrogen through a glass bubbler containing roughly 50 mL of distilled water. The humidity sensor inside the chamber constantly monitored humidity, and the optical microscope recorded images at different humidity ranging from 5 – 70% relative humidity (RH). An AFM (Nanoscope IIIa-Multimode) optical photodiode detection system is utilized to monitor the response of the sensor for small changes in humidity. The photodetector is calibrated through the standard method of fitting curves performed on piranha cleaned <100> silicon. For this experiment, the AFM scanner is enclosed in a chamber and the humidity in the chamber was altered as mentioned earlier. For measuring the dynamic response of the sensors the humidity is cyclically varied is the chamber and the deflection of the cantilever is recorded. The response of the cantilever was recorded using optical microscope at a rate of 30 frames/sec. For experiments involving the detection of naphthalene and hydrazine vapors, the cantilevers are exposed to saturated vapor of the desired chemical.

3.2.5. Confocal Raman microscopy

Raman spectroscopy is a unique non-destructive technique for probing the chemical composition, internal stress, electronic structure of a material. The technique has been widely used for mapping internal stresses in materials such as silicon, carbon nanotubes.[130,131] Raman measurements were performed using a Witec (Alpha 300R) confocal Raman microscope using Ar+ ion laser (λ= 514.5 nm) as excitation source. The intensity of the excitation source was fixed at 4 mW. Raman imaging of the samples was performed using a 600 grooves/mm grating with a resolution of ~3 cm^{-1} or with 1800 grooves/mm grating with a resolution of 1 cm^{-1}. The typical imaging was performed at a resolution of 50×50 pixels unless mentioned otherwise, with each spectra collected for 0.7 sec. The short collection interval used here eliminates the possibility of laser induced heating. The individual spectra were always collected locally over a longer time using 1800 grooves/mm grating with a resolution of about 1 cm^{-1}. The sample is scanned with a piezoelectric stage with a nominal accuracy of about 1 nm in the lateral directions. Focusing on the sample was done with a 100X objective (Olympus MPL 100X-NA=0.90). The Raman microscope provides a lateral resolution of ~250 nm and vertical resolution of 1μm.

CHAPTER 4

NEGATIVE THERMAL EXPANSION IN ULTRATHIN PLASMA POLYMERIZED FILMS

4.1 Introduction

Interactions with the substrate and high specific surface area (film/ air and film/substrate) can cause peculiar properties of the ultrathin polymer films.[132,133,134,135,136,137,138,139] Glass transition of a free standing and supported PS film was found to vary significantly with thickness.[140,141] Other studies have unveiled several interesting phenomena such as the depth dependent glass transition temperature and thickness dependent thermal expansion. [142,143,144,145,146,147] It has been reported that substrate interactions alter the thermal properties of ultrathin poly-(2)-vinylpyridine films.[148] A non monotonic thermal behavior was observed in ultrathin polycarbonate films with a negative and positive thermal expansion below and above glass transition temperature respectively.[149]

Properties of ultrathin polymer films strongly depend upon the fabrication routines. Plasma polymerization allows the deposition of ultra thin polymers films compatible with lithographic fabrication methods, finding applications in sensing devices, MEMS, and optical devices, [150,151,152,153] nanoscale photonics[152,154] or as biocompatible interfaces.[155] The chemical reactions during the plasma polymerization are significantly different from those observed in conventional polymerizations.[150,156] Excited organic species, free radicals and ions react with each other to produce high molecular weight and highly crosslinked chains. The technique offers a unique advantage of the ability to polymerize almost any organic molecule, some of which are impossible otherwise. Due to the fragmentation of the chains and irregular crosslinking, plasma

polymers could display very intriguing novel physical properties.[157] An additional aspect of plasma polymers is that when deposited as thin films, they inevitably possess residual stresses due to their growth mechanisms which can significantly alter their physical behavior.[158,159]

In this chapter, we discuss the unusual thermal behavior of ultrathin plasma-polymerized polymer films on silicon wafers. Remarkably, a large, reversible negative thermal expansion of plasma polymerized polyacrylonitrile (ppPAN) and polytrimethyl silyl acetonitrile (ppPTSA) in the normal direction was observed and related to the thermally induced stress release of a grainy microstructure. We compare this to the behavior of conventional spin-cast films as well as that of polystyrene (PS) spin-cast and plasma films. The unusual thermal expansion (non-linear thermal expansion, large hysteresis between heating and cooling, negative thermal expansion) in these highly crosslinked thin films are suggested to result from large internal stress in these films.

4.2 Experimental details

The polymer films were deposited in custom built PECVD reactor.[160] All the PECVD polymer films were deposited on freshly cleaned (100) silicon wafers. Argon (50-200 cm^3/min, 99.999%), used as the noble gas for generating a plasma, flows into a 10-cm diameter reactor at 0.02-0.5 Torr vacuum through a capacitively coupled radio frequency (RF, 13.56 MHz) discharge of 45 W power. The plasma density is controlled to approximately 10^8 cm^{-3} in the afterglow region. The precursor gas/vapor is added 10 cm downstream from the plasma generation zone. The substrate is located about 2 cm further downstream from the precursor inlet. The precursor flow rate of 1.125 cm^3/min was employed during all the depositions.

Wet deposited ultrathin films of PS (M_w = 250,000 g/mol) were spin coated (3000 rpm) on a silicon substrate from 3% solution in toluene while PAN films (M_w = 3,500 g/mol) were spin coated from 2% solution in DMF. The spin-casting was carried out in class 100 clean room condition and the substrates were priory treated in piranha solution and rinsed thoroughly with nanopure water.

Chemical compositions of the plasma-polymerized films were identified through Fourier transform infrared (FTIR) analysis. FTIR was performed on a Perkin-Elmer Spectrum 2000 FT-IR spectrometer in the transmission mode. A range of 400 to 4000 cm^{-1} was scanned 128 times with 1 cm^{-1} resolution and averaged. The surface morphology of polymer films was studied in the light tapping mode in the range of magnifications (from 1x1 to 30x30 μm) with a Dimension 3000 Atomic Force Microscope.

The thickness of the polymer films at various temperatures was measured using COMPEL automatic ellipsometer (InOmTech, Inc.) equipped with a He-Ne laser with collimated beam of 1 mm diameter. The thickness at different temperatures was computed using a two layer model (polymer film on 1.4 nm SiO_2 layer). The refractive indices of the polymer films used for computing thickness were obtained using Woollam variable-angle spectroscopic ellipsometer system including a VB-200 ellipsometer control module and a CVI Instruments DigiKrom 242 monochromator with a 75-W xenon light source. The reflected polarization states were acquired over the range of 300-900 nm at 1-nm intervals and at angles of incidence equal to 53°, 55°, and 57°.

To study thermal expansion the samples were heated using a Nanoscope heater (DI) and the sample temperature was controlled with a precision of ± 0.1 K. The sample located directly on the ellipsometry stage was held for 10 min at each temperature and the thickness recorded.

The heating-cooling cycles (each about 6 hrs long) were repeated 3-4 times. Prior to the

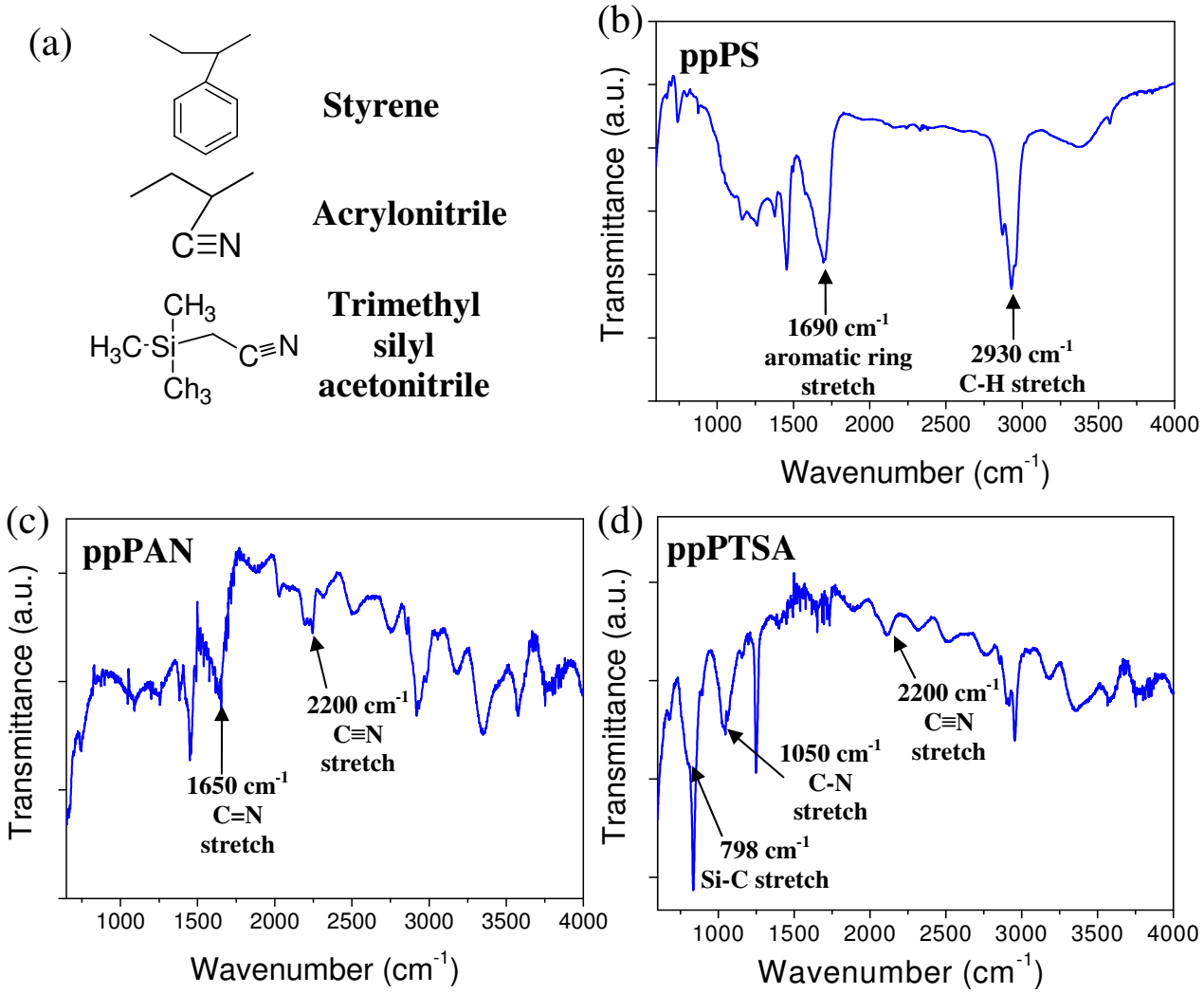

Figure 4.1: (a) Chemical structures of various monomers under study. FTIR spectra of pp PAN, pp PS and pp PTSA showing the characteristic bands.

thermal expansion measurements the polymer films were annealed at 50° C under vacuum for 15 hours to remove a residual solvent and allow stress relaxation.

4.3 Results and Discussions

The chemical structures of the monomers used as precursors for the plasma polymerization are shown Figure 4.1a. FTIR analysis was used to identify the chemical composition of the polymer films under investigation. The FTIR of the PS (Figure 4.1b) was characterized with aromatic ring stretching mode (1600 cm^{-1} and 1450 cm^{-1}), aliphatic C-H stretch mode (2930 cm^{-1}), C-H out of plane vibration (760 cm^{-1}) and ring out-of-plane deformation (690 cm^{-1}).[161] However, it is interesting to note the absence of =C-H aromatic ring vibrations between 3000-3100 cm^{-1} which indicates that the double bonds of the phenyl ring underwent dissociation leading to a high cross-linking in the polymer. The PAN spectrum (Figure 4.1c) shows the characteristic C≡N stretch at 2240 cm^{-1} corresponding to the cyano group. The spectrum also displays a strong C=N stretching mode at 1650 cm^{-1} and N-H stretching at 3300 cm^{-1} suggesting a high degree of cross linking in the polymer film. The spectrum displays other characteristic bands such as -CH_2- stretch (2920 cm^{-1}), C-C stretch and C-H bending (1450 cm^{-1}). The FTIR spectrum obtained from PTSA (Figure 4.1d) shows the representative -Si-$(CH_3)_3$- band (770- 860cm^{-1}), -Si-CH_2R- group (1250 cm^{-1}), cyano group (2220 cm^{-1}) and CH_3 stretch (2960 cm^{-1}). The interesting aspect is the presence of a strong band at 1050 cm^{-1} which corresponds to C-N indicating the cyano group dissociation causing a highly crosslinked network. A relatively weak band corresponding to C=N stretch (1650 cm^{-1}) also indicates cross linking of the polymer. Several other weak bands correspond to the small amount of oxygen impurity, the presence of which is confirmed with XPS.

Table 4.1. Thermal characteristics of nanoscale polymer films

Polymer	Ultrathin films from present study							Bulk films (obtained from literature)
	Plasma polymerized				Spin-cast			
	α **(K^{-1})** 10^{-4}	***t*** **(nm)**	***R*** **(nm)**	***C*** **(deg)**	***α*** **(K^{-1})** 10^{-4}	***t*** **(nm)**	***R*** **(nm)**	***α*** **(K^{-1})** 10^{-4}
PS 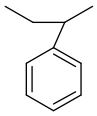	1.9	148	1.5	69	1.7	169	0.25	0.8-2.8 * [Ref. [25]]
PAN 	-3.1	95	1.7	55	1.6	20	0.20	1.0 [Ref. [162]]
PTSA 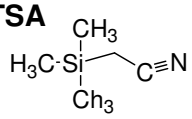	-2.5	97	0.5	75	NA **	-	-	-

α: Linear thermal expansion coefficient below T_g; *t*: Thickness; *R*: RMS roughness over 1×1 μm^2 area; *C*: Contact angle; * Thickness dependent

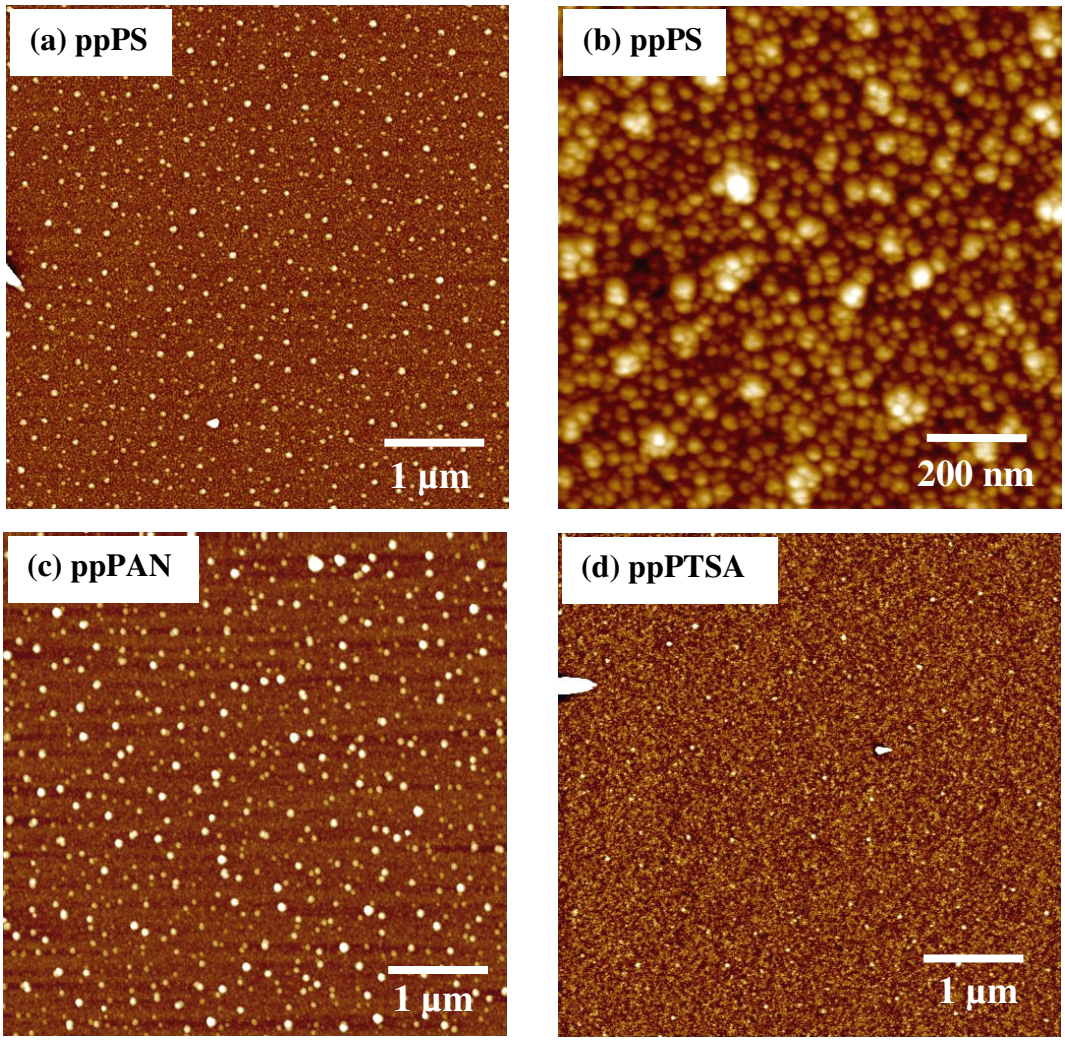

Figure 4.2. AFM images showing the surface morphology of pp PS (a) and (b), pp PAN (c), and pp PTSA (d). The z range is 20nm for all images.

The chemical structures of the monomers used as precursors for the plasma polymerization are shown in Table 4.1. The polymer films were deposited by PECVD technique in a custom built PECVD reactor and thoroughly characterized with FTIR, AFM, and XPS. [152,163,164,165,166] FTIR was used to confirm the chemical composition of the polymer films and their crosslinked structure.[167] Thermal expansion of the polymer films was studied by measuring the thickness of the films using ellipsometry and the thickness values was independently confirmed by AFM scratch test. Selected AFM images of the polymer films obtained under different conditions are

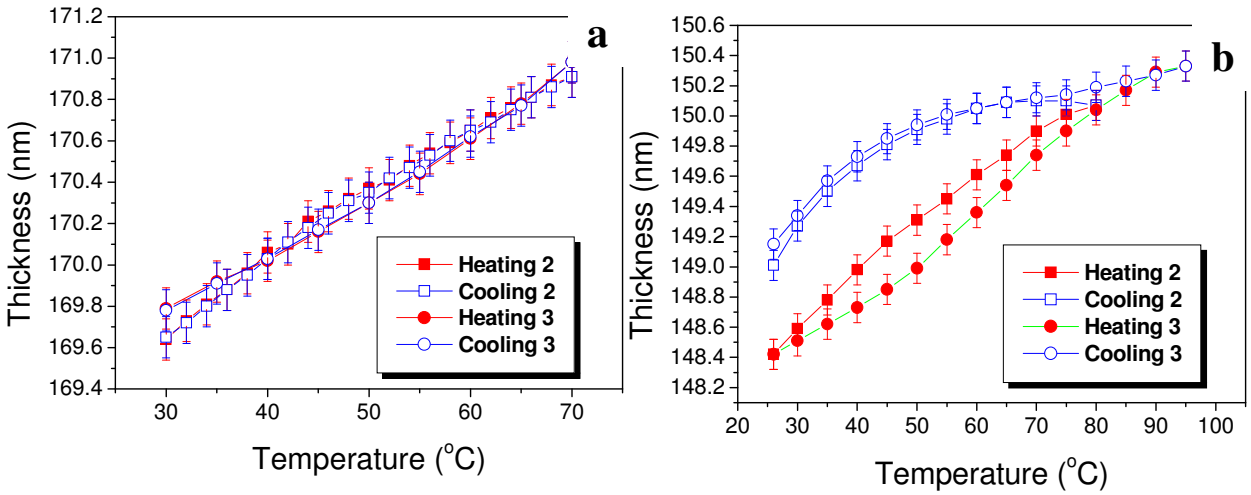

Figure 4.3: Film thickness vs temperature for plasma polymerized and spin coated polystyrene films for 2nd and 3rd heating and cooling cycles.

shown in Figure 4.2. The plasma polymerized (ppX) polymer films exhibited a well-developed grainy surface morphology compared to the much smoother spin deposited counterparts.

The plasma polymerized films exhibited a well-developed grainy surface morphology with grain sized below 100 nm as compared to the smooth surfaces of spin-cast films with no specific features. The RMS surface microroughness was found to be 1.5 and 1.7 nm for pp PS and ppPAN, respectively, with ppPTSA displaying the lower microroughness at 0.5 nm. In all cases, the microroughness of plasma polymerized films is much higher than that observed for spin-cast films (around 0.2 nm) (Table 4.1). Contact angle within 55-75° corresponds to modestly hydrophilic surfaces which is well below that expected for bulk polymers (e.g., 90° for PS) and indicated the presence of polar groups at the surface.

Thermal expansion of spin-cast PS films is plotted for second and third thermal cycles (each cycle was acquired within 6-8 hours) in Figure 4.3a. In all the experiments the first heating and cooling cycle were disregarded to eliminate preparation pre-history. The thermal expansion

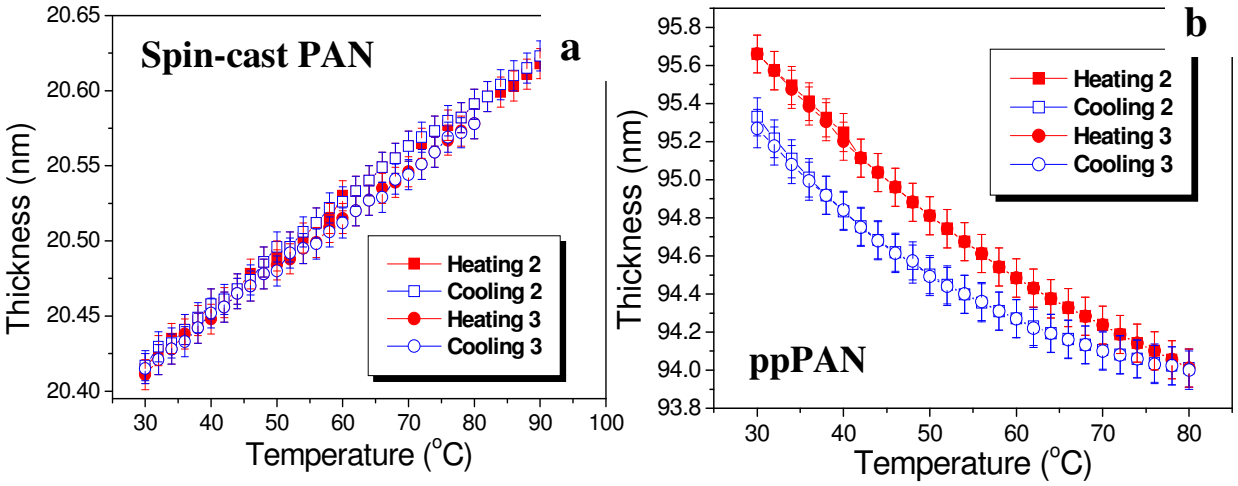

Figure 4.4: Film thickness vs temperature for plasma polymerized and spin coated polyacrylonitrile films for 2nd and 3rd heating and cooling cycles

coefficient was found to be 1.7 ± 0.3×10^{-4} K^{-1} for spin-cast PS film and 1.9 ± 0.3×10^{-4} K^{-1} for ppPS which is within a conventional range of values (Table 4.1). Thermal expansion of the spin-cast PAN with a thickness of 20.5 nm is also linear with a thermal expansion coefficient 1.6×10^{-4} K^{-1} which is slightly higher but close to that for the bulk film (Figure 4.4a, Table 4.1).

However, all the plasma polymerized polymers exhibited a significantly non-linear variation of thickness with temperature while cooled. The final thickness was 0.3-0.5 nm higher than the initial immediately after cooling (for the sake of clarity cycle 3 is offset). However, the film restored to original thickness after long relaxation time (~ 8 hours). This behavior was observed for all the plasma polymerized films while the spin-cast films exhibited no such hysteresis. We suggest that the observed hysteresis followed by relaxation might be due to the stresses

developed in the polymer during the deposition process. In fact, a hysteresis behavior of residual stresses in plasma deposited thin films during thermal cycling was previously reported and accounted to different rates of relaxation. [168,169,170]

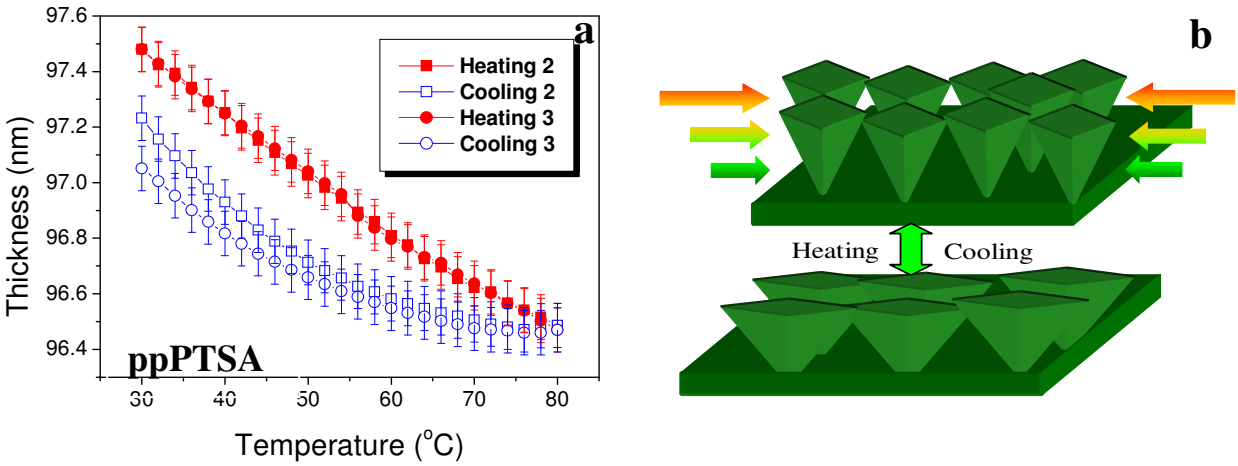

Figure 4.5: (a) Film thickness vs temperature for plasma polymerized trimethyl silyl acetonitrile film for 2nd and 3rd heating and cooling cycles and (b) schematics of the plasma polymer film with the wedge-shaped morphology undergoing a stress release with heating which causes lateral expansion and normal contraction of the wedges.

Moreover, the thermal behavior of two plasma polymerized films was absolutely uncharacteristic for conventional polymers. In both cases, we have observed thermal contraction of the film in vertical direction during heating (Figures 4.4b, and Figure 4.5a a). Furthermore, this negative thermal expansion was found to be reversible with some hysteresis followed by relaxation as discussed above for ppPS. The thermal expansion coefficient calculated from linear portion below 50°C was $-3.1 \pm 0.2\times10^{-4}$ K^{-1} for ppPAN and $-2.5 \pm 0.2\times10^{-4}$ K^{-1} for ppPTSA (Table 4.1).

This unusual negative thermal expansion (NTE) behavior is suggested to be caused by the presence high residual stress in the polymer film common for plasma polymerized materials combined with developed grainy surface morphology as depicted in Figure 4.4b. The high in-plane compressive strength common for plasma polymerized polymers might originate from

specific, wedge-type of their growth.[171,172] The residual stresses arise due to the wedging effect during the deposition process where the high energy fragments wedge in the existing film. In fact, for some plasma polymerized polymers we estimated in-plane compressive stress to be as high as 50 MPa which is close/exceeds yield strength of polymeric materials. Figure 4.5b shows a schematic representation of the plasma polymer films with wedge-shaped individual grains in highly compressive state. Increase in the temperature causes these polymer grains to expand laterally with a simultaneous vertical contraction of the entire film. It is worth to note that although the residual stresses occur for all the plasma polymerized polymers the NTE phenomenon was only for ppPAN and ppPTSA. The actual cause for this remains uncovered but we should note that both the NTE polymers possess a C≡N group which should lead to a higher degree of crosslinking and different topology in comparison with ppPS.

In fact, NTE has been previously observed in some special cases. E.g., NTE was reported along the chain direction for fully aligned linear polyethylene chains.[173] A different effect exhibited by thermal stresses and elasticity in the negative axial thermal expansion of isotactic polypropylene has been discussed.[174] Recently, it has been proposed that a decrease in the entropy associated with expansion in some systems makes thermal contraction thermodynamically favorable.[168] However, the nature of NTE in amorphous polymer films studied here should be very different and similar to the case of high stresses comparable to the yield stress which significantly alter the thermal expansion behavior of the polymer films.[175]

The negative thermal expansion phenomenon in nanoscale polymer films may find applications in technologies requiring nanocoatings with zero thermal expansion. Harnessing these residual stresses either by refining the deposition procedures or by 'freezing' in non-equilibrium state will be a key issue. By designing composite materials comprising of elements with positive, zero, or negative thermal expansions, effective temperature variations in the nanocomposite materials

could be minimized or eliminated. These materials can find interesting applications in MEMS, IC, and optical devices as means to control and compensate the conventional materials which expand on heating.

CHAPTER 5

MECHANICAL PROPERTIES OF COMPOSITE POLYMER MICROSTRUCTURES FABRICATED BY INTERFERENCE LITHOGRAPHY

5.1. Introduction

Polymer/air (porous) structures, in which both phases are bi-continuous in three dimensions, exhibit large specific surface areas in conjunction with the controlled hierarchical porous network. This combination provides a unique platform for designing microstructured materials with interesting transport and adsorption properties. In addition to the steric effects imposed by the porous structure, chemical modification of the porous materials enables tailoring of the surface chemistry and polarity, which provides additional functionality. Porous materials find numerous applications in the field of life sciences, such as cell culture substrates for cell adhesion, biomaterials as tissue engineering scaffolds with biocompatible and biodegradable properties, cell patterning, and protein microarrays.[176]

Dissipation and absorption of mechanical energy within highly porous microcoposite structures is another intriguing topic critical for some applications where high mechanical loads are involved. However, most of materials suggested and discussed to date for such applications are either microscopic foams with random combination of open/close porous interior or macroscopic organized structures (such as civil engineering truss frames). Only a few examples of microscopic *organized porous structures* have been reported to date. Although foam-like structures can be exploited for lightweight structures with microscopic porous morphology, they

exhibit much lower strengths and their high "polydispersity" leads to variations in local physical properties.[177]

Trusses are well known, highly organized 2D and 3D lightweight structural constructions composed of struts (beams) and nodes (joints) with excellent mechanical properties. They are widely used in civil engineering but rarely considered as examples for polymer microstructures. Recently, several miniature truss structures (with mm to cm dimensions) have been theoretically designed, fabricated, and tested.[178,179] Outstanding specific mechanical properties are predicted for these structures. The design for ultimate stiff and lightweight truss structures should provide conditions such that beams are under compression or tension (stretching) while avoiding bending.[180] Furthermore, the open architecture allows for potential beam/wall modification, as well as added functionality since the high surface area (>100 m^2/g) allows for thermal cooling via a continuous fluidic phase or as a thermal barrier using evacuated pores.[181,182] The design consideration includes specific application of the final structure since the mechanical properties exhibit a trade-off to a certain degree. Hence, for load bearing applications, yield strain, yield stress, and creep properties of the structure have to be optimized.[177] For example, the materials for automotive applications need to be designed to withstand a strain rate of 40/s, while those designed for ballistic protection are to be designed for strain rate of ~2000/s.

For some mechanical applications, pyramidal architectures have been predicted to be comparable or better than the benchmark honeycomb panels, but with potential for much lower density.[183] They are fully triangulated and show stretch-dominated properties. Kagome lattices, the name derived from Japanese weaves, are more efficient, offering the lowest mass-to-stiffness ratio.[184] Kagome and tetragonal microtruss structures are suggested as the most efficient designs with maximum stiffness and load limit achieved in combination with extreme

lightweight properties. The minimum node connectivity for a class of lattice structured materials to be stretch-dominated is six for 2D and twelve for 3D.[177] The fabrication of conventional truss structures is usually a cumbersome routine, requiring step-by-step assembly of numerous elements. Moreover, this process cannot be scaled down easily from common meter/sub-meter dimensions of panels and sub-meter/millimeter dimensions of beams to form truly microstructural architectures.

The challenge of fabricating micro- and nanoporous materials from a variety of organic and inorganic materials has been addressed by numerous methods. Template-assisted fabrication is one of the most popular methods, where the porous structure is employed to obtain a negative replica of a second desired material. Porous templates have been achieved by the self assembly of monodisperse submicron colloidal particles (e.g. silica or polymer particles) under carefully controlled processes such as sedimentation, centrifugation, filtration, dip coating, or slit filling.[185,186] Subsequent infiltration and solidification of the second material (e.g. polymerizing the infiltrated monomer), followed by the removal of the template (colloidal crystal) by dissolution of the particles (e.g. HF etch of SiO_2 colloidal spheres), leaves behind a highly porous polymeric structure. This simple technique, which relies on the foundations of colloidal crystallization, has been extended to achieve binary and ternary super lattices (particles of different sizes) by exploiting electrostatic interaction between oppositely charged particles.[187,188]

The other important class of templates is the natural biological materials with complex periodicities which enable the fabrication of porous structures with complex ordering. Bacterial threads, echinoid skeletal plates, eggshell membranes, insect wings, pollengrains, plant leaves, and wood have been employed as biological templates.[189,190,191,192] Other approaches such as breath figure templating[193], dewetting of multilayered films,[194] and selective etching of block copolymers[195] have achieved ordered porous structures. However, these methods suffer from

limited range of structural geometries and long time requirements to achieve templates with long range periodic structure. Most of the techniques discussed so far have a high density of undesired defects as well.

Multiple laser beam interference lithography is a facile technique for realizing uniform periodic polymeric structures over relatively large areas has been drawing increased attention over the past few years.[196] The interference pattern is essentially a periodic light intensity distribution pattern in one, two or three dimensions depending on the number of light beams interfering. A photocurable polymer (photoresist) exposed to the variable light intensity undergoes chemical crosslinking proportional to the local light intensity. Subsequent dissolution of the modified or unmodified portions results in complex periodic polymeric structures replicating the interference pattern. The technique offers fine control over the size and shape of the periodic structures, enabling the realization of much broader geometries than colloidal or block copolymer assembly.[197,198,199,200] Interference of multiple laser beams was initially employed to write simple hologram gratings [201] and was later developed as a lithographic technique to create 3D periodic polymeric structures[202] for applications such as photonic structures. Recently, we have demonstrated that the geometry and hence the phononic band gap of organized porous PDMS structures can be mechanically tuned.[203] Depending upon wavelength, geometry, and processing conditions, a variety of microporous polymer structures can be generated with a typical spacing in the range of 600 nm -1.3 □m, pores dimensions from 100 nm to 800 nm, strut diameters from 100 nm to 600 nm, and with the overall porosity ranging from 20% to 60%.[204,205]

The porous architectures with different lattice symmetries might serve as advanced mechanical structures, while their open porous design provides lightweight properties. For demanding mechanical applications, the key is to select appropriate polymeric materials to create a "skeleton" network with proper 3D geometry for desired mechanical stress distribution. Very

recently, interesting deformational behavior associated with buckling instabilities has been observed in 2D periodic elastomeric structures subjected to compressive stresses.[206] Understanding the elastic and plastic responses as well as the ultimate fracture behavior of the microframe all become paramount. However, despite the recent spur of activities, the advantages of creating sophisticated 2D and 3D periodic microstructures with open, bicontinuous, porous network architectures as microcomposites with unique mechanical properties have not been realized.

This chapter presents recent results and ideas for exploiting organized microporous polymeric structures, obtained by interference lithography, as highly structured microcomposites. We demonstrate the ordered single and bi-component microstructures with high degree of control over the microscopic organization of the polymeric phases and the mechanical properties of these structures. The microscopic and macroscopic mechanical (elastic and plastic) properties of these structures are discussed here. We also demonstrate the possibility of employing the organized microporous structures as masters in soft lithography, enabling the faithful replication of the complex topographical features with polymers using capillary transfer lithography. A recent review on the application of interference lithography for the fabrication of porous microstructures can serve as an excellent introduction to the subject and is recommended to be read before this chapter.[207]

5.2. Organized porous structures in soft lithography

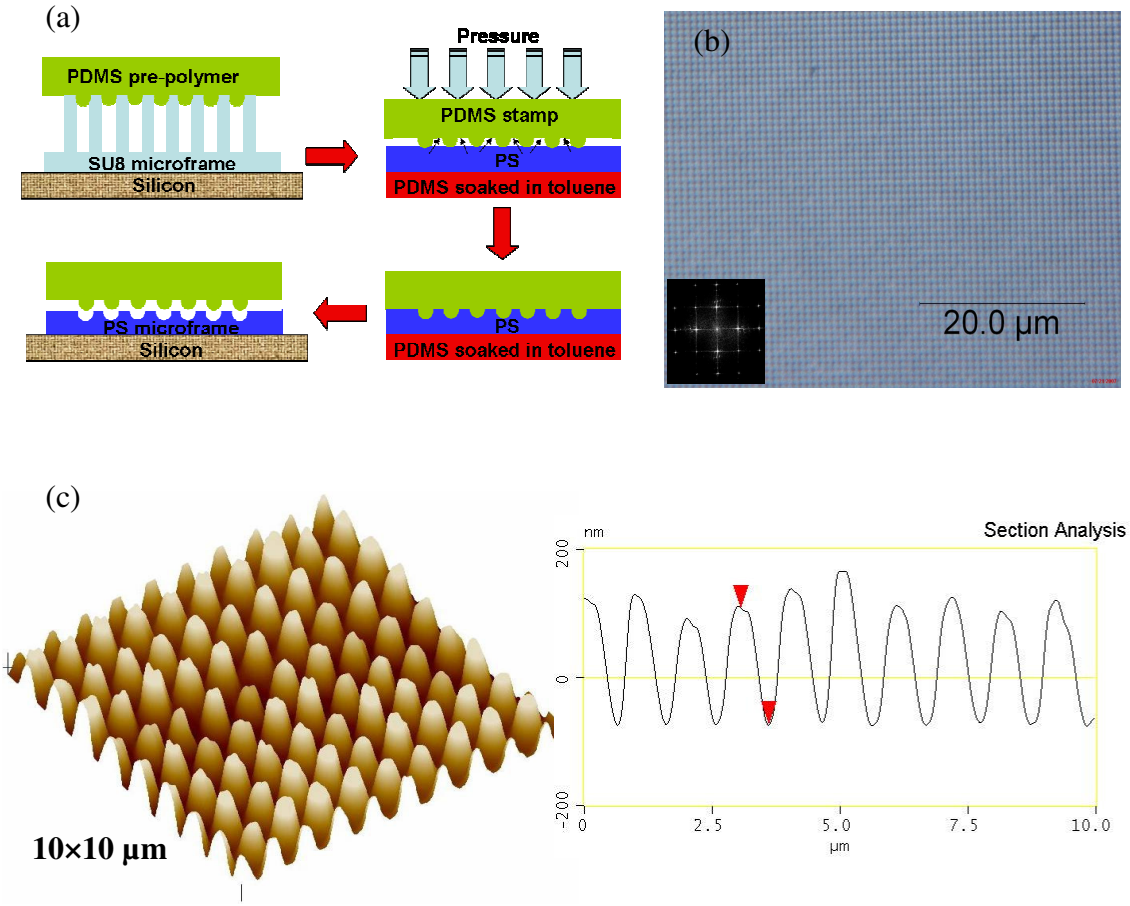

Figure 5.1: (a) Schematic representation of the capillary transfer lithography using ITL structures as masters. (b) Optical image of the PDMS stamp showing the large scale uniformity. (c) AFM image depicting the vertical posts (negative replica of SU8 master) of uniform height (d) Cross section of AFM image showing the uniform height of the posts.

Here, we demonstrate examples of utilization of microporous structures as masters for microprinting. Figure 5.1(a) shows the schematic of the fabrication process which involves the preparation of the negative PDMS replica, followed by infiltration of polystyrene (PS) solution into the receding portions of PDMS and finally, transferring and depositing the PS structure onto a different substrate.

Capillary transfer lithography (CTL) [208] was chosen to reproduce a square array of air cylinders formed by interference lithography in SU8 material. A mixture of pre-polymer and curing agent

(10:1) was poured onto the 2D structure, followed by degassing and curing at 75°C. Subsequently, the PDMS was peeled from the SU8 to create a negative replica of the 2D organized porous structure of the initial architecture.

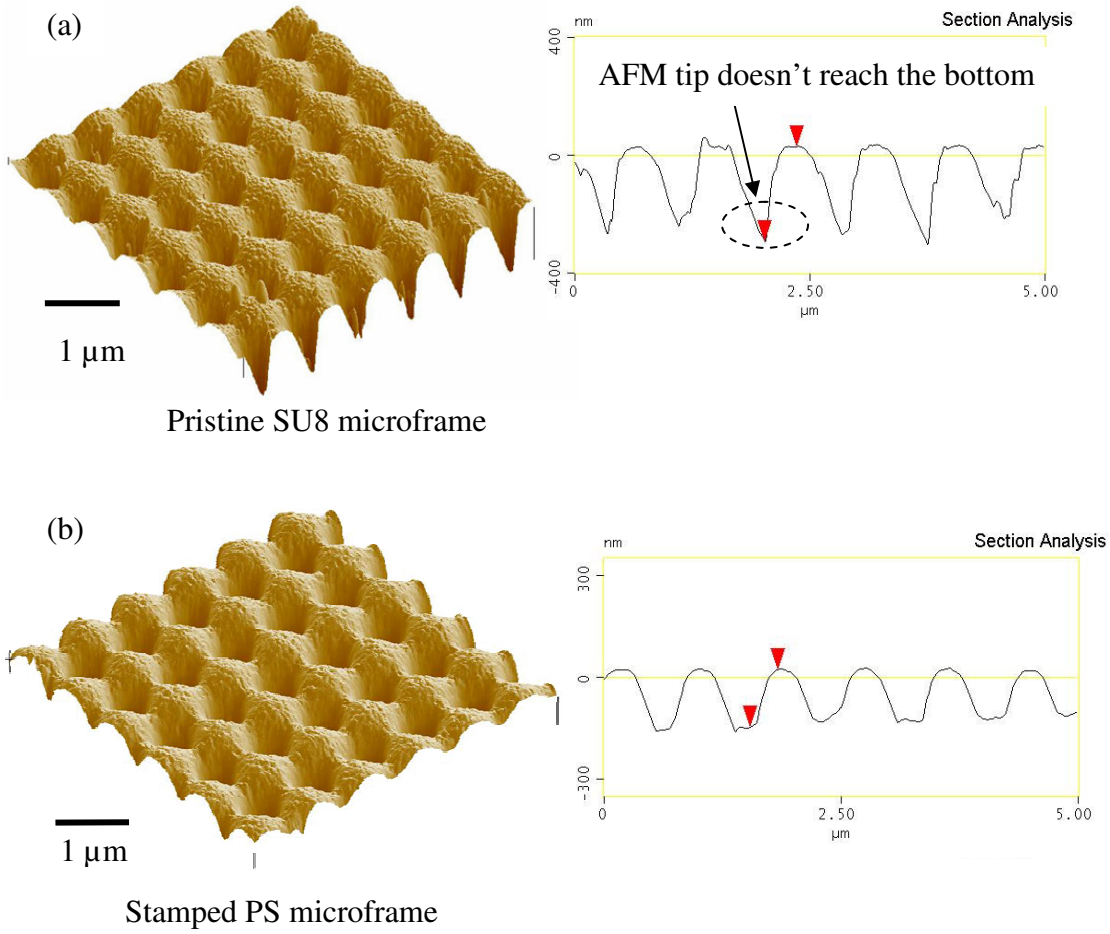

Figure 5.2: AFM images and the corresponding cross section images of (a) Pristine SU8 microframe (b) Stamped PS structure showing identical topolgraphical features down to the nanoscale.

It is important to note that due to the high viscosity of the pre-polymer, only a partial infiltration (200 nm deep) into the SU8 porous structure is achieved. Complete infiltration of the viscous DMS into the pores requires external forces such as evacuation of the pores from the bottom. However, it is interesting to note that PDMS replica was extremely uniform over large surface

area as shown by the optical image (Figure 5.1(b)). The inset FFT diagram shows the sharp spots originating from the highly ordered square lattice of the arrays of vertical posts. Moreover, AFM image (Figure 5.1(c)) shows uniform height of the vertical posts and the cross section of posts shows the height to be nearly 200 nm.

The negative replicas obtained, were then used for the fabrication of organized structures from other polymers (Figure 5.2). Figure 5.2 (a) and (b) show the AFM images and the corresponding cross sections of the original SU8 lattice along with the stamped replica of SU8 square lattice structure from PS. One can observe the remarkable similarity between the two structures with excellent replication of surface topology of the original SU8 IL structure. In fact, even the nanoscale grainy morphology of the SU8 surface caused by photopolymerization during the ITL process was faithfully reproduced in the final structure.[209] It is worth mentioning that the PS stamped structures showed significantly smaller vertical height (150 nm), measured from the AFM cross sections, compared to that PDMS posts (200 nm) due to the elastic deformation of the PDMS stamp during compression.

5.3. Mechanical properties of organized porous ITL structures

The study of the small and large mechanical deformations of the organized porous structures presented here is an important but technically challenging task. Both local elastic deformations of the nanoscale features as well as the overall plastic behavior of the whole porous microstructure at large strains and ultimate failure are discussed in this section.

5.3.1 AFM nanomechanical measurements

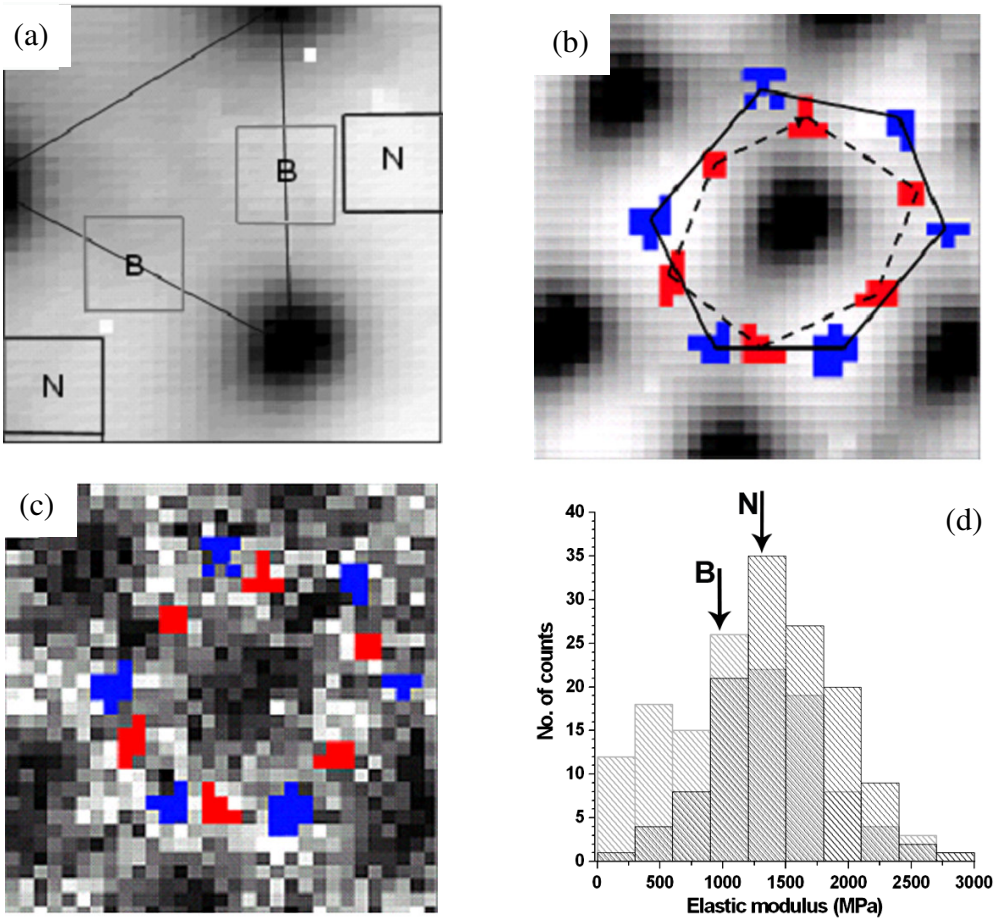

Figure 5.3: High resolution AFM micromapping of the photopatterned SU8 film: (a) 32x32 topography and (b) elastic modulus collected during force micromapping of the 2.5x2.5 μm^2 surface area (two designated areas are marked by squares of pixels (blue for nodes (**N**) and red for beams (**B**)) (c) 32x32 high-resolution AFM topography during force micromapping of the 2x2 μm^2 surface area and (d) combined surface histograms collected for selected surface areas (500x500 nm^2) for nodes (black boxes) and beams (gray boxes)

AFM nanomechanical measurements are conducted to address the spatial distribution of stiffness and the elastic response in the porous microstructure in accordance with the procedure adapted in our labs.[210,211,212] Nanomechanical measurements are conducted in the elastic

regime, with a small indentation depth allowing full elastic recovery of the probed areas.[213] In this study, the array of force–distance data obtained with surface force spectroscopy was converted to loading curves (indentation vs. load) to evaluate the surface stiffness and the elastic modulus for IL structures (Figure 5.3). The Hertzian model of elastic deformation by a semispherical indenter interacting with a planar elastic solid was applied. This approximation is acceptable for the small penetration depths and intermediate loading rates.[210] Under these probing conditions, the viscoelastic contributions are negligible, as has been demonstrated in our previous publications.[214,215]

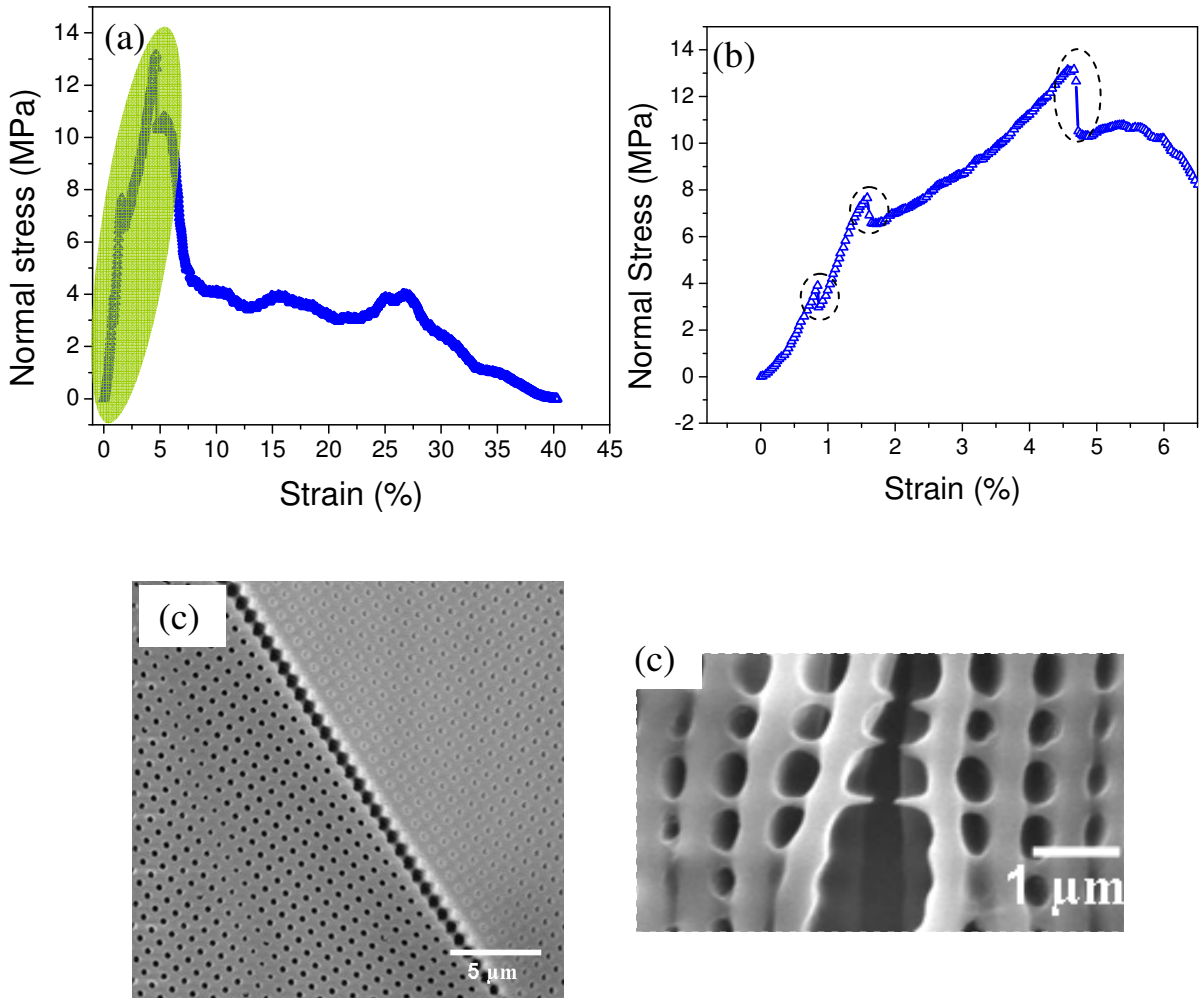

Figure 5.4: (a) Stress-strain plot of tensile measurement performed on 2D SU8 microframe, showing the multiple yield points followed by prolonged necking. (b) Linear regime of the stress-strain plot showing multiple yield points. (c) SEM image of the sample subjected to tensile measurement showing the crack propagation along [1 0] direction. (d) SEM image showing the necking and large plastic deformation of the struts SU8 microframe.

Nanomechanical measurements of the pristine 2D porous structures conducted with nanoscale indentation depth showed a clear bimodal distribution of the SU8 elastic response (shown in Figure 5.3).[213] A broad distribution of elastic moduli ranging from 300 MPa to 1.7 GPa is due to local variations of the properties at nodes, struts, sidewalls, and slope regions (various regions shown in Figure 5.3 (a)). A statistically significant difference of the elastic modulus between

nodes and beams was confirmed by the high resolution mapping of surface elastic properties (Figure 5.3(b) and (c)). The average elastic modulus obtained from these histograms (Figure 5.3(d)) for the nodes was 1480 MPa, which is higher than the calculated value for the beam areas (1120 MPa) due to periodic variation of the light intensity in the course of fabrication. Such a spatial variation is, probably, a very common feature which should be expected for any microstructures fabricated by interference lithography.[213]

5.3.2 Large strain tensile measurements

The AFM nanomechanical measurements provide no insight into the mechanical behavior at a macroscopic scale and for large deformations, which are relevant to the integrated mechanical applications. Therefore, microtensile tests were designed and performed on a 2D square lattice SU8 sample of 2μm thickness with pores of 380 nm in diameter and with a spacing of 830 nm with effective porosity close to 20% (see Figure 5.2(a) for surface topography). Free standing samples (0.9 cm×0.3 cm×2 μm) with 2D square lattice were mounted onto standard microtensile sample holders. Tensile measurements were performed with a force resolution of 3.5 mN and at a strain rate of 10^{-3} /sec.

Figure 5.4(a, b) shows a stress-strain plot obtained under uniaxial tensile loading with the shaded area indicating continuous elastic resistance. Several spikes correspond to the formation of cracks followed by gradual fracturing of the struts (Figure 5.4c, d). The crack formation might be preceded by a local necking of the struts (Figure 5.4(d). However, the unperturbed regions still remain in the elastic regime as can be seen by the elastic response following the spikes. Sharp and multiple yield points correspond to the initiation and propagation of microcracks perpendicular to the stress direction (see cracks in Figure 5.4 (c) and (d)). Each straight crack causes the number of load bearing struts to decrease, which in

turn lowers the effective modulus of the whole microstructure (see changes in slope in Figure 5.4b). Such an unusual, step-wise mechanical deformation is caused by highly organized porous microstructure. It is worth noting that similar load drops can be due to initiation and localization of plastic deformation in the polymer samples subjected to uniaxial and high rate tensile strain resulting in highly inhomogeneous deformation (10^4-10^5 /s).[216]

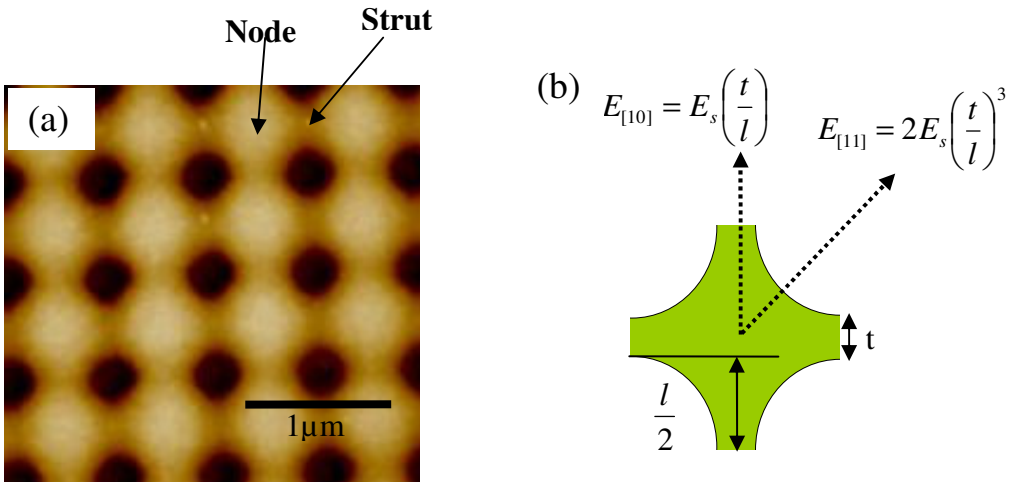

Figure 5.5: (a) AFM image identifying the struts and the nodes of the square lattice SU8 microframe. (b) Schematic representation of unit cell of 2D square lattice and the elastic modulii in the two characteristic directions.

The stress-strain behavior shows an interesting effect: after the highest yield point (at 13 MPa), prolonged necking occurs before the ultimate failure. Overall, the 2D square lattice structure exhibited remarkably high ultimate strain, reaching 35% which is very uncharacteristic behavior for homogeneous SU8 materials with a high degree of crosslinking.[217] Such large plastic deformation can be observed only for very fine SU8 struts (Figure 5.4(d)) with a diameter of several hundred nanometers and related to scale-controlled elasticity of modestly crosslinked elements of IL microstructures.[207] The prolonged necking of the struts under extended deformation provides extremely high toughness to these structures reaching high values of 1.5 MJ/m^3. The toughness of these structures is nearly five times higher compared to the random

mats from drag line silk fibroin and layer-by-layer thin films, asserting the efficient energy absorption of the SU8 microframe structures.[218,219]

The elastic modulus of the 2D lattice was calculated from the initial slope of the stress-strain curve to be 0.5 GPa, which is much lower than that usually reported for the bulk SU8 material (2-4 GPa) and can be associated with porous architecture of these specimens.[217] It is known that for cellular foam material with square lattice of air columns (Figure 5.5(a)), the elastic modulus of the structure is anisotropic and is much lower than that for struts.[177] Indeed, the elastic modulus of the structure along [1 0] and [1 1] directions is given by $E_{[10]} = E_s\left(\frac{t}{l}\right)$ and $E_{[11]} = 2E_s\left(\frac{t}{l}\right)^3$ where E_s is the elastic modulus of the cell wall material, '*t*' is the strut wall thickness, and '*l*' is the distance between the adjacent struts (as schematically shown in Figure 5.5(b)). For the 2D microframe investigated here, t = 330 nm, l = 500 nm and the elastic modulus of the SU8 material after IL fabrication is 1.1 GPa (see above). Thus, the effective elastic modulus of the microframe along [1 0] direction should be reduced to 0.7 GPa, which is only a 30% deviation from the experimentally determined value of 0.5 GPa for the initial stage of the elastic stretching.

5.3.3 Fracture behavior of the organized porous structures

The ultimate performance of microframe structures can also be addressed using a simple peeling process that involves adhering adhesive tape to the structure and peeling off a portion of the film from the substrate.[220] The remaining film is then transferred onto a carbon tape and mounted in an SEM holder. This peeling test involves a complex interplay of forces and allows us to observe the mechanical response of the microframe structure in a wide variety of

deformational modes. We thus see the combined effect of tension, bending, compression, buckling, and shearing on our samples.

Inspection of the film after this procedure reveals a host of interesting deformed morphologies related to the fracture and various types of plastic deformations. Features associated with failure include long, straight, micrometer-wide cracks following particular lattice and easy-fracture directions (see Figure 5.6(a)). The lines of easy fracture always involve the failure of the thin, transversely oriented struts in the 2D samples as has been discussed in detail previosuly.[220]

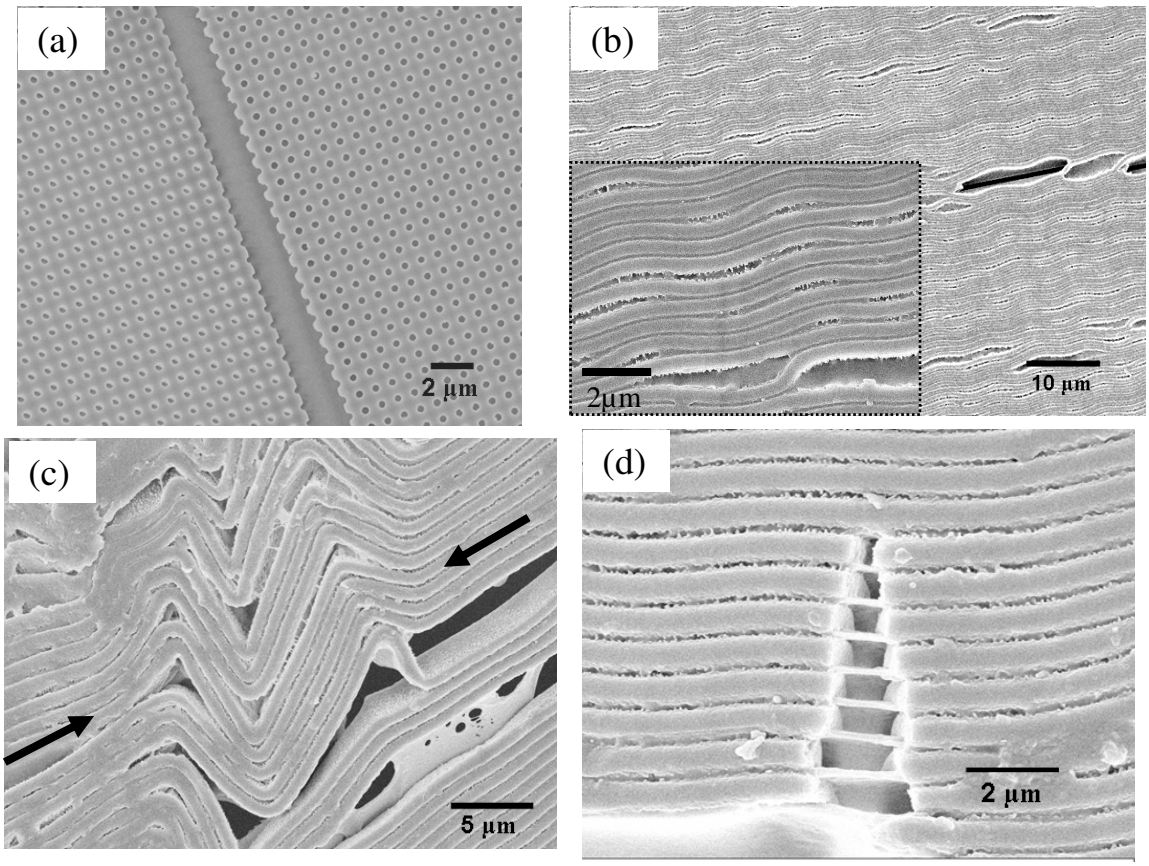

Figure 5.6: SEM image showing fracture behavior of the 2D SU8 microframe (a) Fracture of 2D structure along the easy crack lines (b) Penny shaped cracks and sinusoidal buckling in the 2D microframe sample under compressive stress (c) Compressed regions of the microframe undergoing catastrophic buckling. Arrows indicate the direction of compression. (d) Ultimate fracture of the compressed walls leading failure of the structure

Figure 5.6(b) shows two other important modes of deformation of the 2D sample under compression. The 2D microframe compressed laterally undergoes the collapse of the square lattice of circular air cylinders, forming a stack of thin sheets. Furthermore, the stacks can undergo lateral compression in the perpendicular direction to the initial compressive forces resulting in wrinkling in the plane of the lattice (Figure 5.6(c)). Collapse of the struts and buckling of the thin walls are two efficient energy absorbing mechanisms playing significant role in the deformation.

It is known that buckling of the cell walls in macroscopic cellular structures can occur in two distinct modes: creep buckling and catastrophic buckling.[177] Creep buckling of the wall involves the uniform sinusoidal deformation of structure, while catastrophic buckling involves acute curvature of the walls. Figure 5.6(b) shows the uniform sinusoidal buckling of the thin wall structures which can be related to the creep buckling of the SU8 material. During the peel process, the microframe structure possibly undergoes lateral compression resulting in an in-plane periodic wrinkling pattern. Upon further compression, the deformation of the lattice is localized within very short regions leading to a catastrophic buckling with sharp curvature. Such catastrophic buckling modes were observed in the fractured samples (Figure 5.6(c)). It is important to note that various modes of deformation such as compression of the struts, sinusoidal buckling and catastrophic buckling of the SU8 thin plates, are plastic in nature. These large plastic deformations of the struts bridging the crack result in large absorption of strain energy as observed in tensile measurements (toughness reaching 1.5 MJ/m^3 as was discussed above).

5.4. Bi-component organized IL structures

5.4.1 Infiltration of a second phase into open porous structures:

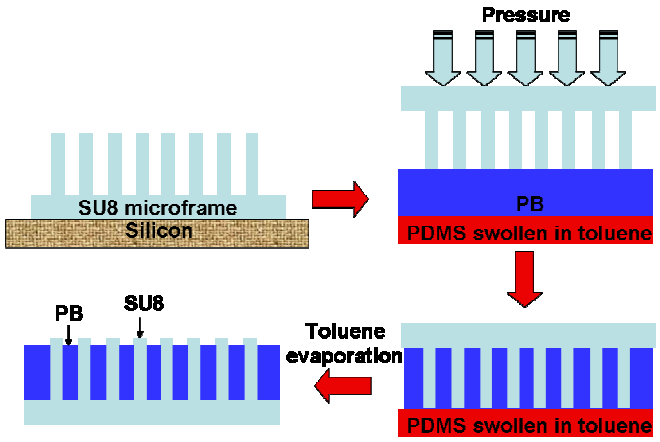

Figure 5.7: Schematic representation of the capillary assisted infiltration of PB into the grid structure.

Combining hard and soft polymer components provides multifunctional materials and coatings with synergetic properties and is frequently utilized for design of advanced polymeric composites.[221] For instance, a strong matrix serves as a load-bearing skeleton for structural integrity, while the soft component can be responsible for the adhesion control. As is known, to achieve proper multiphase structure in conventional composite materials, a complex monitoring of the kinetics of phase separation is required, combined with multiple processing stages (e.g., adding a new component). Although a certain control of spatial scale, morphology, microstructure, and shape is achieved with temperature-composition variation, the resulting composites usually possess high variations of feature dimensions, topology, and composition. These variations make it difficult to prevent a wide fluctuation of physical properties. While such a behavior affects the macroscopic properties of bulk composites, it can be even more critical for microstructural materials with dimensions comparable to the microphase domains (e.g., polymer MEMS).

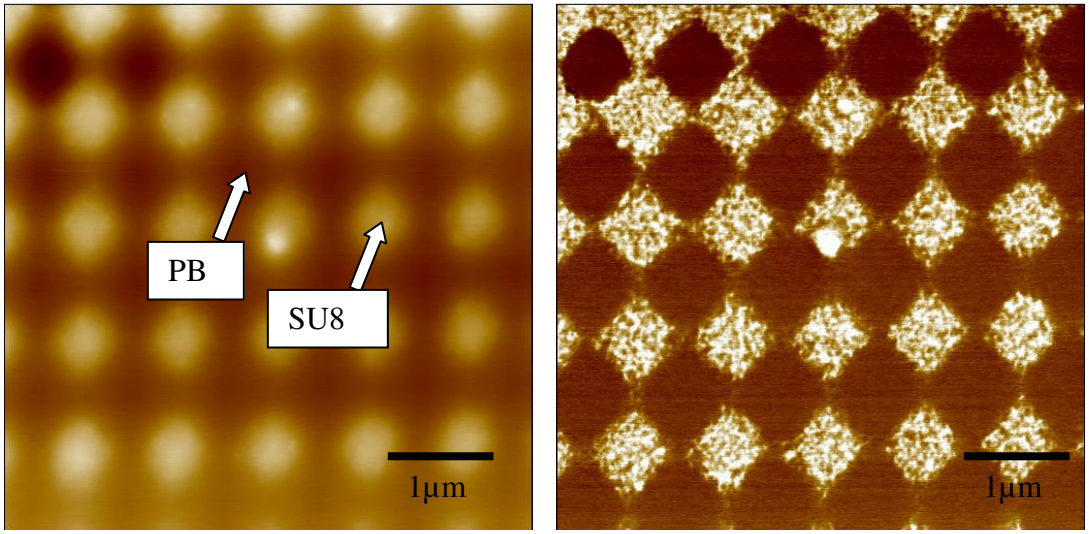

Figure 5.8: AFM images depicting the SU8/PB bicomponent microframe (a) Topography (b) Phase image depicting the two components.

In view of the above consideration, we suggest that organized porous IL structure can serve as an organized matrix for the fabrication of microcomposite materials with well-defined, uniform, and pre-determined component distribution. To implement this strategy, we have applied two independent approaches to infiltrate the second rubbery polymeric phase into the SU8 microframe structure, namely, capillary driven infiltration of polymers and *in situ* polymerization in the microframe structure. In the first method, capillary infiltration of the polymer was employed to fill the 2D open porous structure, as schematically represented in Figure 5.7. The capillary force infiltration method uses capillary-driven filling of polymers softened by solvent (lowering the viscosity). The second polymer component (2% polybutadiene (PB) in toluene) is spin coated onto the PDMS substrate swollen in toluene. Swelling the substrate in toluene continuously supplies the solvent, softening the spin cast PB layer. Upon bringing the SU8 porous structure into intimate contact with the PDMS substrate, the PB solution fills the recessed region of the SU8 porous structure (Figure 5.7).

This method offers relatively uniform infiltration of the rubbery phase into the glassy polymer truss structure as illustrated by Figure 5.8. One of the distinct advantages of the method is that it results in structures with binary pristine surfaces (with no residues of PB material on SU8). The low surface energy of the PDMS substrate results in a poor interaction with PB, enabling the formation of binary surfaces in the final structure. Figure 5.8(a) and (b) show the AFM topography and phase images of the binary infiltrated structure, clearly depicting the distinct SU8 original structure (square matrix) and PB phase.

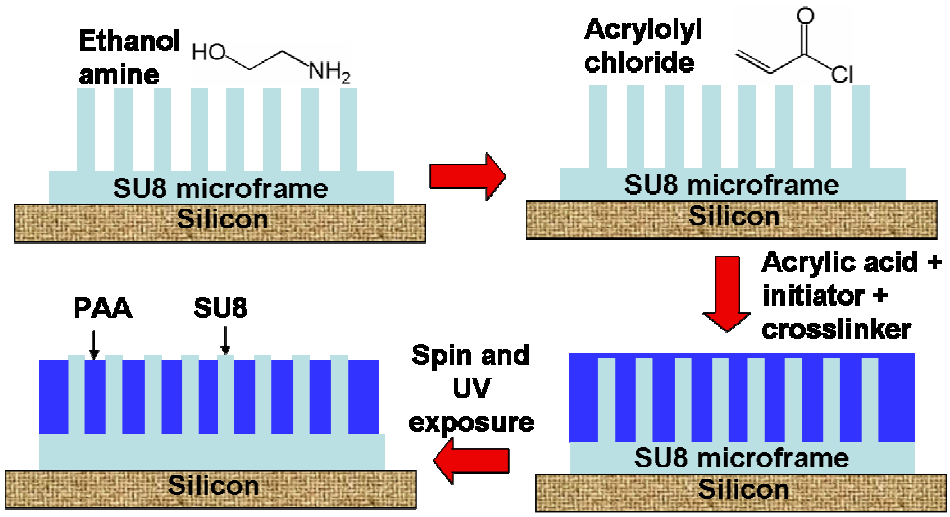

Figure 5.9: (a) Schematic representation of the polymerization of acrylic acid in the pores of SU8 microframe.

The second method of preparation of binary organized microcomposites involves the infiltration with acrylic acid monomer followed by UV initiated polymerization (Figure 5.9). This in-situ polymerization of the acrylic acid results in a thin layer of PAA on the SU8 surface in addition to the holes being filled with PAA material (Figure 5.9). Pristine SU8 samples were treated with ethanol amine to reduce the hydrophobicity. The amine groups react with the uncrosslinked epoxy groups of the SU8, resulting in polar hydroxyl groups at the surface.[222] Following the ethanol amine treatment (which resulted in a decrease in the contact angle from 90° to 30°), the sample was thoroughly washed in Nanopure water and placed in a vial containing 1% acryloyl chloride in ethyl ether for 90 minutes. Then the sample was washed thoroughly and immersed

in a 20% acrylic acid solution with 5% UV initiator and 2% UV crosslinker (acryl amide), allowing acrylic acid solution to infiltrate pores. Finally, the sample was exposed to UV light (365 nm, 20 mW/cm^2) to initiate the polymerization of acryl amide.

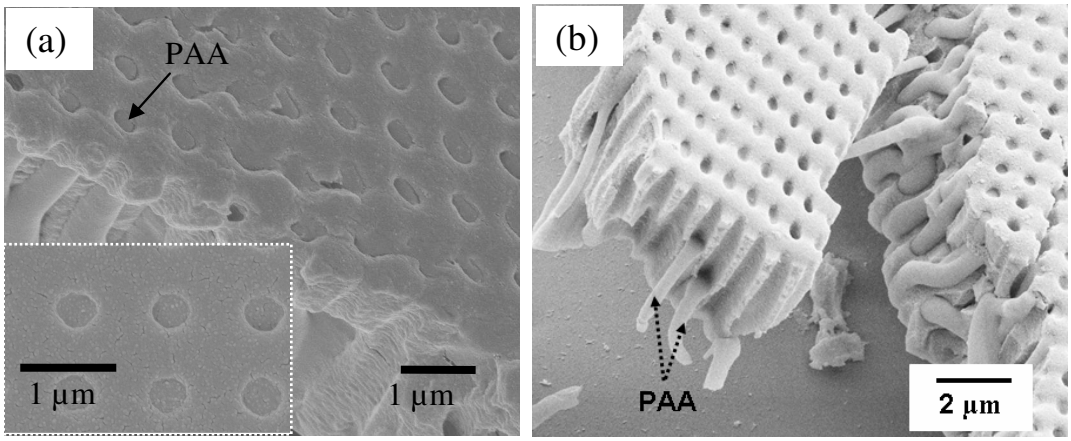

Figure 5.10: SEM images of SU8 microframe with in situ polymerized acrylic acid (a) top view showing the uniform infiltration over large area (b) Fractured microframe the complete infiltration though the entire depth of the pores.

Figure 5.10(a) shows the SEM image of the SU8 square lattice IL structure filled with PAA by the method described above. The inset of Figure 5.10(a) shows the closer top view of the filled pores. Apparently, PAA component uniformly filled the porous SU8 structure over very large areas. Intentional fracture of the PAA-SU8 binary microcomposite film confirmed the complete filling of the pores (entire 2µm thickness) with PAA material (Figure 5.10 (b)). The PAA component was shaped by the SU8 porous lattice in the form of 2µm long cylindrical structures with 380 nm diameter which can be pulled out during fracturing of the microstructure.

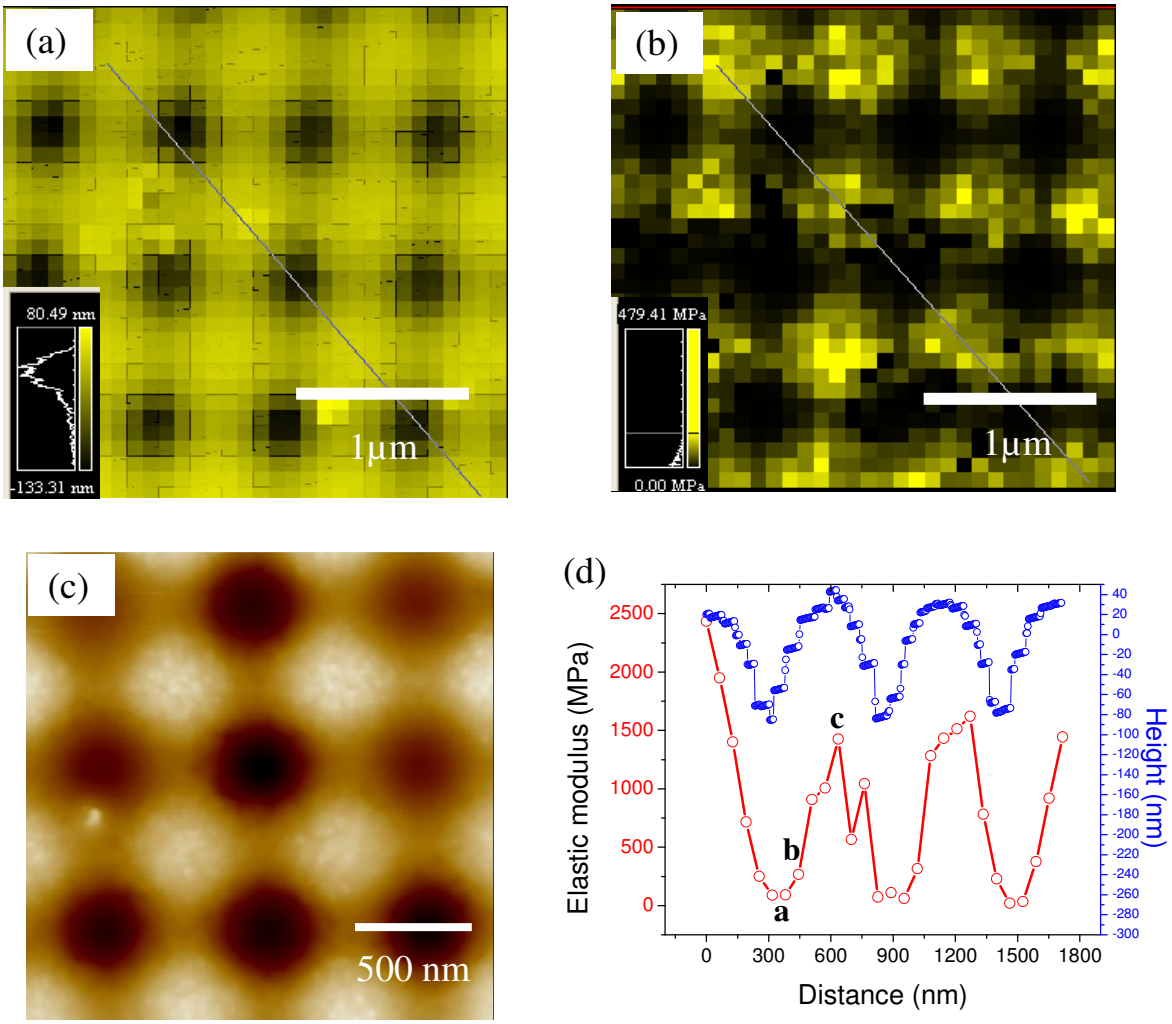

Figure 5.11: (a) AFM micromapping of the PB infiltrated SU8 square microframe: (a) 32x32 topography and (b) elastic modulus collected during force micromapping. (c) High resolution AFM topography image of the bicomponent microframe. (d) Height and elastic modulus along cross section along the line shown in (a) and (b)

5.5. Mechanical behavior of bi-component ITL structures

5.5.1 AFM micromechanical measurements

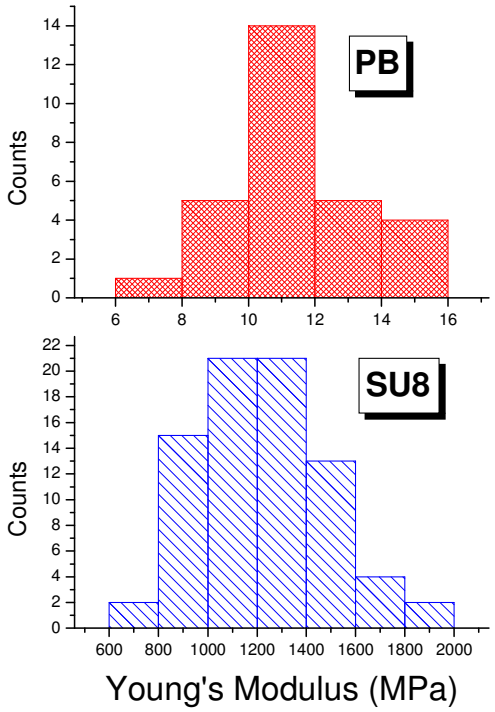

Figure 5.12: Histograms showing the elastic modulus distribution in the SU8 and PB regions.

AFM measurements on the SU8-PB binary microcomposites confirmed the templated periodic distribution of the different polymers. Figure 5.11(a) shows the high resolution AFM topographic image of the sample subjected to the AFM nanoindentation measurements. The height image of the SU8-PB structure confirms that the PB fills the pores with PB elevation remaining below the SU8 nodes, as evident from the 80 nm height difference between the SU8 nodes and PB within pores. Although the polymer solution during the capillary process completely fills the pores, subsequent solvent evaporation causes the polymer to shrink inside the pores.

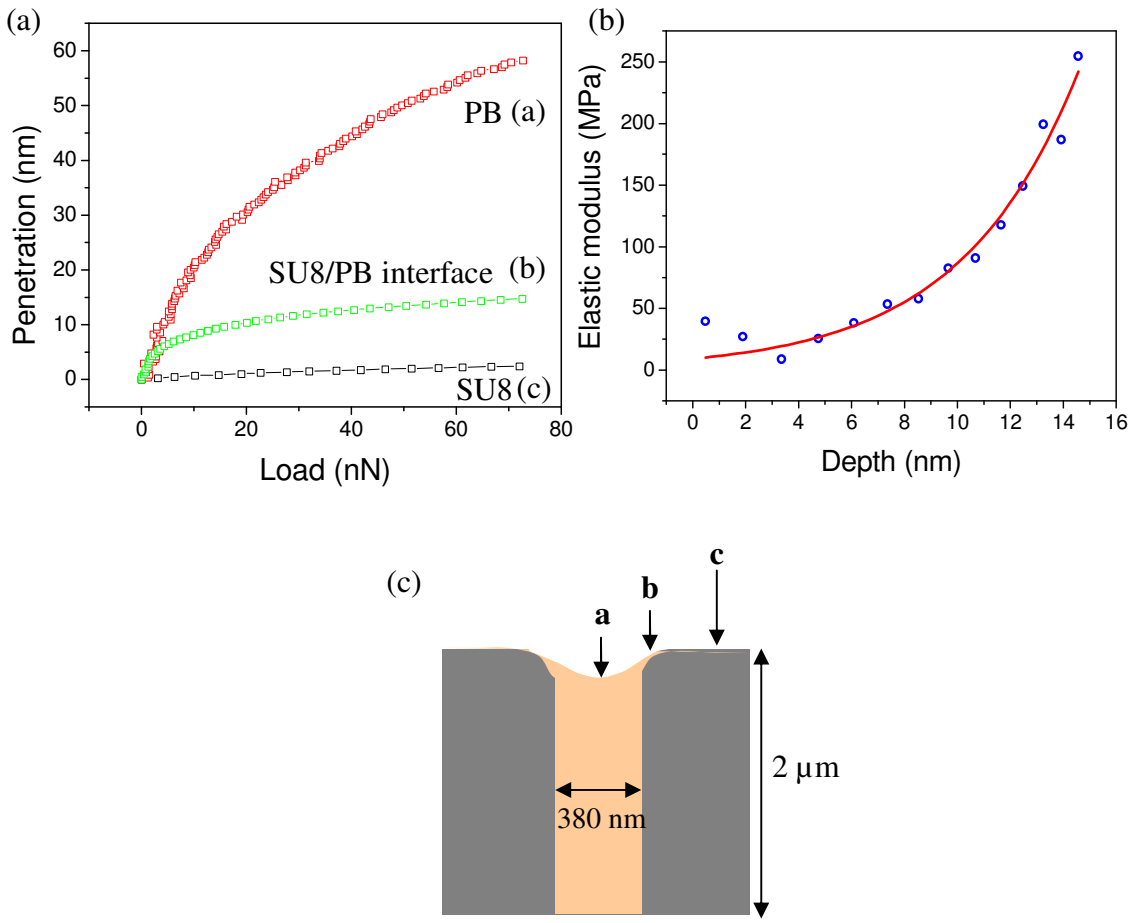

Figure 5.13: Representative load Vs penetration plots from three different regions (SU8, PB and interface) of the bicomponent microframe (b) Depth profile of the elastic modulus at the interface of SU8 and PB (along the edges of the pores) showing the increasing elastic modulus with indentation depth, indicating the layered nature of the interface. (c) Schematic representing the cross-sectional view of the PB in the SU8 pores showing the thin layer of PB on SU8 along the circumference.

Figure 5.11(b) and (c) show the height and the corresponding elastic modulus distribution of the bicomponent 2D microframe structure. The elastic modulus mapping shows that the SU8 regions possess much higher stiffness with an elastic modulus of 1200±250 MPa, similar to that measured for the pristine SU8 structure (see histograms for different phases in Figure 5.12). The PB-filled regions exhibit much lower elastic resistance with an elastic modulus of 12±2 MPa, which is close to that expected for conventional rubbery PB materials.[4]

Figure 5.13a shows the load vs. penetration data obtained from three different regions on the SU8-PB microcomposite: SU8 (I), PB (III) and interface between SU8 and PB (II) (see locations in Figure 5.13c). From the loading data, it is clear that the rubbery PB regions (PB phase is the pores) exhibit much higher elastic deformation compared to the interfacial regions, which in turn undergo higher deformation than that of the glassy material (Figure 5.13a). It is interesting to note that the initial portion of the SU8/PB indentation curve (5nm deformation) closely matches the pure PB phase and then exhibits a drastic change of slope. This drastic change in the slope of the loading curve indicates that the AFM probe encounters underlying material with higher stiffness during the indentation process.[211,215]

In fact, the depth profile of the elastic modulus shown in Figure 5.13 (b) shows a gradual increase of the modulus with the indentation depth, which is a clear indication of the bilayered, rubber-glass structure along the edges of the pores.[223] The regions along the circumference of the holes filled with PB exhibit an intermediate elastic modulus, ranging from the low elastic modulus of PB (about 12 Mpa) to a few hundred MPas (combined PB and SU8). This variation is caused by the interaction of the AFM tip with both materials in these transitions regions. Indeed, the cross section of the height and elastic modulus (along the lines shown in Figure 5.11(a) and (b)) demonstrate a gradual variation instead of abrupt transition around the pores (Figure 5.11(d)). The presence of PB phase at the edges of the nodes/holes resulted in the gradient of elastic modulus observed in this study and confirms the general schematics of distribution of glassy matrix and rubbery phase as presented in Figure 5.13(c).

5.5.2 Fracture behavior of rubber-filled glassy ITL structures

The peel test has been applied to study the fracture behavior of the PAA-SU8 binary microcomposite with 2D square symmetry. SEM images show the fractured areas of the PAA-SU8 sample exhibiting a fundamentally different deformation behavior compared to the original porous SU8 structure (Figure 5.14). Both the SU8 struts and the PAA domains are stretched during the crack propagation as can be seen in Figure 5.14 (b). For these organized microcomposites, the cracks propagate along the [1 0] direction of the square lattice similar to

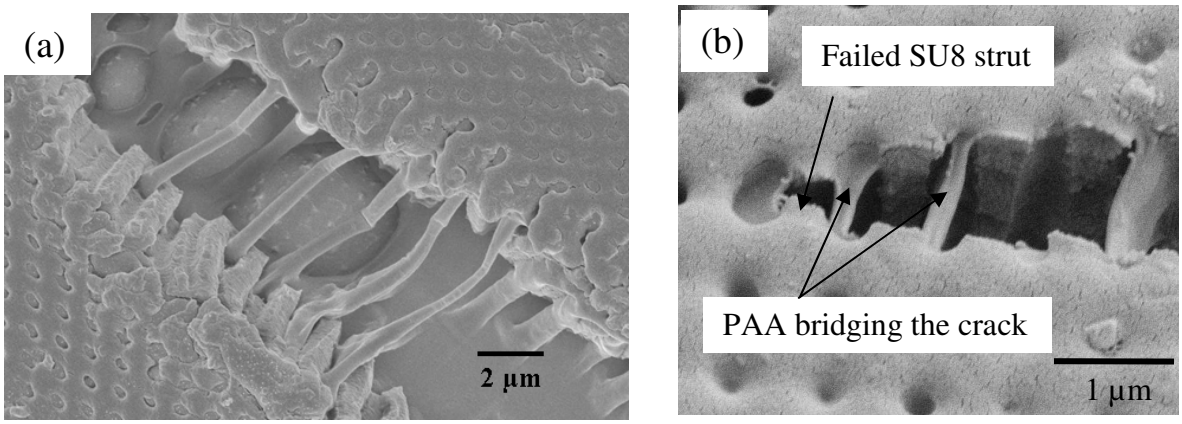

Figure 5.14. SEM images showing the fracture in bicomponent SU8-PAA structures (a) PAA inside the holes stretching and forming fibrils across the crack (b) Crack having to bisect the PAA domains for propagation leading to energy dissipation.

that discussed above, but the rubbery phase is stretched across the crack even at very high elongation after SU8 struts of the matrix failed (Figure 5.14 (a)). Rubbery PAA phase inside of cylindrical pores exhibits significantly higher deformation (300-400%) compared to the SU8 struts (up to 35% ultimate elongation). This way, the crack propagation is arrested by the stretched rubber phase bridging across the SU8 edges, resembling the known crazing phenomenon in conventional rubber toughened composite materials.[224]

The unique feature of the organized PAA-SU8 structure is that the crack follows the lattice direction, which connects the PAA phase inside of cylindrical pores. This stretching of the PAA phase beyond failed struts results in additional dissipation of strain energy in very different way

as compared to conventional microcomposites. In the case of the randomly distributed rubbery microphases, there are multiple random pathways in which the crack can propagate through glassy phase dissipating the least amount of energy and causing the macroscopic failure of the random microstructure. In contrast, for the organized bi-component rubbery-glassy structures discussed here, the crack's pathway through the rubbery-filled pores is predetermined by the matrix architecture, which could possibly maximize energy dissipation during crack propagation.

In the bicomponent microcomposites studied here, we have primarily observed that the PAA domains stretch as opposed to the cavitation in the conventional composites[4]. The possible reason for the absence of cavitation in bicomponent microcomposites studied here might be the length scale dependent mechanical properties of the SU8. It is known that one of the primary reasons for the cavitation of the rubber particles is the brittle nature of the surrounding matrix. In the case of the conventional rubber toughened composites, the rubber domains are separated by a few microns as opposed to the submicron separation in the case of the bicomponent microcomposite system. The epoxy matrix can undergo significant plastic yielding (35% strain, as estimated from tensile test) before failure as opposed to the brittle fracture (<2% strain) in the case of the conventional highly crosslinked epoxy matrix. Thus the length scale dependent mechanical behavior of the matrix (microframe) can result in fundamentally different energy absorption mechanism in multicomponent organized microcomposites. It is important to note that the rubber domains stretching and bridging across the crack is an efficient energy absorption mechanism. Quantitative characterization of the toughness of the rubber filled microcomposites at different strain rates and with varying pore sizes is a subject for further investigation to understand the energy dissipation characteristics.

In conclusion, the results described in this chapter demonstrated that organized porous microstructures with continuous open microscopic pores obtained via interference lithography

can be successfully utilized in the form of complex porous matrices for the fabrication of binary organized microcomposites with intriguing mechanical properties, such as lattice-controlled crack propagation and high energy dissipation due to multiple failures of struts and rubbery domains. Such organized glassy-rubbery microcomposites can find novel applications, which require precise control of the mechanical elastic and plastic behavior at micro and nanoscale.

CHAPTER 6

MECHANICAL INSTABILITIES IN CROSSLINKED PERIODIC POROUS SOLIDS

6.1 Introduction

Mechanical instabilities are ubiquitous phenomena observed at all length scales in a wide range of materials in both natural and manmade systems.[225,226,227,228,229,230, 231,232,233,234,235,236] Of various types of instabilities, such as wrinkling, fingering, snap-through, and Rayleigh instabilities to name a few, buckling is the most commonplace for elastic and elasto-plastic materials. For instance, reduction in the elastic energy due to out of plane periodic bending caused by either elastic compression or stretching manifests itself in a wide range of phenomena such as wrinkling of the skin, textured cream on milk, and the edges of leaves. Buckling instabilities in metals, ceramic and polymeric thin films have received intense attention in the last few years. Thin film buckling phenomenon has been exploited as a novel metrology technique for measuring elastic moduli of nanoscale polymeric films, composite nanomembranes, as well as 1D and 2D nanostructures, for which conventional mechanical testing approaches cannot be readily applied.[229,230,231,233,234]

Buckling instabilities have also been demonstrated to be valuable in controlling adhesion, enabling flexible electronics, fabricating microfluidic structures, providing means for micro and nanopatterning and optical microdevices based upon micrograting. [237,238,239,240,241] Very complex and highly localized buckling instabilities patterns have been achieved in thin metal and polymer films by various techniques such as patterning metal nanoparticles in polymer films, local oxidation of the elastomeric substrate. This phenomenon led to a patterned hard

skin or patterned adhesion between the film and substrate well-controlled by local mechanical stress distribution.[225,230,242]

Among recent novel structured materials, microscopic analogs of periodic cellular structures in which the periodicity and the pore size are in the sub-micron scale are gaining interest as prospective base for a wide variety of applications ranging well beyond structural materials. Current and prospective applications of these structured materials (sometimes called microframes) include 3D photolithography, photonic and phononic band gap materials, microfluidic networks, porous biomaterials as tissue engineering scaffolds and DNA-protein microarrays. [243,244,245,246,247,248,249] When subjected to external stresses caused by direct mechanical loading or internal stresses due to changes in osmotic pressure, or differential thermal expansion, or partial swelling, the periodic porous microstructure can become unstable at a certain critical stress. Such mechanical instability might lead to dramatic transformation of the initial periodic structure, a phenomenon rarely addressed and rarely discussed on a quantitative level.

While the buckling in thin films results in highly periodic surface relief patterns, buckling in periodic porous and bi-component materials might result in much more complicated pattern transformation.[250] Indeed, peculiar and reversible pattern transformation in periodic elastomeric structures subjected to a simple load has been already uncovered[235,251,252] and intriguing deformational behavior and fracturing of periodic solids has been reported. [253] Furthermore, the instability in surface relief elastomeric structures has been employed to pattern nanoparticle distribution.[254] We have recently demonstrated the pattern transformation in porous elasto-plastic solids following the polymerization of rubbery component in the pores which resulted in the pore collapse.[255] We discovered the intriguing pattern of buckling instabilities initiated by the

compressive stresses generated inside the cylindrical pores by rubbery materials grafted to the walls in the course of its polymerization and solvent evaporation.

In this chapter, we describe in detail the triggering and mechanistic aspects of such instabilities responsible for pattern transformation in periodic porous elasto-plastic solids. The porous, periodic, solid polymer structures with different symmetries employed here have been fabricated with multiple laser beam interference lithography (IL) from a negative photoresist.[256] The surface morphology of these transformed materials was studied with atomic force microscopy (AFM) and internal stress distribution in the transformed structures has been addressed by confocal Raman microscopy. Furthermore, we demonstrated the micropatterning of such mechanical instabilities in periodic, porous solids by confining the compressive stresses to predetermined locations. The confinement of the compressive stress in one and two dimension resulted in higher order, complex microscopic periodic porous structures as discussed here in great detail. Numerical simulations with non-linear finite element analysis (FEA) were employed to better understand the mechanics of the experimentally observed pattern transformation and elucidate the role of general and localized compressive stress distribution and coupled buckling-rotation of microstructural elements. Finally, we demonstrated the precise replication of the topographical features of the transformed pattern in polystyrene using soft lithography approach.

6.2 Experimental details

Fabrication of SU8 microframes: 2D square and hexagonal patterns were fabricated using multi-beam IL according to the usual procedure.[267] The fabrication involved a 2-step sequential,

double exposure with a 90° rotation of the sample to the interference pattern of two equal intensity laser beams for the square lattice and single exposure to the interference pattern of three equal intensity laser beams for hexagonal lattice. The transfer of the light intensity pattern into an SU8 photoresist platform via laser-initiated cationic polymerization results in each 2D patterned structure. The Gaussian output from the laser was cleaned up and expanded using a spatial filter and re-collimation setup.

The materials platform consisted of Epon-SU8 (Miller Stephensen) as a photoresist (a multi-functional epoxy derivative of a bisphenol-A Novolac), H-Nu 470 (Spectra group) as a photosensitizer which absorbs the visible light and electron transfers to an onium salt, octoxyphenylphenyliodonium hexafluoroantimonate (OPPI) (UCB Radcure) as a photoacid

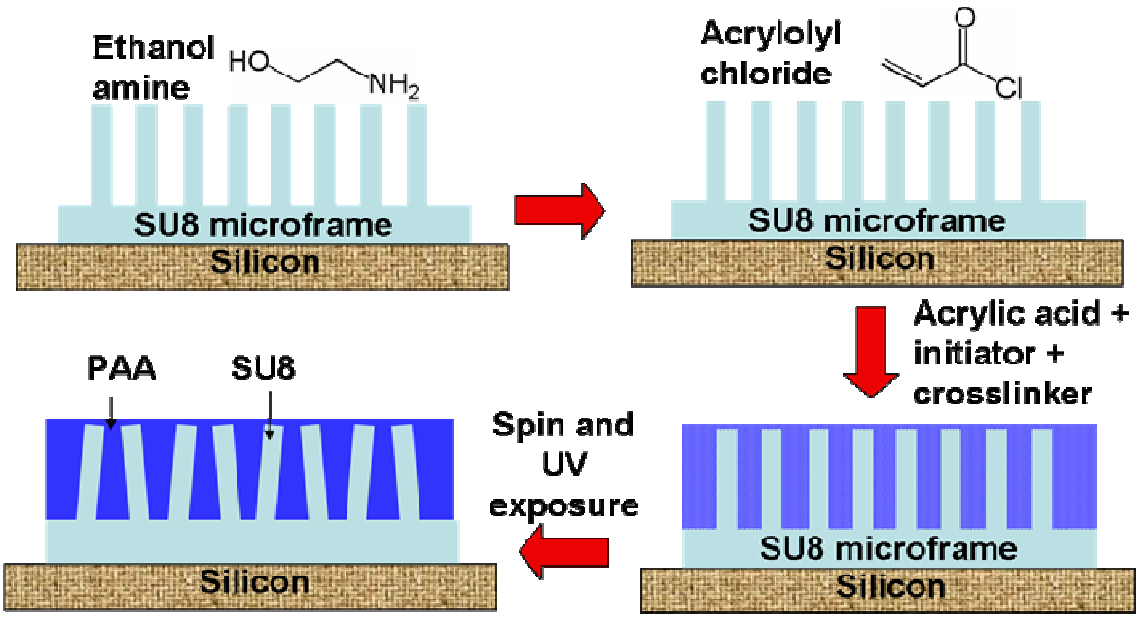

Figure 6.1: Process steps involved in the in-situ polymerization of the acrylic acid in the SU8 structures.

generator, and trioctylamine to compensate for the non-zero background arising from the interference intensity. The glass substrate was treated with a thin (700 nm) buffer layer of pre-crosslinked SU8 material to assure attachment of the structured polymer film to the substrate

via chemical grafting. A 3 µm thick SU-8 film was subsequently spin-coated on top of the existing crosslinked SU-8 film at a spin speed of 2000 rpm. The IL exposure was done using a 532 nm cw Nd:YAG laser with an intensity of 1.5 W for 8 -15 seconds to give the total exposure dose of 12-22 J/cm^2. After baking the 3 µm thick film at 75 ºC for 3 min, the resultant cationic photopolymerization only takes place in regions that were exposed to high intensities of light. The uncured regions are developed away in PGMEA (propyleneglycol monomethylether acetate) followed by rinsing with isopropanol. No further heat treatment is applied. The glass transition temperature of the SU8 cured under similar conditions (including the 5 min UV exposure during the acrylic acid) was found to be 120° C from the DMA measurements.

In situ

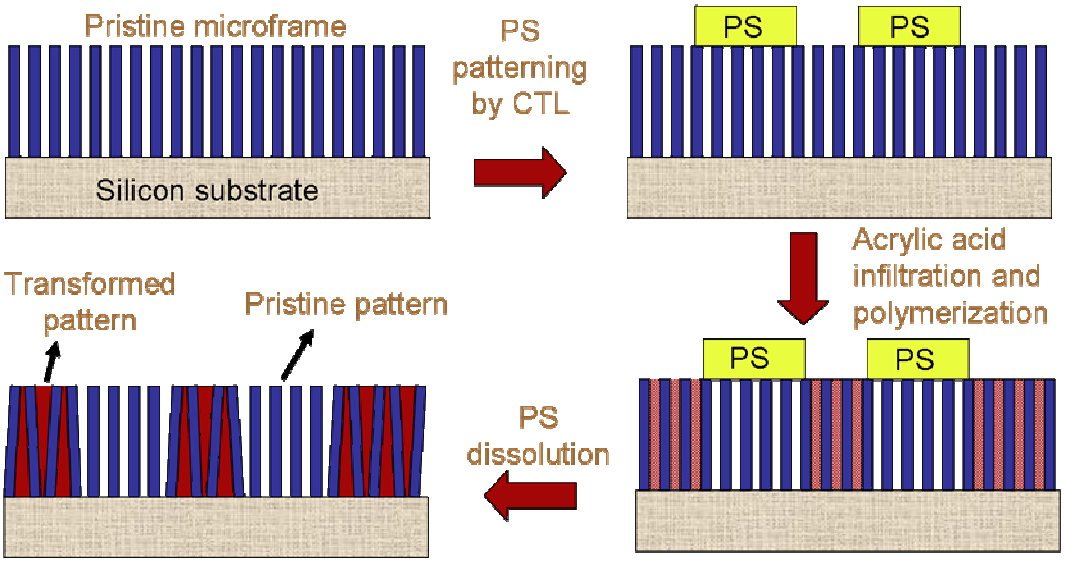

Figure 6.2: Schematic of experimental routine for patterning the instabilities which involves in stamping polystyrene pattern for block acrylic acid infiltration followed by acrylic acid polymerization.

polymerization of acrylic acid in submicron pores: To fabricate filled microstructures (Figure 6.1), pristine microframes were treated with ethanol amine to reduce the hydrophobicity and induce surface hydroxyl groups.[257] Following the ethanol amine treatment (which resulted in a decrease in the contact angle from 90° to 30°), the sample was thoroughly washed in Nanopure water and placed in a vial containing 1% acryloyl chloride in ethyl ether for 90 minutes. AFM

imaging at this stage in various locations of the sample revealed no signs of transformed pattern. Then, the sample was washed thoroughly and immersed in a 20% acrylic acid solution with 5% UV initiator and 2% UV crosslinker (acryl amide), allowing acrylic acid solution to infiltrate pores. Finally, the sample was exposed to UV light (365 nm, 20 mW/cm^2) to initiate polymerization of AA. The pH of the monomer with initiator and crosslinker was 2.3 keeping the carboxylic moieties on the PAA are in neutral state. The crosslinked PAA materials filling the micropores is in a swollen state in water (73%).

Patterning instabilities: To localize and pattern the instabilities, patterns of polystyrene were employed as physical mask on the microframe to prevent acrylic acid infiltration into the desired pores (Figure 6.2). The samples were treated with ethanol amine to reduce of the hydrophobicity and stamped with a pattern of polystyrene (with10 µm periodicity) using capillary transfer lithography (CTL) illustrated in Figure 6.2.[274,275] In brief, a PDMS stamp (with 10µm periodicity) was soaked in toluene for 1–2 minutes and brought into conformal contact with the polystyrene film on the PDMS substrate (swollen in toluene) and pressed for one minute. The polystyrene infiltrated the receding portions of the PDMS stamp by capillary action. The pattern was then transferred onto the microframe surface by contact of the PDMS stamp for 1 min.

Numerical simulations: FEA calculations were conducted within the nonlinear code ABAQUS/Standard, version 6.6-1. In the numerical analyses an infinite array of circular holes has been considered in the x1-x2 plane parallel to the holes, so that the analyses could be conducted both on the primitive cell and on multi-cell representative volume elements (RVEs). To respect the periodicity of the structure a series of constraint equations were applied to the surfaces of the primitive cell (not on the top and bottom surface) providing general periodic boundary conditions.[258] The square array is composed of cylindrical pores with a radius R=190 nm and a primitive cell Y defined by the lattice vectors v1= [830 0] nm and v2= [0 830] nm. The oblique array with a radius R=200 nm is spanned by v1= [1000 0] nm and v2= [500 1000] nm

(Figure 6.3). The stress-strain behavior of the material (photocrosslinked epoxy SU8) is captured using a rate independent elastoplastic model, since the small rate dependency recently observed does not influence the pattern transformation.[259,260] The initial Young's modulus has been measured to be 1300 MPa and the Poisson's ratio is taken to be 0.33. The other material parameters are derived from values recently measured, taking them to linearly scale with the initial Young modulus. A Mises yield surface and isotropic hardening are used with a yield stress of 60 MPa and a strain hardening modulus of 300 MPa.[260]

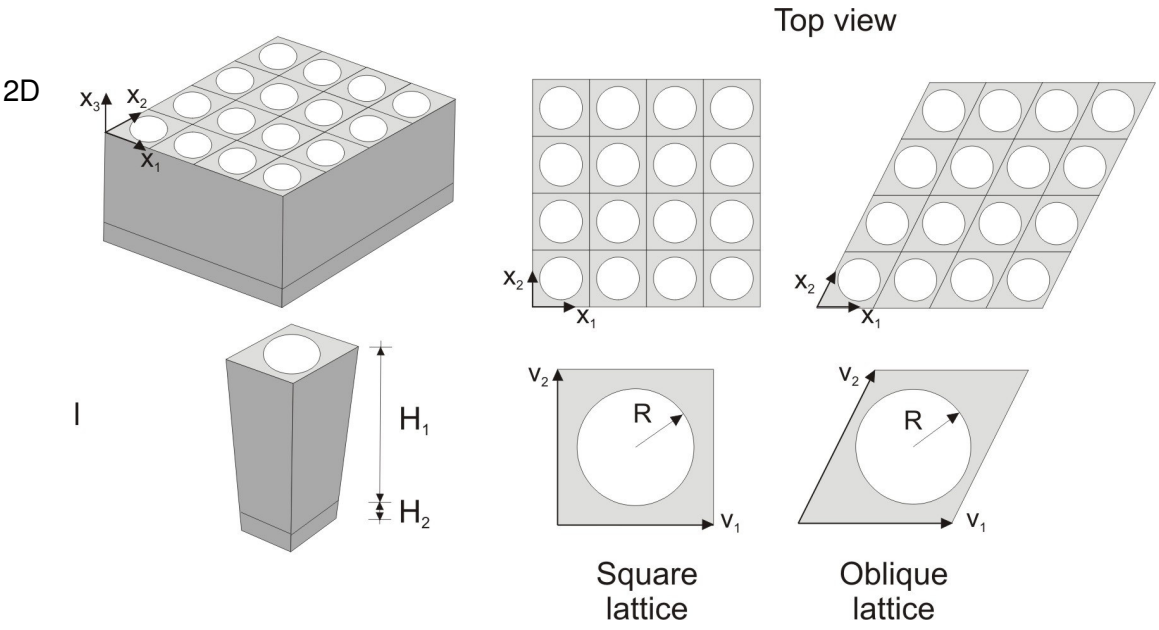

Figure 6.3: 4x4 periodic representative volume elements (top row) and corresponding primitive cells (bottom row) for square and oblique arrays of cylindrical pores.

models under plane strain conditions were used to investigate instability performing Bloch wave analyses.[235,258] The mesh was constructed of 6-node, quadratic, 2D elements (ABAQUS element type CPE6H) and a pressure was applied to the void to mimic shrinkage occurring after evaporation of the water. 3D models using 15-node, quadratic, hybrid elements (ABAQUS element type C3D15H) were then constructed and the mesh was perturbed using the critical eigenmode obtained from the Bloch wave analysis. In the 3D models the pores are considered

to be 3 µm long in the x3 direction and the porous structures are bonded to a substrate that is 700 nm thick. In correspondence with the periodicity of the transformed patterns, RVEs consisting of 2x2 and 1x2 primitive cells are considered to simulate the stress-strain response of the square and oblique arrays, respectively.

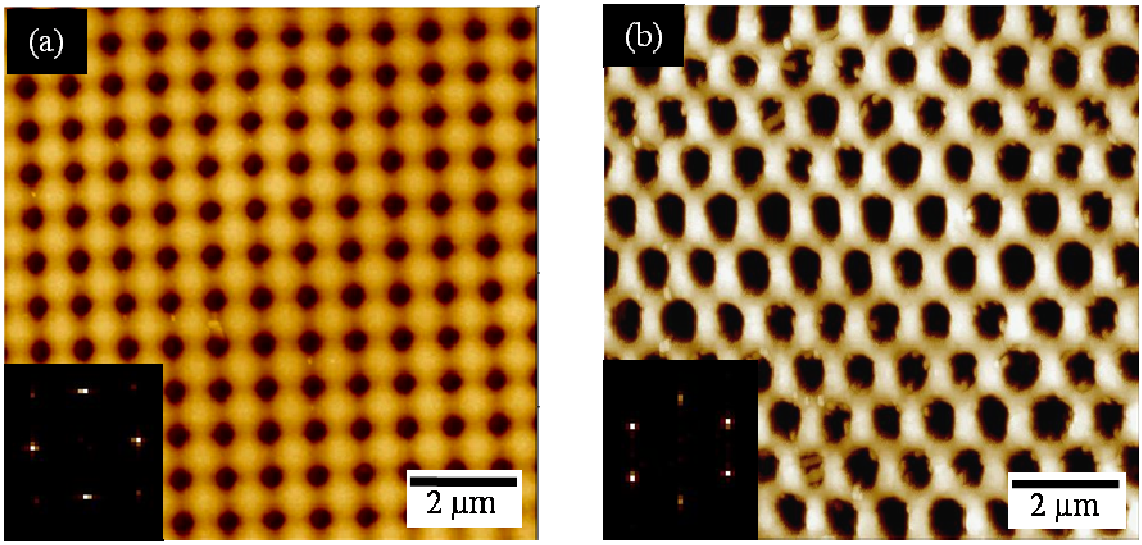

Figure 6.4: AFM images of the pristine microframe structure with (b) square and (c) oblique lattices and corresponding FFT patterns (insets).

The morphology of the pristine and patterned microframes was studied with a Dimension 3000 Atomic Force Microscope (AFM) according to the procedure adapted in our lab.[261,262] Field-emission scanning electron microscopy (FESEM, LEO 1530) was used to investigate the pattern transformation in the microframe structures. Raman measurements were performed on both pristine and transformed SU8 structures using Alpha 300R Witec Confocal Raman microscope. Raman measurements were conducted using an Argon laser at 514.5 nm with the incident power below 4 mW. The average spectrum from struts and nodes were obtained by averaging over 40 individual spectra from different locations.

6.3 Results and Discussion

The periodic porous polymer structures studied here have been fabricated with IL from a common negative photoresist, epoxy derivative of a bisphenol-A Novolac photocurable resin, SU8, which is widely utilized in photolithography technology. [263,264,265,266]

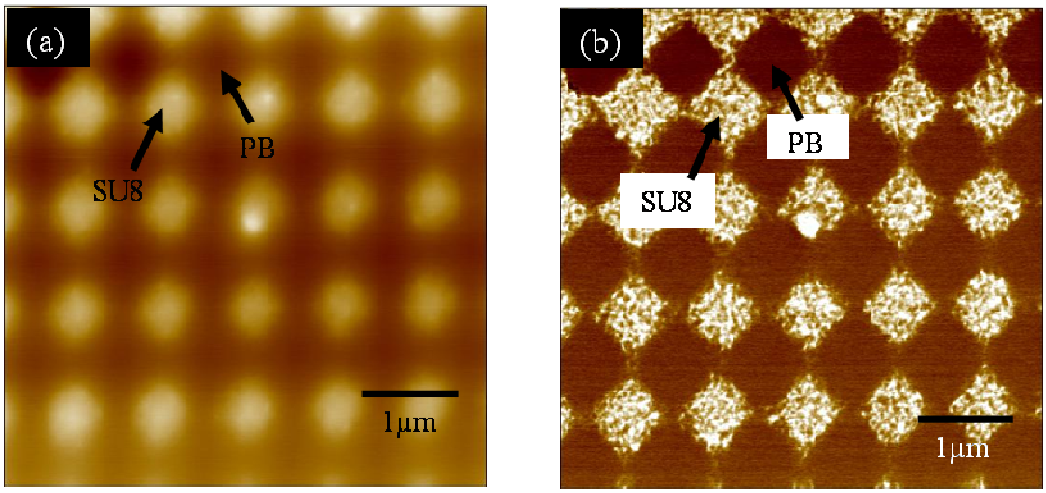

Figure 6.5: AFM image of square porous SU8 structure filled with PB by capillary infiltration method ((a) topography and (b) phase) showing the distinct rubber and glassy phases organized in a checkerboard pattern.

Figure 6.4 a, b shows the AFM images of the pristine microframes with the corresponding 2D FFTs (as insets) reflecting the square lattice symmetry of cylindrical pores. The periodicity of the square lattice was 830 nm, the radius of the cylindrical pores was 190 nm and the porosity was 20% as determined from AFM and SEM studies. The corresponding oblique lattice microframe fabricated in a similar manner had a periodicity of 1 μm, a radius of 200 nm and a porosity of 35%. The thickness of the microframe structures was 3 μm, making the aspect ratio to be nearly eight. AFM nanomechanical measurements showed the average modulus of the SU8 IL structures to be 1.3 GPa with higher elastic modulus for nodes and continuous gradient of crosslinking density along struts. [267,268]

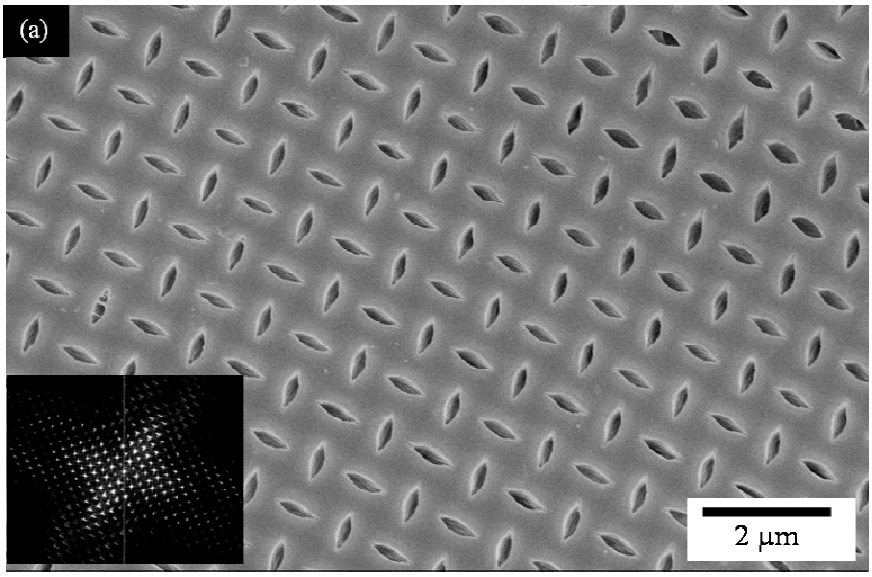

Figure 6.6: SEM images of transformed pattern of square lattice showing the large scale uniformity of the transformed pattern. Insets show the FFTs of the transformed pattern.

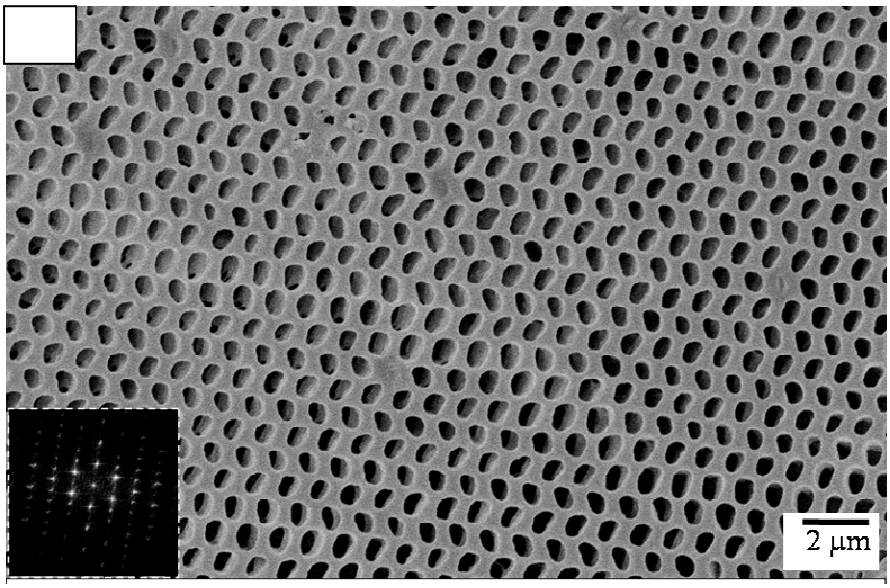

Figure 6.7: SEM images of transformed pattern of oblique lattice showing the large scale uniformity of the transformed pattern. Insets show the FFTs of the transformed pattern.

We verified that conventional filling of the SU8 microframe porous structure with a rubbery

phase by employing spin coating and capillary driven infiltration from 2% polybutadiene (PB) solution does not affect the initial porous SU8 structure.[267] AFM images shown in Figures 6.5 a, b (topography and phase) clearly demonstrated the finely separated PB microphases localized within the pores forming a characteristic checkerboard pattern. Neither the shape nor the size of the pores exhibited any noticeable changes following the infiltration process.

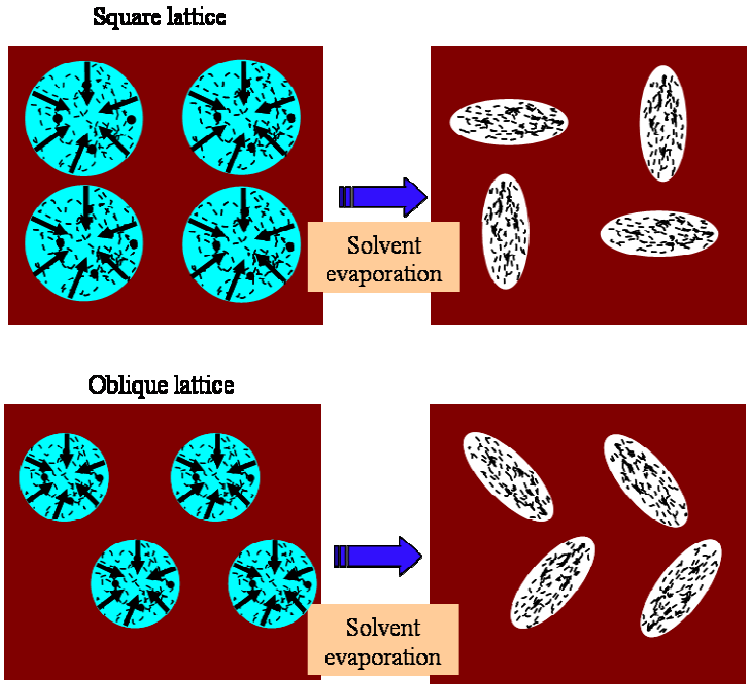

Figure 6.8: Schematic depicting the transformation in square and oblique lattice.

In a sharp contrast, *in situ* solution photopolymerization of acrylic acid monomer performed directly in the cylindrical pores results in grafting of the polymer to the SU8 walls and eventually in complete reorganization of the initial porous structure (Figure 6.6, 6.7). In has been demonstrated that the trace amounts of triarylsulfonium hexafluoroantimonate (initiator) which remains within cured SU8 acts as a source of free radicals, initiating UV-mediated grafting of PAA onto the surface of the SU8.[269] Figure 6.1 illustrates the surface modification, infiltration of the monomer and subsequent polymerization of the acrylic acid in the pores of the SU8

structure. The slow evaporation of the water from inside of open cylindrical micropores causes the swollen PAA network grafted to the pore walls to shrink significantly resulting in high compressive stresses. These stresses resulted in a dramatic transformation of the periodic circular holes to ellipses in the case of the square lattice and sheared ellipses in the case of the oblique lattice as is discussed below (schematically shown in Figure 6.8).

As a result of this transformation of porous structure, a dramatically different lattice with perfectly regular, non-trivial geometry was observed across the macroscopic surface area (Figure 6.6). The initial square array of cylindrical micropores has been transformed into periodic, mutually orthogonal, highly collapsed elliptical pores. Transformed regions are extremely uniform extending to surface areas up to few millimeters. On the other hand, the oblique lattice has been transformed into an array of sheared pores with the shear direction alternating back and forth from row to row resembling a common herringbone pattern (Figure 6.7).

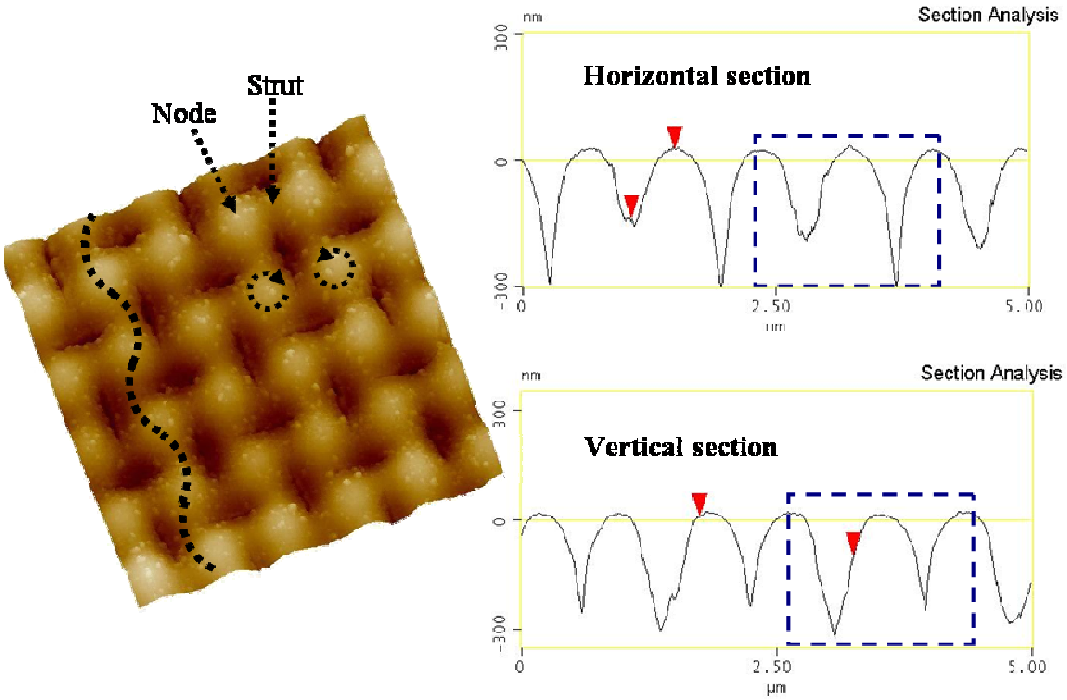

Figure 6.9: AFM topographical image (5X5 µm) of the transformed pattern showing the deformation modes of the struts (bending) and the nodes (rotation) on square lattice and the cross-sections along the (01) and (10) directions showing the double bump morphology.

The AFM image depicted in Figure 6.9 identifies the nodes (elevated round areas) and struts (ridges connecting nodes) of the square lattice microframe structure. At a microscopic level, the pattern transformation can be related to bending of the struts in alternate directions (along x_1 and x_2) and the rotation of the nodes in clockwise and anticlockwise directions[251] as indicated on the AFM image (Figure 6.9). The resulting instabilities are frozen after transformation and can be relaxed only after extended annealing at temperature close to glass transition temperature of SU8. The pattern of alternating elliptical micropores is identical along x_1 and x_2 directions with characteristic, double-bump shape reflecting alternating depth of the AFM tip penetration along short and long axes of the collapsed pores caused by its interaction with narrowing, slit-like pores (Figure 6.9, see cross-sections in different directions).

6.3.1 Numerical analysis of mechanical instabilities

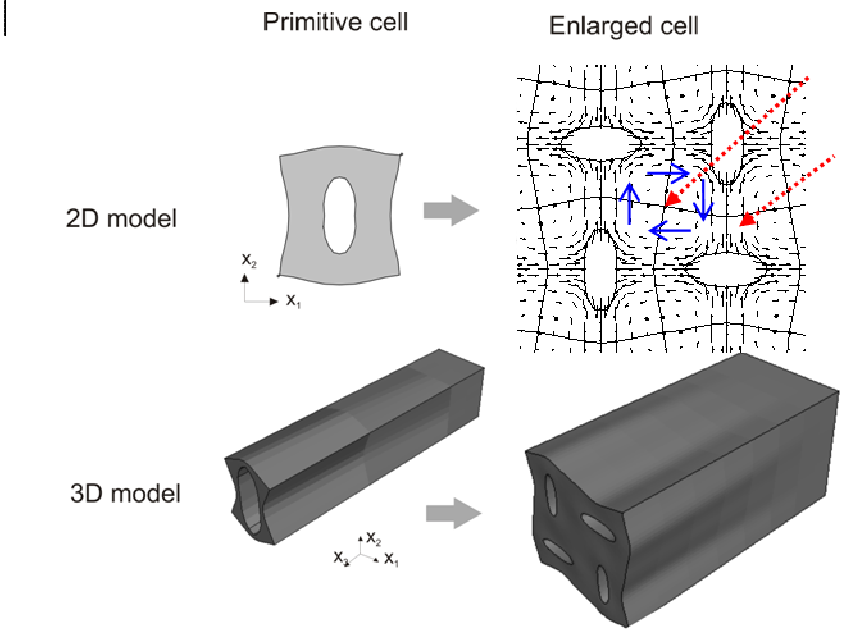

Figure 6.10: Eigenmode of the microscopic instability for the infinite square array of circular holes as predicted by the Bloch wave analysis and the displacement field with arrows showing direction of local displacements (top). The transformed pattern as obtained from the 3D analysis is showed on the bottom.

For further insight into the mechanics of the pattern transformation observed here, numerical investigations of the behavior of the periodic microporous solids were conducted utilizing nonlinear FEA. [235,251] First, the instabilities of the infinite periodic porous solid are investigated conducting Bloch wave analyses and then load-displacement analyses are conducted to capture the critical transformation event and the post-transformation behavior.[270]

The bifurcation FEA analysis demonstrates that indeed during the initial deformation, at a critical point the square array of cylindrical pores undergoes an instability transformation. This symmetry change results in a four times enlarged representative cell now consisting of two primitive cells in both lattice directions (Figure 6.10). The displacement field calculated for such

a compression confirms the rotation of the nodes and the resulting buckling of the struts as was suggested from AFM imaging (Figure 6.9). The oblique array is characterized by a critical instability as well resulting in an enlarged representative cell now consisting of one primitive cell in the horizontal direction and two primitive cells along the other lattice direction (Figure 6.11).

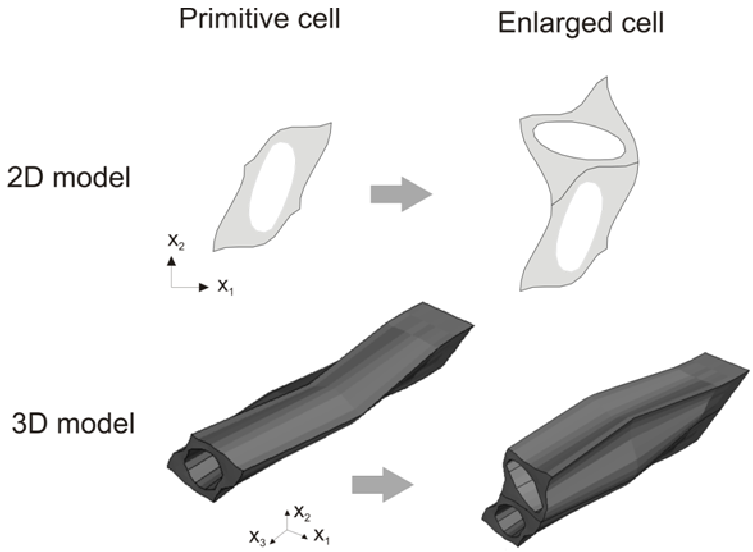

Figure 6.11: Eigenmode of the microscopic instability as predicted by the Bloch wave analysis (top) and transformed pattern as obtained in the 3D analysis (bottom) for the oblique array of circular holes.

The variation of the eigenmode through the thickness of the specimen for the square array confirms that the transformed pattern gradually develops through the thickness and corresponds well to the SEM image of the transformed structure (Figure 6.12). Such a vertical gradient is caused by the constraint generated by the substrate on the lateral deformation in the vicinity of the buffer layer. Furthermore, the same critical eigenmode is detected at the same macroscopic strain level both when the bottom surface is fixed only in x_3 direction and in all three directions, suggesting only a small influence of the boundary constraint on the behavior of the porous solids at distance larger than 1/3rd of the total thickness. It is worth noting that a gradient

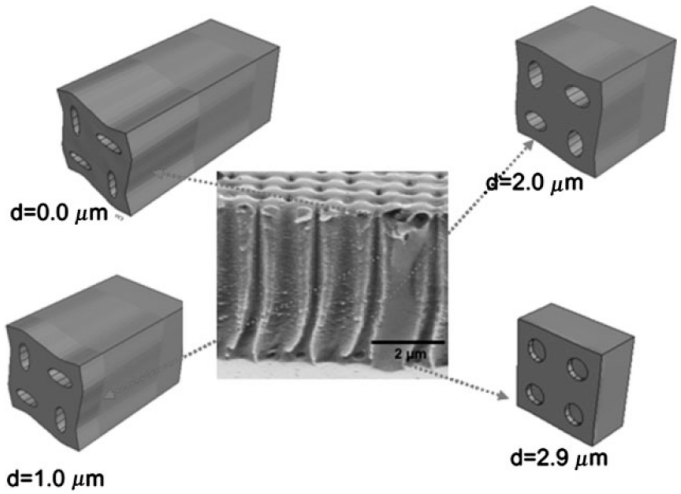

Figure 6.12: View cuts along the x1-x2 plane at different distances from the top surface and a cross-sectional SEM image of an intentionally fractured microframe depicting the vertical gradient (some shearing is caused by specimen preparation for SEM).

transformation along the thickness was suggested earlier (but not confirmed experimentally) as a main cause of pattern transformation of swollen porous elastomers.[254]

6.3.2 Internal stresses probed by confocal Raman microscopy

The dual (elastic-plastic) nature of the SU8 material deformation locks in the mechanical instabilities after the release of the external stress with internal stresses dissipated to a great extent as was confirmed by Raman spectroscopy.[271] Mapping of peak intensities with confocal Raman microscopy, sensitive to local stresses, confirmed uniform distribution of internal stresses with similar pattern in pristine and the transformed patterns. Figure 6.13a shows the confocal Raman map of the intensity integrated over 1550 cm^{-1} and 1650 cm^{-1} of the pristine and transformed patterns. The Raman peak positions and their relative intensities which are sensitive to active bond vibrations did not exhibit any significant observable changes between the pristine and transformed solids (compare major bands at 1600 cm^{-1} (backbones, C=C

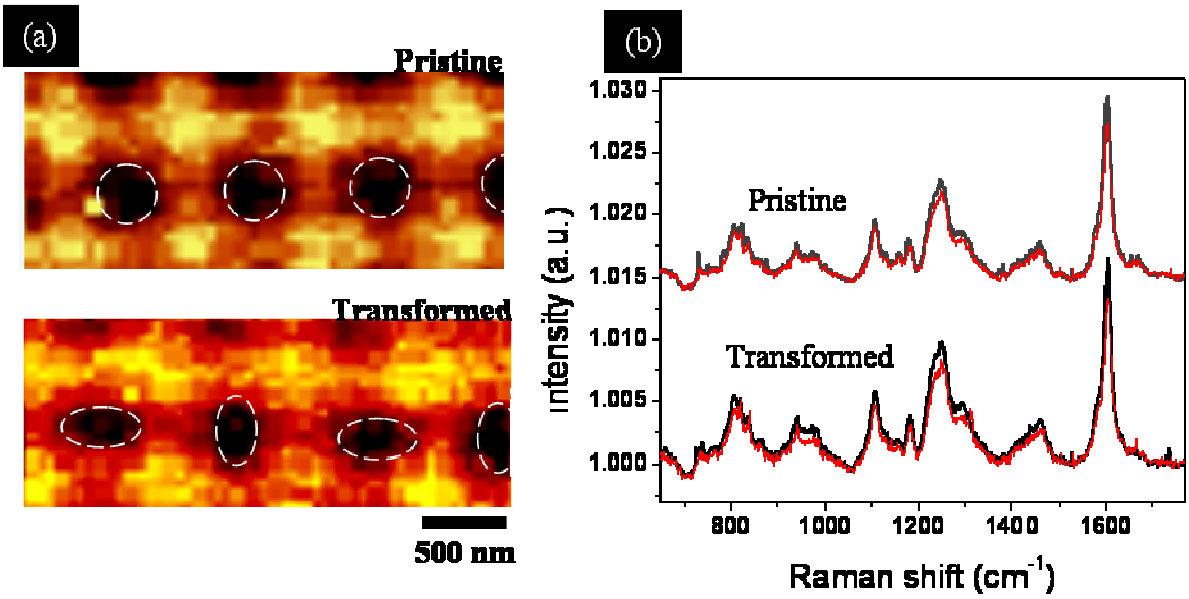

Figure 6.13: (a) Confocal Raman intensity mapping (integrated between 1580 and 1620 cm^{-1}) of the pristine and transformed patterns (pixel resolution of about 200 nm limits the visual appearance) and (b) average Raman spectra of nodes (black) and struts (red) obtained from the pristine and transformed patterns.

stretching) and at 830 cm^{-1} and 1250 cm^{-1} (epoxide ring vibration and ring stretching respectively) (Figure 6.13b).[272,273] Such a similarity suggests a complete relaxation of the stresses for both nodes and struts after the transformation completed and locked. It is worth noting that this observation is in sharp contrast with the instabilities in elastomeric solids, in which the transformed structures exhibit stress concentration in localized areas.[251]

6.3.3 Confinement of mechanical instabilities

The extent of the pattern transformation across the entire structure can be controlled by localizing the compressive stress in certain areas. Such localized stresses can be achieved by filling predetermined areas of porous structure with acrylic acid monomer solution while preventing the infiltration into the other pores. Capillary transfer lithography (CTL) has been employed for selective depositing a polystyrene pattern with a periodicity of 10 μm (7 μm wide polystyrene stripes alternating with 3 μm gaps) for selective blocking of certain areas.[274,275]

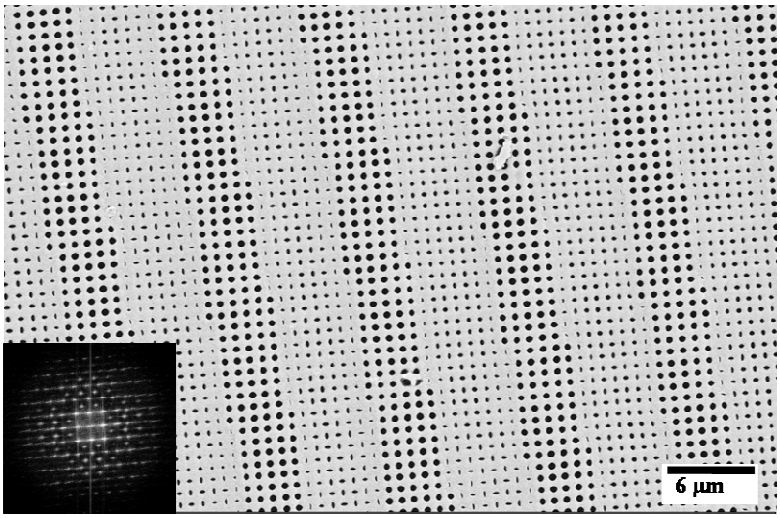

Figure 6.14: SEM image depicting the large scale periodic confinement of the mechanical instabilities causing regular transformation pattern.

Figure 6.2 illustrates the steps involved in the confined polymerization of the acrylic acid in predetermined, micropatterned areas. As expected, the photopolymerization in the exposed areas (3 µm wide) resulted in the localized transformed superlattice pattern with periodicity of 10 µm as determined by microstamp spacing (Figure 6.14). The SEM image in Figure 6.14 clearly demonstrates the array of mutually orthogonal elliptical pores (transformed areas) interleaved with the array of circular pores (intact areas) with extremely sharp transition zones between these two regions as discussed below.

Figure 6.15a shows the higher magnification AFM images of the confined pattern transformation resulting in a hybrid (coexisting pristine and transformed regions) porous structure when the confining polystyrene pattern was parallel to the (10) direction of the microframe square lattice. The AFM image reveals narrow regions with high deformation running at ~45º to the lattice direction, releasing the stress caused by overall shrinkage of the volume due to the lateral confinement of transformation to certain localized regions. The cross section along the line

shown in the AFM image depicts the alternating single bump (pristine regions) and double bump morphology (transformed regions) (Figure 6.15 b).

The transition between the pristine and transformed regions in this case is rather sharp,

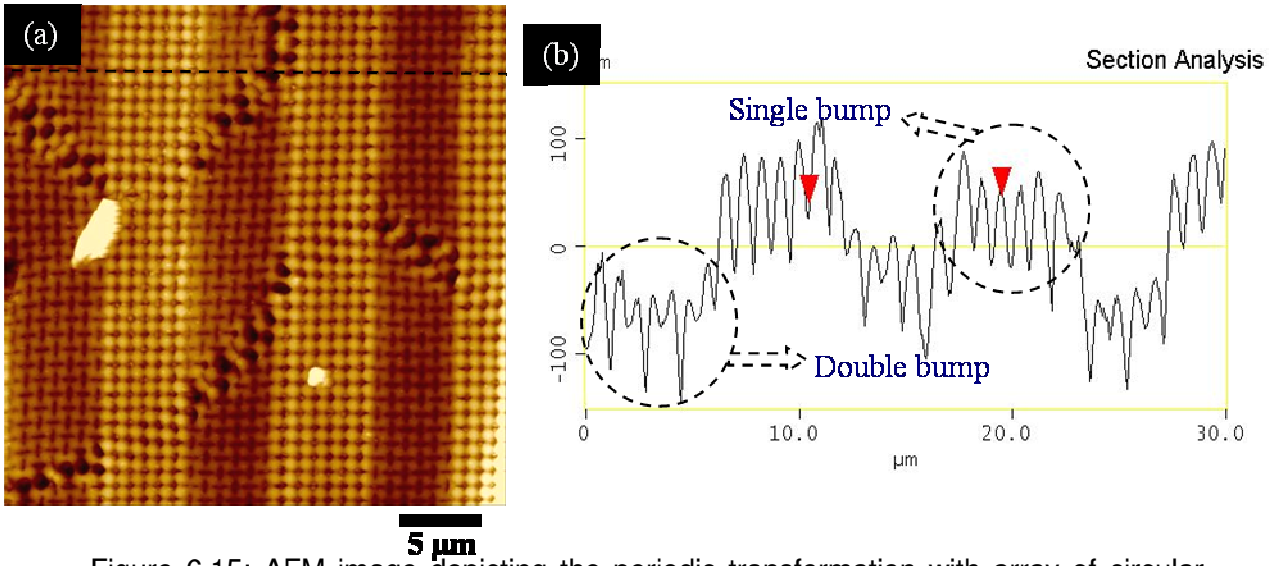

Figure 6.15: AFM image depicting the periodic transformation with array of circular holes interleaved with array of mutually orthogonal pores (a) polystyrene pattern aligned with the (10) direction of the microtruss pattern (b) cross-section along the horizontal line (shown on the AFM image) of the interleaved pattern showing the alternating single bump and double bump structure.

switching from pristine to transformed regions within one unit cell. On the hand, when the polystyrene micropattern was slightly misaligned (by 20º) to the lattice structure ((10) direction), the interface of the pristine and transformed region exhibits a diffused transition with an intermediate topology between the pristine and transformed pattern (Figure 6.16a, b). The stress release in this case occurs by the plane buckling in the form of narrow ridges inbetween the pristine and transformation regions, as evident from the AFM image (Figure 6.16a). The pristine regions are narrow (~5 µm) compared to the width of the polystyrene pattern (7 µm), possibly due to the undercutting of the acrylic acid into the pores at the boundary or from the compressive stresses at the interface.

One important feature common to both of the confined samples was the compression of the transformed regions along the normal direction as compared to the pristine regions as apparent from 3D topography of the micropatterned porous structure and the corresponding cross section (Figure 6.16a, b). In fact, the cross section analysis reveals that the transformed regions were compressed by ~150 nm (corresponding to 5 % strain) in the vertical direction compared to the pristine porous regions (lower regions in Figure 6.16b). The vertical compression is due to the

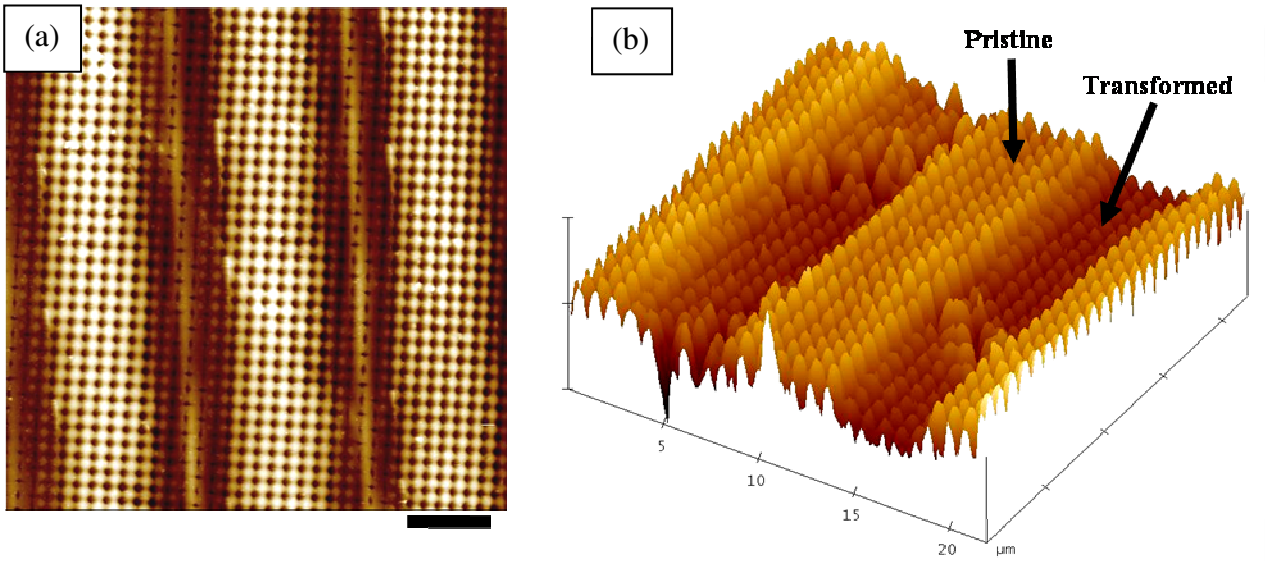

Figure 6.16: (a) AFM image of the confined pattern transformation when the polystyrene pattern slightly (20º) misaligned with respect to (10) direction. (b) 3D AFM image depicting the vertical compression in the transformed areas compared to the pristine areas.

vertical component of the stress exerted during the isotropic collapse of the PAA network during the solvent evaporation. It is worth noting that in recent studies of pattern transformation in elastomers the authors suggested, but did not prove, the vertical compression in the areas of the pattern transformation.[254] The patterning of instabilities achieved in this study clearly revealed such significant vertical compression in the transformed areas, confirming that the pore

collapse occurs not only in the (x,y) plane of the microstructure but also significantly perturbs the porous structure in z direction.

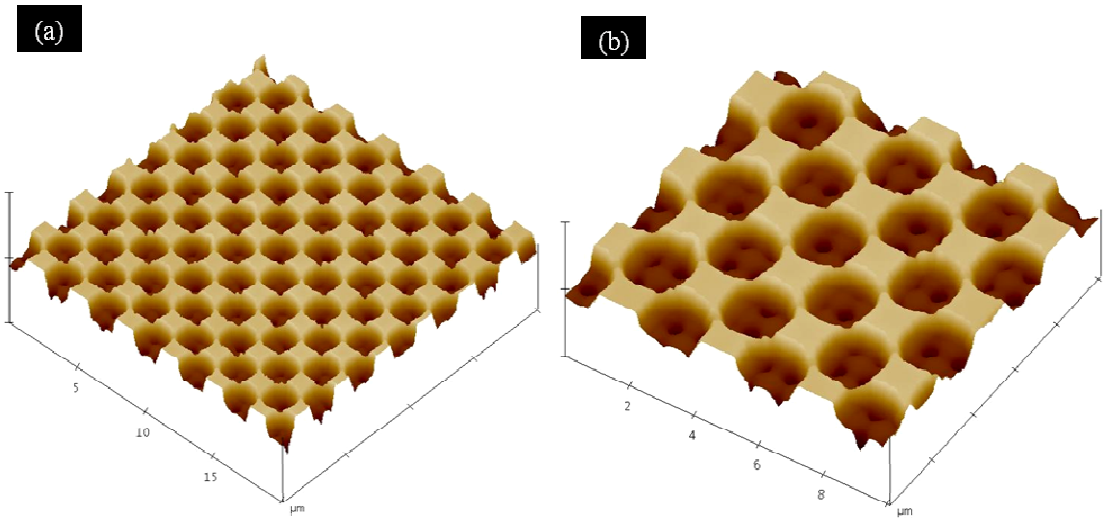

Figure 6.17: AFM image of the (a) Uniform square pattern of polystyrene on SU8 structure (20x20 µm, Z range of 2.2 µm). (b) Higher magnification image clearly depicting the PS pattern and the underneath porous structure and one to three open pores exposed in each open square (10x10 µm, Z range of 2.0 µm*).*

While the polystyrene parallel stripes pattern confines the mechanical instabilities to one dimension, the more complex pattern comprising of array of polystyrene squares confines the mechanical instabilities in two dimensions (Figure 6.17a). The square pattern imposed here has a periodicity of 3 µm with the dimensions of the individual squares being 1.5µm × 1.5µm separated by square areas of the same size. The pattern was stamped on the porous lattice of the SU8 such that the (10) direction of the polystyrene pattern is at ~ 45° with respect to the (10) direction of the SU8 square lattice. Such a pattern orientation mismatch results in a complex periodic of *superlattice transformed structure* governed by the periodicity of the individual patterns (porous structure itself and polystyrene micropattern) and their relative alignment in (x,y) plane.

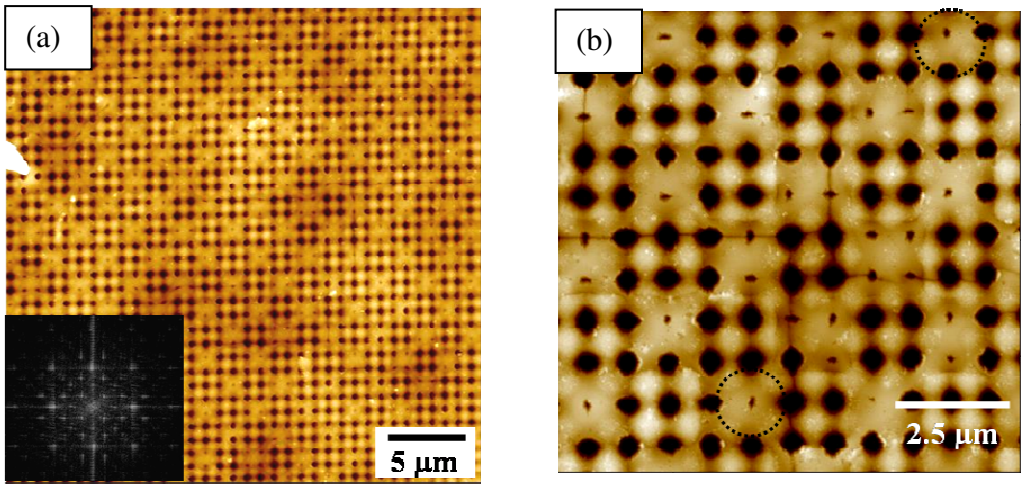

Figure 6.18: Pattern transformation in the microframe owing to the two dimensional confinement caused by the square patterns of SU8 and polystyrene aligned at 45° with respect to each other (inset shows the FFT depicting overlapped misaligned lattices). (a, b) higher magnification of the confined transformation identifying the repeating structure in adjacent cells.

Apart from the 2D periodicity, the other significant difference of the square array polystyrene pattern compared to the 10 µm periodic stripe pattern described earlier is the smaller periodicity (3 µm). The smaller periodicity results in only one or two open pores followed one or two closed pores in (10) and (01) directions as opposed to nearly five open pores in (10) direction and infinite pores in (01) direction (Figure 6.17 b). AFM image of Figure 6.18a depicts the square array of the transformed pattern and the FFT depicts the overlapping square pattern of the transformed and original lattices oriented 45° with respect to each other. The AFM image in Figure 6.18b identifies (highlighted by circles) two identical squares in adjacent unit cells. It is apparent that the transformation occurs only partially (in terms of ellipticity of the pores and their orientation), with the pore shape in-between the circular pores and mutually orthogonal ellipses (Figure 6.18b). This partial transformation suggests a finite and very sharp transition region between the pristine and transformed regions which spans over usually two neighboring pores.

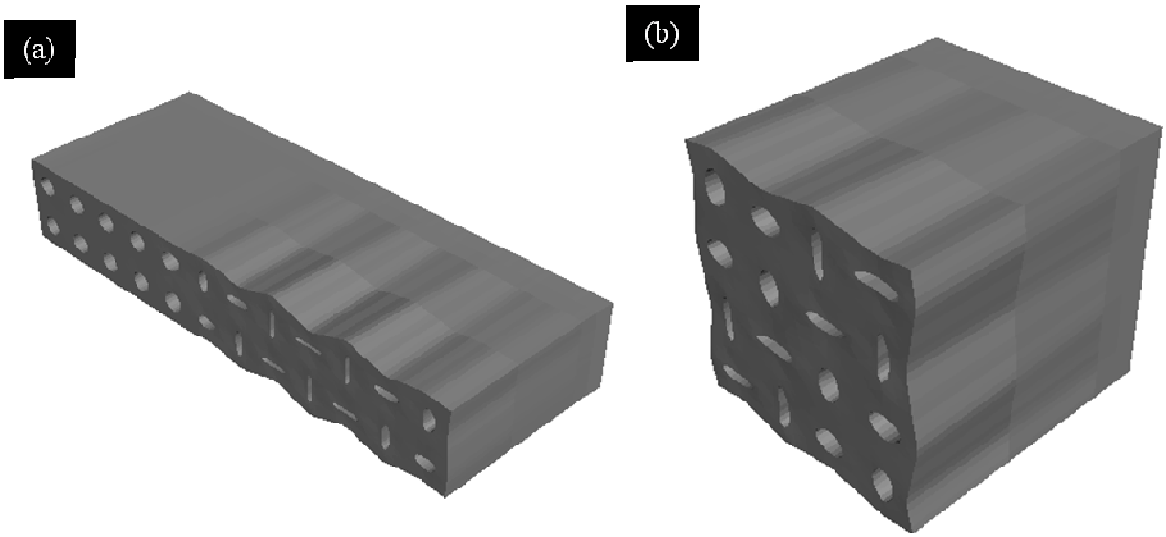

Figure 6.19: Eigenmode of the microscopic instability for the confined square array of circular holes as predicted by the Bloch wave analysis for: (a) one dimensional stripe confinement (2x6 cells) and (b) two dimensional squared confinement (2x2 cells).

Numerical simulations were conducted of both the pattern obtained with polystyrene parallel stripes and square micropatterned arrays to understand the extent of the stresses and corresponding deformation areas. The results of these simulations shown in Figure 6.19 confirm again, that the deformation of porous structures within SU8 material is highly localized and does not extend to more than two or three neighboring cells (Figure 6.19a). The width of the transition region is close to the experimentally observed gradient of localized transformation of porous structure. The numerical investigations also confirm the experimentally observed intermediate geometry of the deformed pores in the transition regions between the pattern and pristine structures with partially collapsed and intermediately reoriented pores (Figure 6.19a).

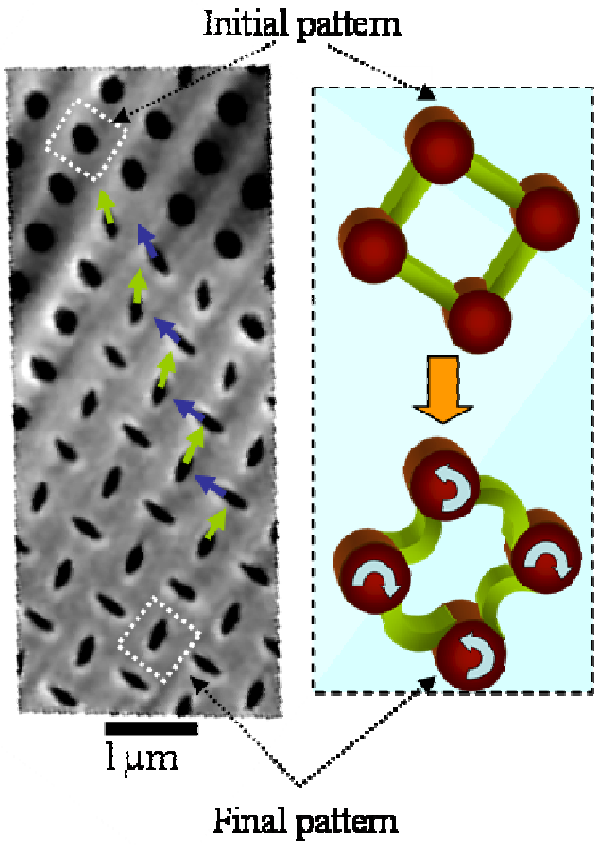

Figure 6.20: SEM image of the square lattice showing the gradual transformation from a pristine square unit cell of cylindrical pores to the final transformed pattern and schematic representation of the transformation highlighting the deformation of the individual elements of the microframe structure.

Indeed, the gradient transformation of porous structures is obvious at the interfacial regions between a pristine and transformed pattern such as that presented in Figure 6.20 for gradual variation of the degree of pore filling. The transformed pattern extends from a few pores at the top remaining unfilled and so preserving their initial morphology. In this image, one can observe a progressive transformation from a square array of circular holes on the top (initial morphology) to the final transformed pattern of orthogonal collapsed ellipses on the bottom of the region. The gradual alternation of the local orientation of the ellipsoidal pores confirms the presence of

the strong rotational deformation of nodes. Finally, orthogonal orientation is established within few unit cells as highlighted by the arrows in Figure 6.20.

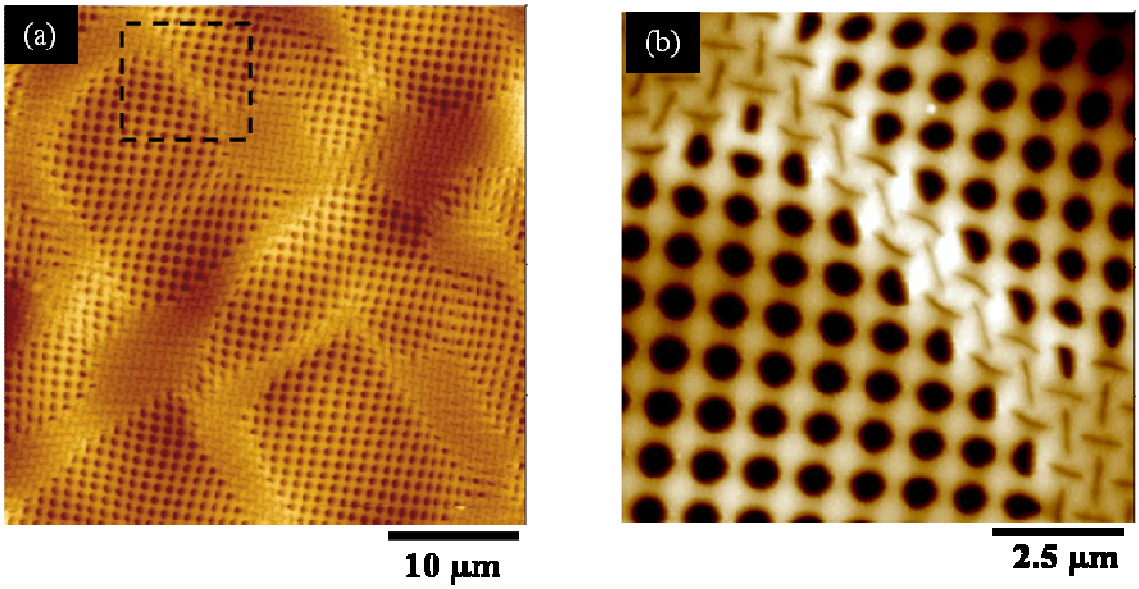

Figure 6.21: AFM image of mechanical instabilities in a microframe with a variety of topographical features resulting localized transformation of the pattern (a) AFM image depicting the transformed pattern localized to certain areas, connected by narrow ridges (b) Higher magnification image of a single ridge showing the large curvature the struts undergo when the transformed pattern is localized to two adjacent unit cells.

While only a partial transformation occurs when the polymerization is confined to few pores in (01) and (10) direction, highly localized (confined to just two pores wide) instabilities occur when the polymerization is confined in only one direction. Figure 6.21 depicts the *in situ* polymerization conducted in a porous structure with a broad range of topographical features which include squares extending over a few pores and narrow ridges. These topographical features are caused by non-uniform distribution of the acrylic acid monomer in various areas resulting in selective infiltration of the pores in certain areas while the other areas remained pristine. Polymerization and subsequent solvent evaporation resulted in highly confined mechanical instabilities in the localized areas where the infiltration of the monomer occurred.

Figure 6.21a depicts the AFM image with transformed localized areas interconnected by transformed narrow stripes. Figure 6.21b shows the narrow transformed pattern (two unit cell wide) along the (11) direction. The transformed pattern exhibits highly deformed concave pores owing to the high degree of localization of the pattern transformation. Furthermore, the pores adjacent to the transformed areas on either sides exhibit large deformation to accommodate the bending of the struts in the transformed regions. The transformation observed here suggests that a complete and highly localized transformation can be achieved when the compressive stresses are confined to one dimension as opposed to the partial transformation in the case of the confinement in two dimensions. The high degree of bending of the struts to accommodate narrow transformed regions shows the excellent mechanical properties and elasto-plastic nature of the SU8 struts.

6.3.4 Replication of transformed pattern

To extend the range of application of pattern transformation harnessed by mechanical instabilities in periodic porous structures, it is highly desirable to extend the range of materials where such transformed periodic structures can be achieved or stored. As a first step towards this goal, we conducted additional studies and confirmed that the topographical features of the transformed pattern can be replicated in a common glassy polymer, polystyrene, by using CTL process as depicted in Figure 6.22a. [274]

The process involves in the fabrication of a negative replica (stamp) of the transformed pattern from SU8 structures by using PDMS. The stamp is then used again to replicate the transformed pattern in polystyrene (Figure 6.22a). The AFM image in Figure 6.22b shows the resulting

polystyrene replica with mutually orthogonal ellipses resembling those in the transformed

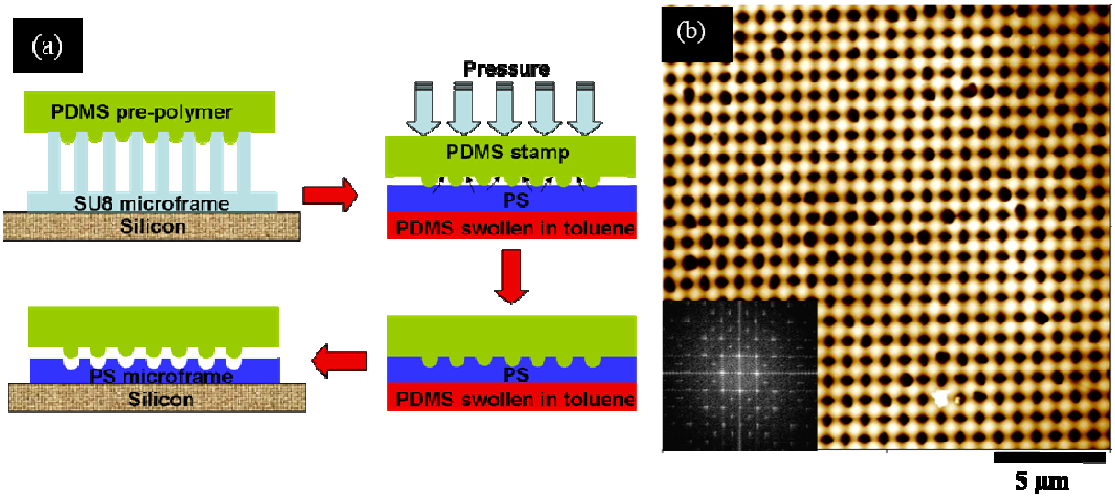

Figure 6.22: (a) Schematic illustrating the CTL replication of the transformed pattern and (b) AFM topographical image of replicated polystyrene structure with mutually orthogonal ellipses (inset shows the corresponding FFT) .

master, although the level of collapse is less dramatic than in the original microstructure. Based upon this preliminary data, we suggest that this replication technique can be extended to generate more complex polymeric patterns using various patterned instabilities as masters. Furthermore, the stamped patterns can be employed as physical masks for patterning various nanostructured materials for tuning the optical properties of the assembled superlattices.

In conclusion we have demonstrated the onset of buckling instabilities in porous elasto-plastic solids upon polymerization of additional rubbery component inside cylindrical pores which lead to a dramatic pattern transformation. Owing to the elasto-plastic nature of the porous structure, the transformed pattern is frozen and stable as opposed to the elastomeric counterparts, which return to the pristine structure once the external pattern is removed.

We suggest that localized polymerization of acrylic acid within cylindrical pores resulted in confined mechanical instabilities leading to a complex hierarchical porous structure comprised of regularly collapsed pores with alternating orientation. Moreover, we have observed a controlled transformation when the polymerization can be confined in two dimensions to highly localized areas which include only two to three neighboring pores. On the other hand, complete transformation with highly collapsed pores can be achieved when the transformation is confined in only one dimension. Finally, we have also demonstrated the replication of the topographical features of the transformed pattern in other polymers using the CTL process.

We believe that the mechanism of transformation of organized microporous solids via localized bifurcation of the primitive cell with rotation of nodes combined with the bending or buckling of struts can be important in the range of complex physical phenomena critical for diverse fields such as tunable photonic crystals, porous scaffolds for tissue engineering, structures with tunable transport properties, or porous-shape memory alloys in metallic and polymeric stents.

CHAPTER 7

HIGHLY CROSSLINKED POLYMER-SILICON FLEXIBLE STRUCTURES FOR FAST CHEMICAL VAPOR DETECTION

7.1 Introduction

Although there are several aspects contributing to an efficient chemical sensor system, responsive materials are important in optimizing several key attributes critical for their ultimate performance, specifically high sensitivity, selectivity, fast response time, and wide dynamic range. Common issues with sensors reported to date are limited range of detection, slow response, long recovery period, and fast saturation (limited dynamic range).[276] Most of these issues are directly associated with the large volume of bulk porous materials that are needed for measurable signal output, which leads to inherently slow sorption, diffusion, and desorption processes. One type of gas sensor that receives modest attention, yet is among the most frequently used for measuring important environmental quantities is a humidity sensor.[277] Important applications include respiratory equipment, incubators, chemical gas purification, and surgical operations. The major requirements for humidity sensors are good sensitivity over a wide humidity range, low hysteresis, good reproducibility, and longevity.[277,278] Often it is required that the sensors are miniature and amenable for integration into arrayed systems to work as odor sensing arrays.

Current humidity sensors predominantly exploit bulk materials with resistive and capacitive response properties. These sensors are comprised of a moisture sensitive ceramic, metal, or polymer material undergoing a change in resistance/capacitance upon variations in ambient humidity.[278,279] Some of the common polymers considered in water vapor sensing technology are polyimides, polycarbonates, cellulose acetates, and conductive polymers.[280,281] Typical vapor

sensitivity of these sensors is tens parts per million (10 ppm) (or ±0.05% RH), which is sufficient for most routine measurements, but fails if a fast, real-time monitoring of vapor content variation is required. Using a porous material to maximize the specific surface area available for water vapor adsorption resulted in increased sensitivity to a low ppm level.[282,283,284] For example, 0.4 ppm_v water vapor detection was demonstrated by Salonen et al using carbonized porous silicon.[284] Bruno et al. used a polymer coated resonant device to obtain a sensitivity of 7 ppm_v.[285] Although the sensors reported showed good sensitivity they suffered sluggish (few minutes) response and usually required few minutes to completely recover. For current designs, modest sensitivity and slow response are major obstacles in the development of the microcantilever-based sensor technology.[286,287]

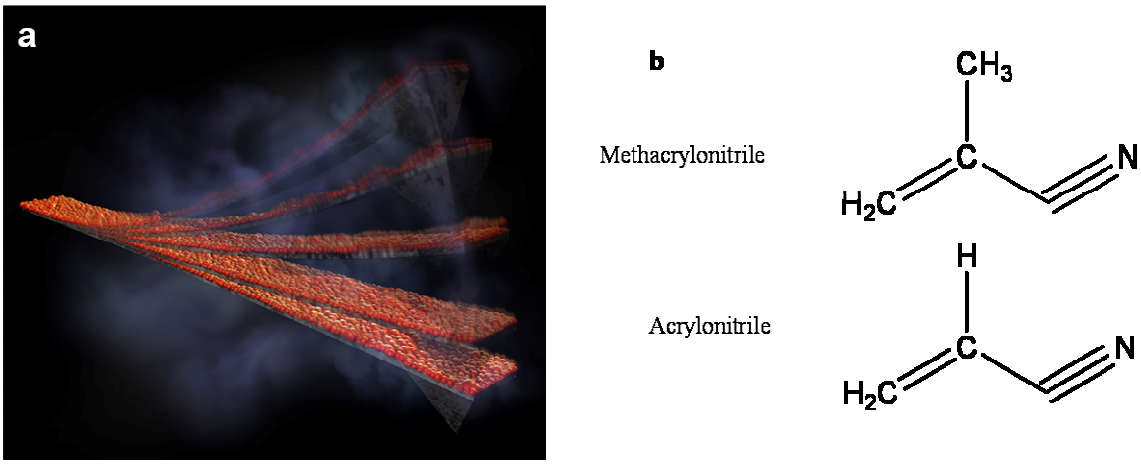

Figure 7.1: (a) Schematic of the plasma polymer coated microcantilever responding to water vapor. (b) Chemical structure of methacrylonitrile and acrylonitrile.

In this chapter, we present a bimaterial design for humidity sensing with a vapor-sensitive plasma polymerized nanolayer coated on a silicon microcantilever with a low flexural rigidity (Figure 7.1a). This layer acts as a sensitive mechanical actuator, which mediates high internal stresses enabling fast response to presence of vapor in the environment. For a bimaterial microcantilever, preferential swelling plasma-polymerized material with particular analytes causes a change of surface stress resulting in the bending proportional to the external stimulus. For this bimaterial

design, we observed unprecedented sensitivity to humidity variations with resolution ± 10 ppb (±0.00005% RH) with fast (millisecond range) temporal response, which are both several orders of magnitude better than the typical values reported in the literature. We suggest that the integration of the crosslinked polymer, high internal stresses, and firm adherence to the silicon are critical for the responsive behavior of a bimorph structure.

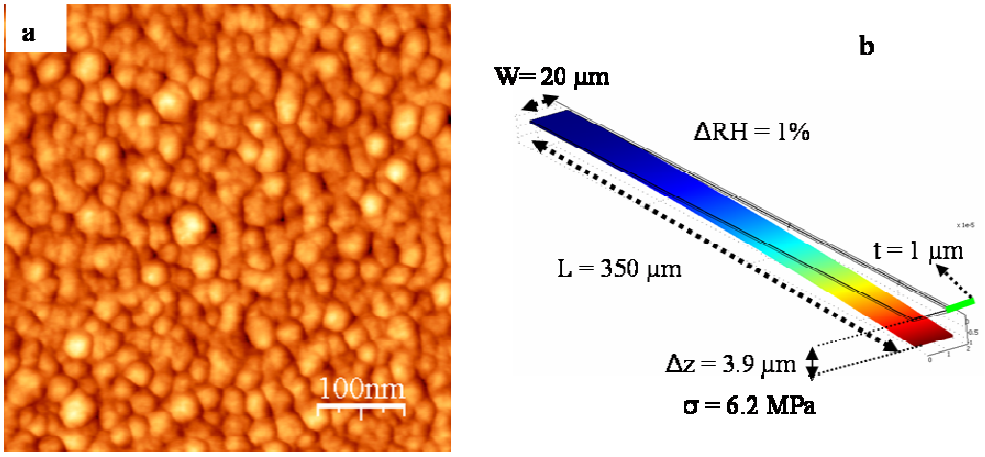

Figure 7.2: (a) AFM topographical images of PP-MAN surface showing the nanodomain surface morphology (z range: 10 nm) (b) FEA model of the deflected cantilever with parameters exploited.

7.2 Morphology and properties

Plasma enhanced chemical vapor deposition exploited here offers the unique ability to polymerize a wide variety of precursors to obtain coatings sensitive to various analytes.[288,289,290,291,292] Plasma polymerized methacrylonitrile (PP-MAN) was observed to be the most efficient vapor responsive material from a series of six other plasma polymers tested in this study (Figure 7.1b). The AFM image of PP-MAN coating with a thickness of 283 nm at 6% RH shows a granular morphology with a surface microroughness of about 1.2 nm over an surface area of 1×1 μm^2 (Figure 7.2a). The granular surface morphology, a characteristic feature of the plasma polymers films [293], with average diameter of nanodomains below 30 nm facilitates a high specific surface area critical for

performance discussed here. In fact, it has been previously demonstrated that the enhanced surface area (due to well defined grain boundaries) and locked in residual stress in thin metal films deposited at slow rates provide significant enhancement in the sensitivity of the MC based sensors compared to the smooth films.[294] Surface force measurements [295] showed the elastic modulus of 1.6 GPa and high adhesive forces (36±12 nN). The contact angle of the PP-MAN of 75±4° (surface energy of 43 N/m), as opposed to the 56±2° of spin coated sample characterizes the surface as modestly hydrophobic, possessing some polar groups.[296] Considering the higher contact angle of PP-MAN and the presence of C=N and C≡N stretch bands in the Fourier transform infrared (FTIR) spectra, we conclude that plasma polymerization results in crosslinked films with a modest surface concentration of the polar cyano groups. Surface analysis of the plasma polymers acquired by X-ray photoelectron spectroscopy (XPS) indicated close to expected chemical composition with, however, the presence of some amount (12-14%) of oxygen possibly due to the free radicals within the sub-surface layer.[297]

7.3. Response of plasma polymers coatings to water vapor:

Figure 7.3a shows the microcantilever at various RHs ranging from 6% to 66%. The deflection of the PP-MAN cantilever under desiccation and humidification shows a modest <2% hysteresis over 10 consecutive cycles (10 hours time frame) separated by several days and over a year of storage (Figure 7.3b). It is remarkable that the response remained virtually unchanged (within ±5%) after such long storage time under normal (variable temperature, humidity, and air quality) lab conditions. The deflection was virtually linear for small RH range (<10%) and sensitivity (deflection per a unit of humidity change) was calculated to be extremely high, 3.5 μm/1% (Table 7.1). It is worth to note that the simple presence of the human palm at a modest distance (about a foot) can be easily visualized with a 50 μm deflection. The response of identical cantilevers coated with spin coated “conventional” PMAN (of thickness 470 nm) was remarkably lower. This cantilever showed

a meager response with a sensitivity of only 110 nm/1%RH, similar to that reported in the literature for similar cantilever and nearly *30 times lower* than corresponding plasma polymerized cantilever.[298] Plasma polymerized acrylonitrile (PP-AN) cantilever also exhibited a high (although lower than pp-MAN) sensitivity while the uncoated reference cantilever exhibited no visible deflections (Figure 7.3b).

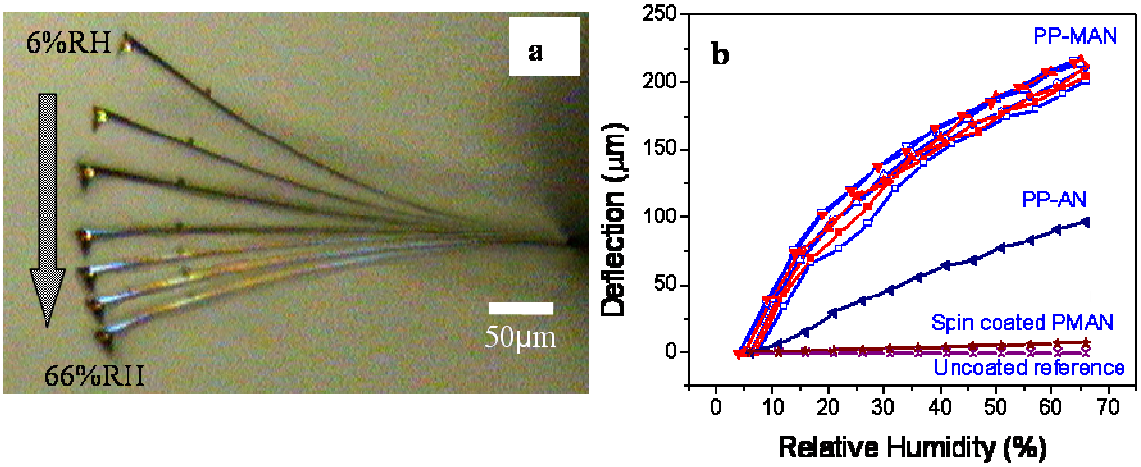

Figure 7.3: (a) Optical images showing the bending of the PP-MAN-coated cantilever for humidity changing from 6% to 66% RH at an interval of 10% RH with deflection at 6% taken a reference point. (b) The deflection vs. humidity (error bars are below the size of the symbols) of cantilevers coated with PP-MAN, PP-AN, spin-coated PMAN (5 consecutive cycles) and a bare silicon cantilever.

Here, in accordance with common understanding, we suggest that the adsorption (condensation) of water molecules on and rapid progressive swelling of the plasma polymer layer are the primary reasons for the differential stress across the bimorph interface causing the bending of the entire structure. However, water condensation, which applies normal forces due to the vertical component of the surface energy of the liquid-vapor interface normally results in a minor nanometer-scale deflection, well below any deflections observed here.[299,300,301] Thus, although it is possible that some enhancement might come from the capillary condensation in the nanopores, micron-scale deflection requires to consider swelling as a major cause. Hence, swelling of the PP-

MAN layer was studied by measuring the coating thicknesses at three different RH levels (6%, 30% and 66%). The thickness of the film increased by 12% for a 60% RH difference giving 0.2% change per 1% RH. Thus, the strain induced in the polymer film for a 1% change in RH was calculated to be 4.3×10^{-4}. This level of strain generates a 5 MPa stress for the measured elastic modulus. The corresponding deflection can be roughly estimated using the known Stoney's equation,[302,303] $\sigma = \frac{Et_s^2}{6R(1-\upsilon)t_f}$, where R is a radius of curvature, E is the elastic modulus, t_s is the thickness of the substrate, υ is the Poisson's ratio, and t_f is the thickness of the polymer film. The expected deflection calculated from this equation for the swelling-induced stress was about 2 μm/1%RH which is lower to that obtained experimentally. Therefore, considering the limited accuracy of the Stoney's equation for bimaterial structures with the thicker coating (25% of the thickness of the cantilever in our case), we evaluated stresses for the polymer-silicon beam with finite element analysis (FEA) (Figure 7.4a).[304] The estimated deflection due to the swelling-induced stresses with full stress transfer across interface was estimated to be 3.9 μm/1%RH, which is close to that obtained experimentally (3.5 μm/1%RH) with some reduction caused probably by coating imperfection (Figure 7.4a). The interfacial stress at the free end of the bimaterial structure was calculated to be 6.2 MPa (12% higher than in simple Stoney's estimation) for 1% change in RH and reaches nearly 370 MPa for a 60% change in RH. The lower sensitivity of a 50 nm thick PP-MAN coating also agrees closely with FEA evaluation (Figure 7.4a). Thus, FEA simulation indicates that the swelling-related interfacial stresses are sufficient to cause the microcantilever bending behavior observed experimentally.

In the case of spin coated PMAN layers, the observed cantilever deflection was well below the theoretical estimation confirming a failure to efficiently transfer the swelling-initiated stress. This result points to the importance of the strong adhesion of the coating resulting in a maximal conversion of the enthalpy driven swelling to the mechanical bending of the bimaterial cantilever.

Indeed, plasma polymerized coatings introduced here displayed excellent adherence to the cantilever surface as confirmed by the study of modified cantilevers after huge multiple deflections (up to 300 μm) and a peel-off test. AFM imaging of the PP-MAN coating after multiple deflections showed no signs of rupture or delamination of the topmost plasma polymerized layer. This is consistent with recent results on the much higher mechanical stability of the plasma polymer coatings under repeated shearing.[305] Moreover, our peel-off test demonstrated that the PP-MAN

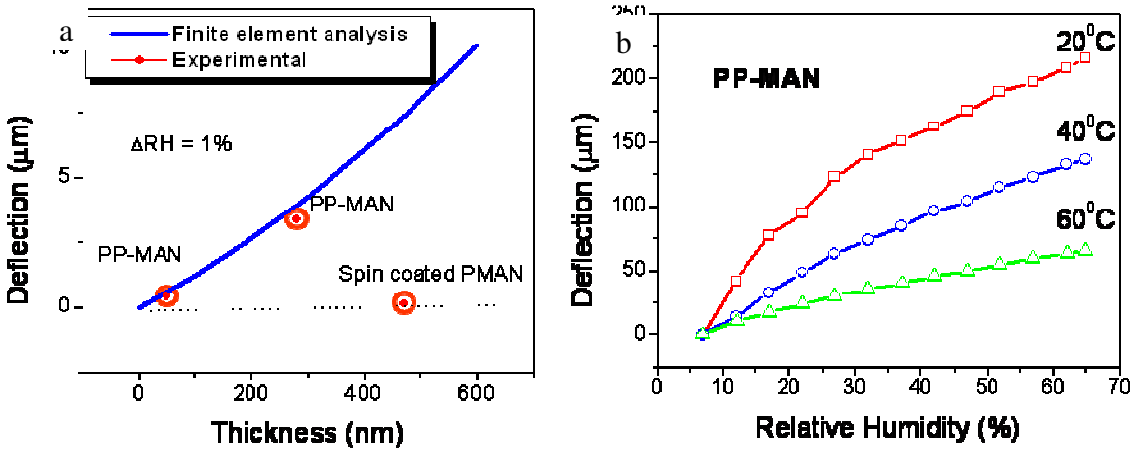

Figure 7.4: (a) FEA theoretical deflection of the cantilever vs thickness of the PMAN coatings for 1% change in RH (solid line) and experimentally observed deflections for 50 nm and 283 nm PP-MAN and 470 nm spin coated PMAN. Dotted line represents typical deflection for conventional cantilevers. (b) Deflection vs humidity of PP-MAN cantilever at 20ºC, 40ºC, and 60ºC.

coatings are extremely stable and cannot be removed with a sticky tape.

Conventional bimaterial cantilevers are usually based on one-side modification with SAMs that facilitate the adsorption of the analytes leading to the differential surface energy.[306,307,308,309] Although such a design has been successfully used for chemical and biological detection their sensitivity is inherently limited to the differential surface energy mediated by analyte adsorption.[310,311,312,313,314] If this difference reaches 20 mJ/m^2 (difference between highly hydrophobic and hydrophilic surfaces), the bending force reaches several nanoNewtons that could lead to several hundred nanometers deflection for typical microcantilevers (stresses within 0.01-0.1

N/m). In contrast, in the case of plasma polymer nanocoatings even modest swelling results in the bending force in milliNewton range (stress within 1 -10 N/m) facilitating micron-scale deflections.

Hence, unlike conventional bimaterial structures, which rely on small differences in the surface tension for active and passive sides, the bimaterial design with plasma polymerized coating utilizes a mechanism involving *large interfacial stresses* causing inherently higher bending forces. It is worth to note that swelling has been previously employed as the mechanism to induce differential stress in the bimaterial cantilever for vapor sensing.[315] However, these coatings as well as other (such as spin coating, and inkjet printing) coatings resulted in relatively modest deflections, typically on the order of several tens-hundred nanometers.[316,317] The reported sensitivity of 10 nm/1%RH for plasma polymerized cantilevers is more than two orders of magnitude lower than that measured here, indicating an insufficient transfer of swelling-induced stress to the polymer-inorganic interface.

The sensitivity achieved here are several orders of magnitude better than those known for microcantilever-based sensors and considered to be sensitive, miniature, fast, and inexpensive alternative. [318,319,320,321] Surface layers, such as self-assembled monolayers (SAMs), polymer brushes, hydrogels, thin metal films, and sol-gel layers have been employed as sensitive coatings.[322,323,324,325] Swelling of plasma polymerized allylamine on cantilevers has been recently studied by Igarashi et al.[316] They have concluded that lower cross-linking of plasma polymers results in higher swelling, but these bimaterial structures showed only modest cantilever deflection due, probably, to insufficient stress transfer ability. We suggest that the fine balance of local hydrophobic and hydrophilic interactions important for fast intake and removal of water molecules achieved for PP-MAN coatings with randomized network of polar segments and hydrophobic methyl groups is responsible for such swelling behavior (Figure 7.1a). The coexistence and close proximity of hydrophobic and hydrophilic groups, as well as the internal stresses promote

significant expansion and contraction. This suggestion is supported by much less impressive performance of PP-AN coating without hydrophobic methyl group (Figure 7.3b) and some other polymers with predominantly polar or hydrophobic segments. Finally, the response of PP-MAN cantilever was tested at different temperatures demonstrating the highest response close to the room temperature (Figure 7.4b).

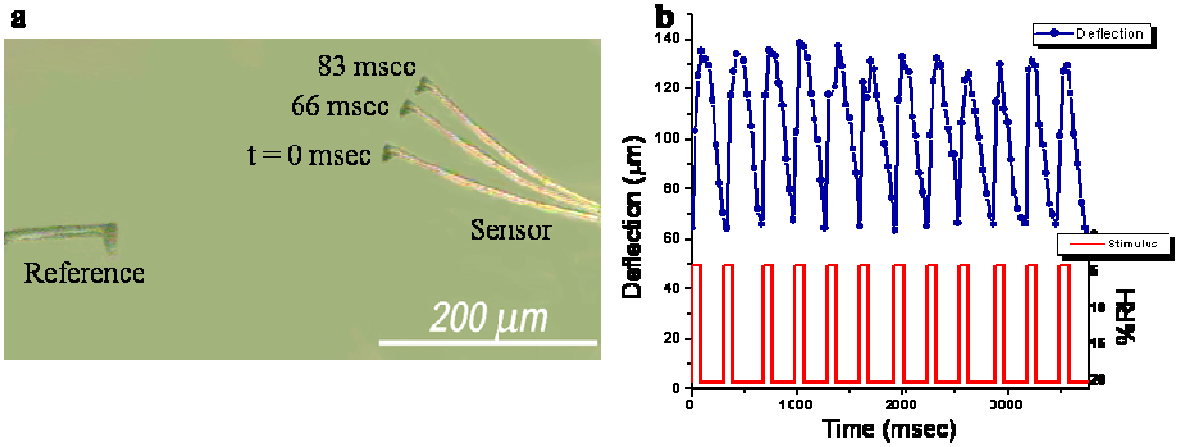

Figure 7.5: (a) Overlaid snap shots of the PP-MAN coated cantilever and reference uncoated cantilever depicting the response to nitrogen pulse (b) Deflection of the cantilever under desiccating nitrogen pulses followed by relaxation to humid state.

7.4. Fast sensor response

The other important issue related to the conventional sensors relying on the swelling phenomenon is relatively slow dynamics to reach the equilibrium state.[323] In contrast, our experiments clearly demonstrate the extraordinarily fast response for bimaterial cantilevers. This fast response, which reaches a low millisecond range is out of reach for conventional sensors with typical response time in second-minute range because they are limited by

slow processes of molecular sorption and desorption within a bulk material.[326,327] In fact, considering that the analyte molecule propagation is controlled by the molecular diffusion [327], scaling down the thickness of the polymeric layer from conventional 10 µm to 200+ nm should facilitate three orders of magnitude faster equilibration time.

Two distinct experiments were performed to quantify the response time of the sensor to varying humidity in larger (%RH=16% and 2%) and smaller (%RH = 0.025% and 0.002%) ranges. Firstly, the PP-MAN cantilever was exposed to gentle dry nitrogen pulses (for 83 msec) followed by recovery (for 250 msec) to initial humidity (36% RH) at a constant rate of 3 Hz (Figure 7.5a, b). The corresponding periodic deflection of the PP-MAN cantilever and a reference uncoated cantilever were recorded for hundreds of cycles (see Figure 7.5a) and the differential deflection is plotted in Figure 7.5b (the correction for the reference cantilever deflection was within 3%). The responsive behavior was stable and reproducible with a characteristic asymmetric shape reflecting faster response and slower relaxation to the initial position. The response time was found to be 80±20 msec for 16% change in humidity (estimated from calibrated bending), a fast response to such a large range. In an independent experiment, the cantilever was exposed to cyclic variations of humidity in a narrow range (±1% RH) over a relatively long time (several minutes) and showed repeatable and stable response with no change in the base line (Figure 7.6a).

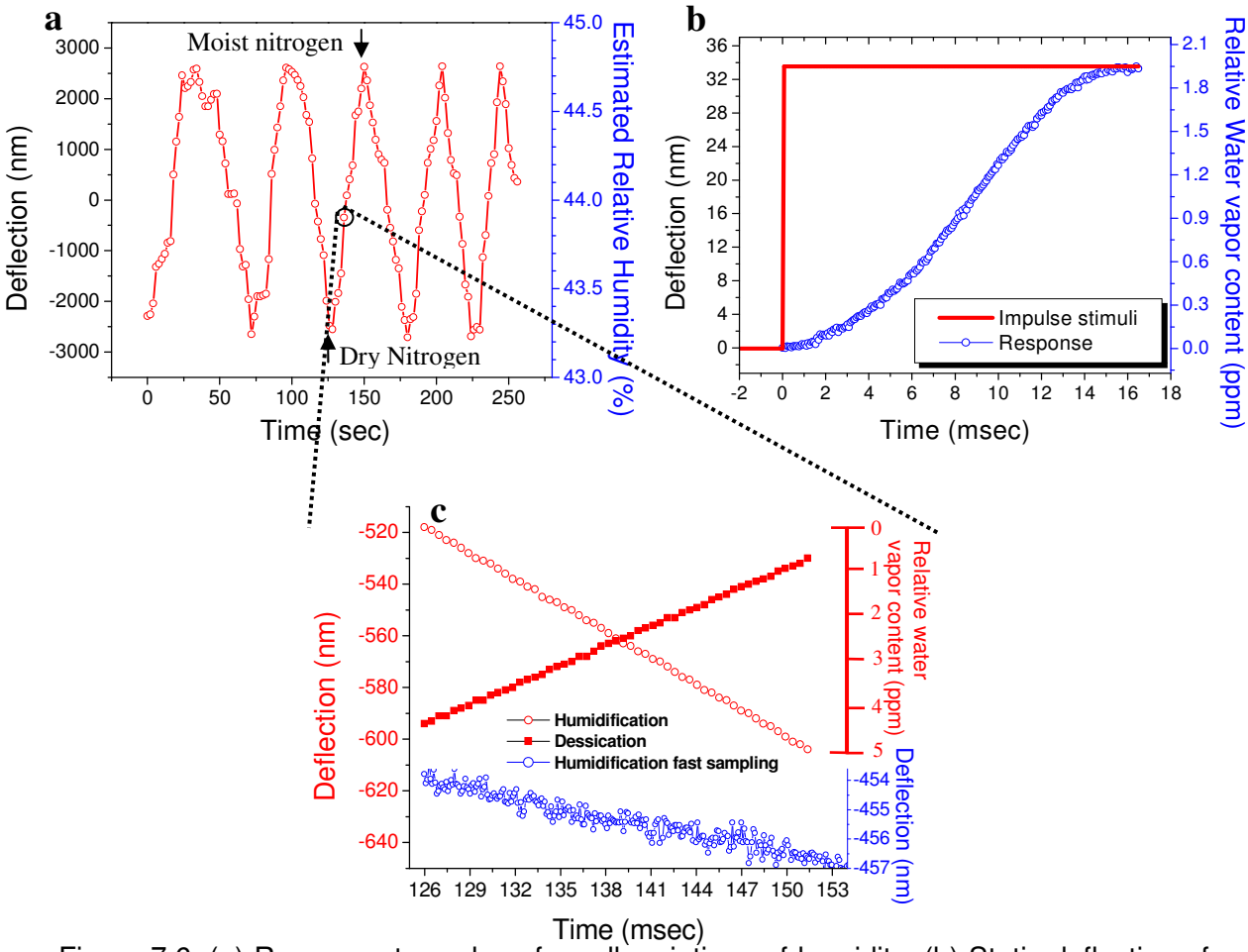

Figure 7.6: (a) Response to cycles of small variations of humidity. (b) Static deflection of cantilever to a sudden change in humidity (0.01% step). (c) Dynamic sampling for a linear humidification and desiccation for RH interval of 0.02% (top) and 0.001% (bottom).

On the other hand, for a nearly instantaneous change of humidity (by 0.01%) the cantilever exhibited a response time (between 10 and 90% of the total response) of 9.5 msec (Figure 7.6b). Furthermore, linear ramps (1%RH/sec) of humidification and desiccation within 0.025% RH or ±5 ppm_v range (1% RH corresponds to a vapor density of 0.23 g/m^3 [278]) were monitored with a sampling frequency of 1 KHz (Figure 7.6c). Under these conditions, we observed a linear response with a minimum distinguishable increment, limited by thermal vibrations, of 0.0005%RH (or ±10 ppb), which exceeds that reported to date with cantilevers by two orders of magnitude (Table 7.1).[284] The ultimate limits of the sensitivity were tested for the cantilever at a slow ramp

rate of 0.02%/sec with a sampling frequency of 10 KHz (Figure 7.6c). At such extreme conditions, the overall linear trend is observed beyond the thermal noise (thermal amplitude of 0.25 nm). This observation confirms the smallest measurable change of water vapor content of ±10 ppb and temporal resolution below 2 msec. This deflection dynamics shows not just the excellent sensitivity of the bimaterial cantilever, but also extremely fast response time under variable environmental conditions. Remarkably, the response was stable for many repeated humidification and desiccation cycles over a period of more than a year after fabrication.

7.5 Selectivity to various vapors

While the results discussed so far emphasized the high sensitivity and fast response time of the PP-MAN cantilevers to water vapor, this design can be extended to different gas/chemical analytes potentially inspiring a whole new class of real-time, fast, and microscopic chemical sensing arrays

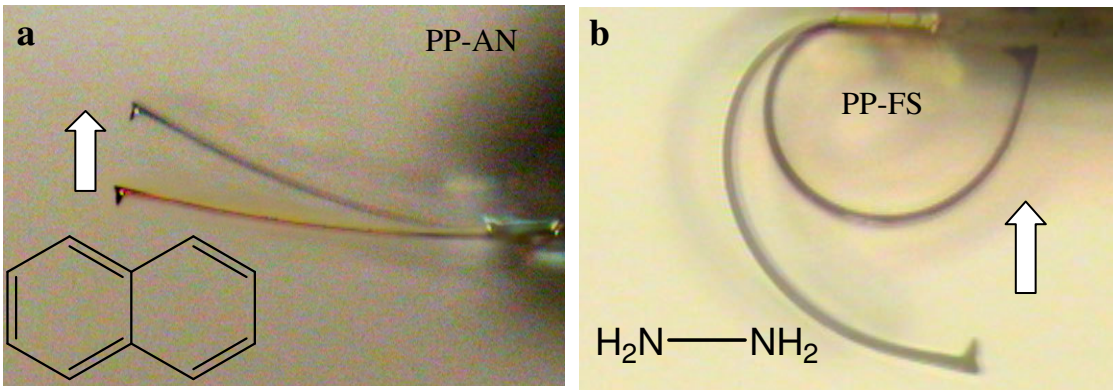

Figure 7.7. Optical images showing the deflection of the different cantilevers to different vapors: (a) PP-AN cantilever to naphthalene (b) PP-SF cantilever to hydrazine and PP-MAN cantilever to acetone

needed for real-time environmental monitoring. [306,328] In fact, in our preliminary testing, we demonstrated that a proper selection of plasma polymer coatings facilitates high sensitivity to organic compounds, which can be used as components of plastic explosives (Figure 7.7). For

instance, PP-AN (thickness 240 nm) cantilevers showed a fast reversible response to naphthalene vapor at 40℃ with a detection limit below 1 ppb, an exceptionally low value (Figure 7.7a).[329] Pentafluorostyrene (PP-FS) (thickness of 340 nm) cantilevers showed huge, reversible, and robust response (total 300μm bending) to saturated hydrazine, a potentially explosive and highly toxic chemical (Figure 7.7b).[329] In this case, the detection limit was estimated to be close to 10 ppb, which far exceeds those reported using resistance of conductive polymers or fluorescence emission of conjugated polymers (100 ppb - 10 ppm).[330,331,332] It is interesting to note that PP-FS coated cantilever initially bent by 180° still reacts to hydrazine vapor (Figure 7.7b). We believe

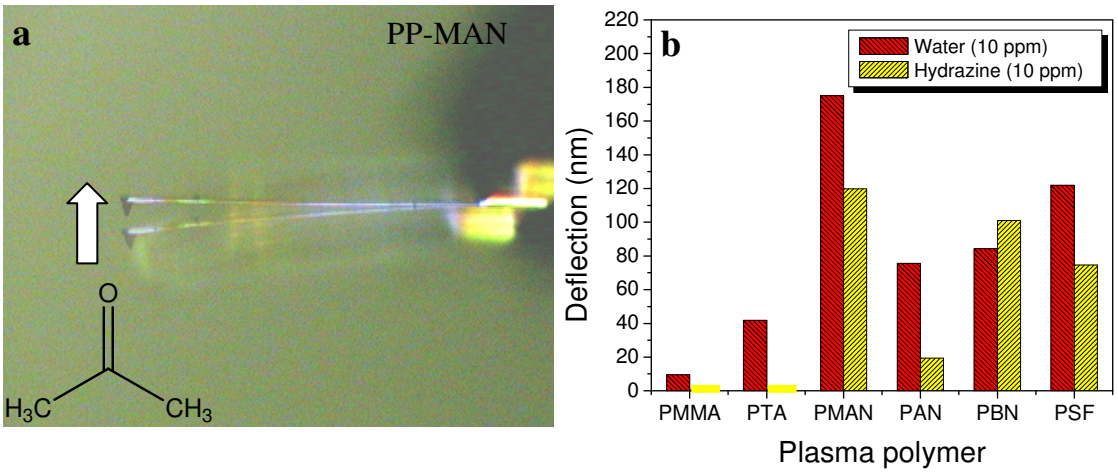

Figure 7.8. (a) Optical images showing the deflection of PP-MAN coated cantilever to acetone. (b) Response of different cantilevers to 10 ppm of water and hydrazine.

that different plasma polymer coatings investigated here exhibit structural changes due to solvation forces in the presence of various organic vapors. The magnitude of the swelling of the plasma polymers under various analytes will be the subject of further investigation.

To test the selectivity, which is critical for designing multifunctional sensor arrays, we monitored the response of a series of cantilevers coated with different plasma polymeric coatings to a host of analytes (Figure 7.8b). Cantilevers with plasma polymerized methyl methacrylate (PP-MMA), trimethyl silyl acetonitrile (PP-TA), PP-MAN, PP-AN, benzonitrile (PP-BN) and PP-FS (with thickness within 250-310 nm) showed very different responses to 10 ppm of water and hydrazine

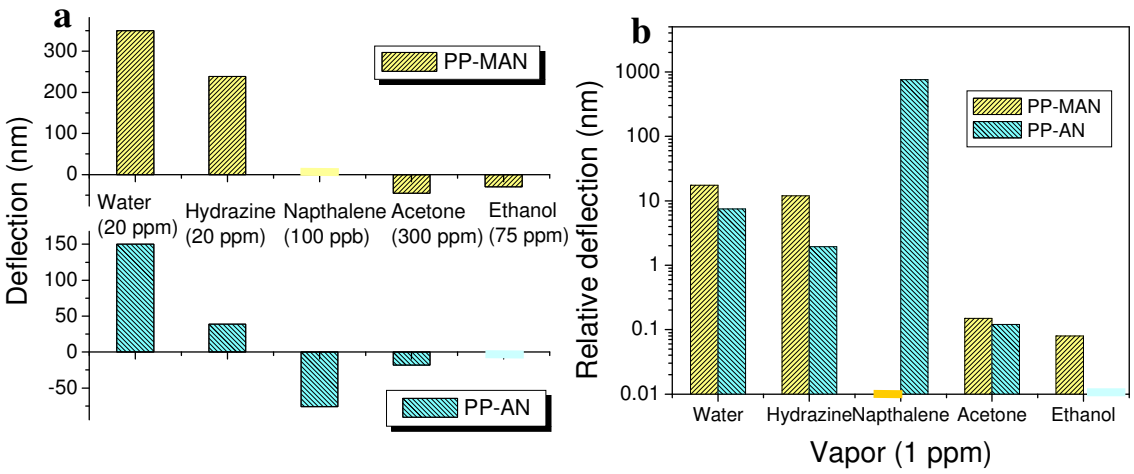

Figure 7.9:(a) The deflection of PP-MAN and PP-AN cantilevers to different vapors under saturated conditions. The bars have been included in the plot for clarity indicating no detectable deflection. (b) Logarithmic plot of the absolute deflection of PP-MAN and PP-AN cantilevers normalized to 1 ppm concentration of various analytes.

vapor (Figure 7.8b). The selectivity of some cantilevers to various analytes is illustrated by the response of PP-MAN and PP-AN cantilevers to water vapor (20 ppm), hydrazine (20 ppm), naphthalene (100 ppb), acetone (300 ppm) and ethanol (75 ppm) (Figure 7.9a). The selected series of chemicals represents a wide range of relevant types of gases representing several extreme cases as can be classified with existing schemes of solubility contributions [276]: highly volatile (acetone and ethanol), hydrophilic with rich hydrogen bonding network (water), highly hydrophobic (naphthalene) and highly reactive, polar (hydrazine) components of plastic explosives.

As we observed, for this series of chemicals, PP-MAN cantilever exhibits a response of 350 nm for water, while it remains insensitive to naphthalene and exhibits a *negative deflection* of 45 nm for acetone vapor, a puzzling behavior at this stage. It is interesting to note that the PP-MAN cantilever also deflects in opposite directions in response to ethanol, while the PP-AN cantilever exhibits a negative deflection for naphthalene for which PP-MAN remains insensitive. Figure 7.9b displays the absolute values of the cantilever deflections to various

vapors normalized to 1 ppm. The plot clearly shows that the response of cantilevers to different vapors spreads over *four orders of magnitude* making the pattern of deflection distinguishable using artificial neural network approach if cantilever arrays are exploited.[298]

Table 7.1. Summary of major parameters for various gas sensors

	Sensitivity to H_2O (nm/20 ppm)	Detection precision, * (ppb)	Response time (sec)	Selectivity Deflection Ratio **	Shelf Life (years) ***
PP-MAN cantilever	3500	±10	10^{-3} 10^{-1}	10^4	>1.5
Spin-coated PMAN cantilever	110	±300	NA	NA	NA
Typical bimaterial cantilever	10-100	±(100-500)	10-200	5-100	NA
Swollen PP coating from literature40	10	±10000	~100	NA	NA
Acoustic wave sensors 58	NA	±6000	~10	8	<0.1
Silicon Nanowires	NA	±50	>300	0.2	NA

Comparison with the best sensitivity and response parameters for existing designs from other plasma polymer cantilevers, acoustic wave sensors, and recently reported silicon nanowires shows that the detection precision of our design is about one order of magnitude better,

response time is at least two orders of magnitude faster, and selectivity is two orders of magnitude better than those reported in the refereed literature (Table 7.1). We believe there are several factors that contribute to the outstanding response of the plasma polymerized cantilevers, including the unique nanoporous morphology, minute thicknesses, cross-linked nature, and strong interfacial adherence of these nanocoatings. Sensitivity and response time achieved here is out of reach for the current sensor designs, which usually employ bulky porous materials or weak differential bending forces. It is worth to note that the plasma polymerization process employed here is a dry deposition technique, compatible with micromachining technology suitable for batch microelectromechanical system (MEMS) fabrication and allowing seamless integration into arrayed structures. Each cantilever may be selectively coated with a different sensing layer (current resolution of spot-coated plasma polymers is several hundred micrometers) with a distinctive response pattern to different chemical vapors making it feasible to develop sensitive, fast, and microscopic odor sensing structures capable of real time sensing of toxic and explosive chemical vapors.[276,333,334]

CHAPTER 8

GENERAL CONCLUSIONS AND BROADER IMPACT

8.1 General conclusions

Ultrathin and thin crosslinked films were found to exhibit robust physical transformations (non-linear and negative thermal expansion, buckling and folding) when subjected to external stimuli such as temperature and pH. The unique physical properties and the robust response of these ultrathin crosslinked polymers can be utilized to develop a functional microsensor system based on organized crosslinked polymers. In this work, we primarily focused on two major crosslinked polymer coatings: polymer microstructures fabricated by multi-laser interference lithography (IL), and plasma polymer coatings. The two polymer coatings with complementary attributes (such as periodic structure, vertical stratification, residual internal stresses, and high surface and interface tunability) will enable us to understand and design novel multifunctional coatings.

These large residual stresses in the plasma polymers result in intriguing thermal behavior such as non-linear thermal expansion and hysteresis between the heating and cooling cycles. Furthermore, a large, reversible negative thermal expansion of plasma polymerized polyacrylonitrile (ppPAN) and polytrimethyl silyl acetonitrile (ppPTSA) in the normal direction was observed. This unusual negative thermal expansion (NTE) behavior is suggested to be caused by vertical contraction caused by the high residual stress in the polymer film, which is common for plasma polymerized materials combined with developed grainy surface morphology.

In the next level of complexity, the crosslinked periodic porous structures were fabricated using multi-laser beam interference lithography, which formed glassy skeletons. Organized

bicomponent structures were fabricated by infiltration of the rubbery component into the porous glassy microframe. AFM imaging and nanomechanical measurements on the SU8-PB binary microcomposites confirmed the templated periodic distribution of the glassy and rubbery microphases. The unique feature of the organized glassy/rubbery structures is that the crack follows the selected lattice direction stretching the rubbery phase inside of cylindrical pores. Indeed, in the case of the randomly distributed rubbery microphases, there are multiple random pathways in which the crack can propagate through glassy phase dissipating the least amount of mechanical energy and causing the macroscopic failure of the random microstructure. In contrast, for the organized bi-component rubbery-glassy structures discussed here, the crack's pathway through the rubbery-filled pores is predetermined by the matrix symmetry (square lattice in this case), which could possibly maximize energy dissipation during crack propagation. Such organized glassy-rubbery microcomposites fabricated with IL can find novel high-demanding applications, which require precise control of the mechanical elastic and plastic behavior at micro and nanoscale.

In the process of fabrication of organized glassy/rubbery structures, yet another intriguing observation is the mechanical instabilities in the periodic porous crosslinked microstructures. The onset of buckling instabilities during the polymerization of additional rubbery component inside cylindrical pores leads to a dramatic pattern transformation. Owing to the elasto-plastic nature of the porous structure, the transformed pattern is frozen and stable as opposed to the elastomeric counterparts, which return to the pristine structure once the external pattern is removed. Furthermore, localized polymerization of acrylic acid within cylindrical pores resulted in confined mechanical instabilities leading to a complex hierarchical porous structure comprised of regularly collapsed pores with alternating orientation.

All the above results clearly indicate the crosslinked thin films and the periodic porous structures can exhibit robust physical transformations under external stimulus such as mechanical stress, change in environment (pH, temperature). The latent energy, stored as residual stress in the crosslinked polymer systems, manifests as robust physical transformations in these systems, which can be exploited for realizing ultrasensitive sensors. Plasma polymers were employed as sensitive layers in bimaterial microcantilevers sensors resulting in unprecedented sensitivity and response time. In the best example, plasma polymerized methacrylonitrile coated silicon cantilever exhibited a deflection of nearly 200 μm for a 60% change in relative humidity enabling a resolution of 0.00005% RH. There are several factors that contribute to the outstanding response of our cantilevers, including the unique nanoporous morphology, minute thicknesses, crosslinked nature, and the strong interfacial adhesion of these nanocoatings. The sensitivity and response times achieved here are out of reach for current sensor designs, which usually employ bulky porous materials or weak differential bending forces.

8.2 Significance and Broader impact

The role of ultrathin polymer layers and multicomponent polymer coatings as functional surfaces and interfaces in sensors, actuators, microelectromechanical systems (MEMS), microfluidics, and biomedical implants continues to be of critical importance, particularly highly responsive materials. The work presented here establishes novel design paradigm for multifunctional crosslinked polymer coatings with well defined physical and chemical attributes. For example, conventional approaches of depositing a sensitive layer on the microcantilever involved in techniques such as spin coating, drop casting and ink jet deposition. Apart from the poor control over the thickness, morphology of the coatings, these techniques also suffered low sensitivity owing to the poor interface between the components of the bimorph. The novel approach of plasma polymerization on the microcantilevers overcomes these issues taking the microcantilevers technology to the next level.

The sensitivity and response times achieved here are out of reach for current sensor designs, which usually employ bulky porous materials or weak differential bending forces. It is noteworthy that the plasma polymerization process employed here is a dry deposition technique, compatible with micromachine technology suitable for batch micro-electromechanical system (MEMS) fabrication and allowing seamless integration into arrayed structures. Each cantilever may be selectively coated with a different sensing layer, as the current resolution of spot-coated polymers is several hundred micrometers. Individual layers can have distinctive response patterns to different chemical vapors making it feasible to develop sensitive, fast, and microscopic odor-sensing structures that are capable of real-time sensing of toxic and explosive chemical vapors. The excellent sensitivity, selectivity, and fast response of the plasma polymers demonstrated here have almost universal applications in the field of sensors far beyond cantilever based transduction. For example, the plasma polymers can be used as responsive matrix with nanoscale fillers to realize ultrasensitive chemiresistors and chemFETs.

On the other hand, the traditional approaches of multicomponent polymer systems, namely, polymer blends and block copolymers suffer from limitations such as disordered structure or limitation on the size of individual domains. As demonstrated in this work, multi laser beam interference lithography enables the fabrication of well-ordered multicomponent polymer films to complement existing approaches based upon phase separation (polymer blends and block copolymers). The multicomponent coatings demonstrated here can serve as a unique tool for the fabrication of a new generation of multiphase coatings with well-ordered, periodic, interpenetrating network topology, with monodisperse feature sizes ranging from 100 nm to 1000 nm, and possessing a combination of properties unachievable in established coatings incorporating conventional designs.

We believe that the mechanism of transformation of organized microporous solids via localized bifurcation of the primitive cell with rotation of nodes combined with the bending or buckling of struts can be important in the range of complex physical phenomena critical for diverse fields such as tunable photonic crystals, porous scaffolds for tissue engineering, structures with tunable transport properties, or porous-shape memory alloys in metallic and polymeric stents.

Publications and Presentations

Refereed publications directly related to this dissertation

1) **S. Singamaneni**, K. Bertoldi, S. Chang, J. H. Jang, E. L. Thomas, M. Boyce, and V. V. Tsukruk, "Mechanical behavior of porous elasto-plastic solids under deformation" Adv. Func. Mater., Vol. 19, pp. 1426, 2009.
2) **S. Singamaneni**, K. Bertoldi, S. Chang, J. H. Jang, E. L. Thomas, M. Boyce, and V. V. Tsukruk, "Instabilities and pattern transformation in periodic, microporous, elasto-plastic solids" ACS. Appl. Mater. Interfaces Vol. 1, pp. 42, 2009 ***(Invited article in the inaugural issue)***
3) J.-H. He, **S. Singamaneni**, C. H. Ho, Y.-H. Lin, M. E. McConney, and V. V. Tsukruk, Thermal Sensor and Switch Based On Plasma Polymer/ZnO Suspended Nanobelt Bimorph Structure, Nanotechnology Vol. 20, pp. 065502, 2009.
4) **S. Singamaneni**, S. Chang, J-H. Jang, W. Davis, E. L. Thomas, V. V. Tsukruk, "Mechanical properties of 2D Polymer Microstructures via Interference Lithography" Phys. Chem. Chem. Phys., Vol. 10, pp. 4093, 2008. ***(Invited feature article, Inside front cover)***
5) **S. Singamaneni**, M. C. LeMieux, H. P. Lang, Ch. Gerber, Y. Lam, S. Zauscher, P. G. Datskos, N. V. Lavrik, H. Jiang, R. R. Naik, T. J. Bunning, V. V. Tsukruk. Bimaterial

microcantilevers as a hybrid sensing platform, Adv. Mater., Vol. 20, pp. 653, 2008. ***(Invited Review)***

6) **S. Singamaneni**, M. E. McConney, M.C. LeMieux, H. Jiang, J.O. Enlow, T. J. Bunning, R. R. Naik and V.V. Tsukruk, "Polymer-Silicon flexible structures for fast chemical vapor detection" Advanced Materials, Vol. 19, pp. 4248, 2007. ***(Inside Front Cover)***
7) **S. Singamaneni**, M.C. LeMieux, H. Jiang, T. J. Bunning, and V.V. Tsukruk, "Negative Thermal Expansion in Ultrathin Plasma Polymer Films" Chemistry of Materials, Vol. 19, pp. 129, 2007.

<u>Publications from related studies</u>

8) **S. Singamaneni**, M. K. Gupta, R. Yang, M. Tomczak, R.R. Naik, and V. V. Tsukruk, "Universal, nondestructive, and *in-situ* identification of crystal orientation of anisotropic ZnO nanostructures" Adv. Mater. (Under review)
9) Y. Hu, Y. Gao, **S. Singamaneni**, V. V. Tsukruk, and Z. L. Wang, "Converse piezoelectric effect induced transverse deflection of a free-standing ZnO microbelt" Nano Letters (Under review)
10) M. K. Gupta, **S. Singamaneni**, M. E. McConney, L. Drummy, R. R. Naik, and V. V. Tsukruk, "Patterned secondary structure in silk fibroin films" Adv. Mater. (Accepted)
11) S. Chang, **S. Singamaneni**, E. Kharlampieva, S. Chang, and V. V. Tsukruk, "Responsive Hybrid Nanotubes Composed of Block Copolymer and Gold Nanoparticles" Macromolecules (In press) ***(Cover story)***
12) E. Kharlampieva, J. M. Slocik, **S. Singamaneni**, N. Poulsen, N. Kroger, R. R. Naik, and V. V. Tsukruk, "Protein-enabled Synthesis of Monodisperse Titania Nanoparticles on and within Polyelectrolyte Matrices" Adv. Func. Mater., (In press)

13) S. Chang, H. Ko, **S. Singamaneni**, R. Gunawidjaja, and V.V. Tsukruk, "Nanoporous Substrate with Hybrid Mixed Nanoclusters for Enhanced Raman Scattering for Peroxide Compounds" Analytical Chemistry, (Accepted)

14) B. Weintraub, S. Chang, **S. Singamaneni**, W. H. Han, Y. J. Choi, J. Bae, M. Kirkham, V. V. Tsukruk, Y. Deng, Density-Controlled, Solution-Based Growth of ZnO Nanorod Arrays for Enhanced Field Emission, Nanotechnology Vol. 19, p. 435302, 2008

15) H. Ko, **S. Singamaneni**, and V. V. Tsukruk, "Nanostructured Surfaces and Assemblies as SERS Media" Small, Vol. 4, pp. 1576, 2008 ***(Invited review)***

16) **S. Singamaneni**, C. Jiang, E. Merrick, D. Kommireddy, and V. V. Tsukruk, "Robust Fluorescence of Multilayered LBL films", Journal of Macromolecular Science, Part B: Physics, Vol. 46, pp. 7, 2007.

17) R. Gunawidjaja, C. Jiang, S. Peleshanko, M. Ornatska, **S. Singamaneni** and V. V. Tsukruk, "Flexible and robust 2D array of silver nanowires by encapsulation into free standing layer-by-layer films", Advanced Functional Materials, Vol. 16, pp.2024, 2006.

18) C. Jiang, **S. Singamaneni**, E. Merrick, and V. V. Tsukruk "Complex buckling instability patterns of nanomembranes with encapsulated gold nanoparticle arrays" Nano Letters, Vol. 6, pp. 2254-2259, 2006.

19) C. Jiang, M. E. McConney, **S. Singamaneni**, E. Merrick, Y. Chen, J. Zhao, L. Zhang, and V. V. Tsukruk "Thermo-Optical Arrays of Flexible Nanoscale Nanomembranes Freely Suspended over Microfabricated Cavities as IR Microimagers" Chemistry of Materials, vol. 18, pp. 2632, 2006.

20) M. C. LeMieux, M. McConney, Y-H. Lin, **S. Singamaneni**, H. Jiang, T. J. Bunning, V. V. Tsukruk "Polymeric Nanolayers as Actuators for Ultra-Sensitive Thermal Bimorphs" Nano Letters, vol. 6, pp. 730, 2006. ***(Selected for news in MRS Bulletin: Polymer-Silicon Microcantilevers serve as ultrasensitive IR detectors, MRS Bull., 2006, 31, 438-439)***

21) Y-H. Lin, M. E. McConney, M. C. LeMieux, S. Peleshanko, C. Jiang, **S. Singamaneni**, and V. V Tsukruk "Trilayered ceramic-metal-polymer microcantilevers with dramatically enhanced thermal sensitivity" Advanced Materials, vol. 18, pp. 1157, 2006. ***(Inside Front Cover)***

Conference Presentations on Dissertation Topic

1) **S. Singamaneni,** K. Bertoldi, S. Chang, J. -H. Jang, E. L. Thomas, M. Boyce, V. V. Tsukruk "Mechanical Instabilities in Nanoporous Elasto-Plastic Solids fabricated by interference lithography" ACS Spring meeting, Salt Lake City, UT, 2009. (***Oral presentation***)
2) **S. Singamaneni**, S. Chang, J. -H. Jang, E. L. Thomas, and V. V. Tsukruk, "Mechanical properties of the polymer composites fabricated via interference lithography" ACS Spring meeting, Salt Lake City, UT, 2009. (Poster presentation)
3) **S. Singamaneni,** K. Bertoldi, S. Chang, J. -H. Jang, E. L. Thomas, M. Boyce, V. V. Tsukruk "MechanicalInstabilities in Nanoporous Elasto-Plastic Solids" APS March meeting, Pittsburgh, PA, 2009. (***Oral presentation***)
4) **S. Singamaneni**, M. Gupta, R. Yang, Z. L. Wang, and V. V. Tsukruk, "In situ non-destructive identification of crystal plane orientation of ZnO nanostructures", APS March meeting, Pittsburgh, PA, 2009. (Poster presentation)
5) **S. Singamaneni**, S. Chang, J. -H. Jang, E. L. Thomas, and V. V. Tsukruk, "Mechanical properties of the polymer composites fabricated via interference lithography" APS March meeting, Pittsburgh, PA, 2009,. (Poster presentation)
6) **S. Singamaneni** "Triggering and Confinement of Mechanical Instabilities in Nanocomposite films and Nanoporous Elasto-Plastic Solids" MRS Fall meeting, Boston, MA, 2008,. (***Gold Graduate Student Award, featured in MRS Bulletin***)

7) **S. Singamaneni,** K. Bertoldi, S. Chang, J. -H. Jang, E. L. Thomas, M. Boyce, V. V. Tsukruk**,** "Buckling instabilities in periodic porous elasto-plastic solids" MRS Fall meeting, Boston, MA, 2008. (***Oral presentation***)

8) **S. Singamaneni**, S. Chang, J. -H. Jang, E. L. Thomas, and V. V. Tsukruk, "Mechanical properties of the polymer composites fabricated via interference lithography" MRS Fall meeting, Boston, MA, 2008. (Poster presentation)

9) **S. Singamaneni**, M. Gupta, R. Yang, Z. L. Wang, and V. V. Tsukruk, "Confocal Raman spectroscopy of one dimensional ZnO nanostructures", MRS Fall meeting, Boston, MA, 2008. (Poster presentation)

10) **S.Singamaneni,** M. E. McConney, M. C. Lemieux, H. Jiang, T. J. Bunning, V. V. Tsukruk, "Intriguing Thermal properties and thermal actuation of plasma polymer films" NATAS, Atlanta, GA, 2008. *(**Oral presentation**)*

11) **S. Singamaneni**, M. C. LeMieux, M. McConney, Y. -H. Lin, H. Jiang, J. O. Enlow, T. J. Bunning, V. V. Tsukruk "Plasma polymer nanocoatings as responsive materials for ultrasensitive sensor platform" MRS Spring meeting, San Francisco, CA, 2007. ***(Best Poster Award)***

REFERENCES

[1] Bhushan, B., Ed. *Micro- and Nanosystems: Information Storage and Processing* Systems, **2002**.

[2] V.V. Tsukruk, K. Wahl, Eds. *Microstructure and Microtribology of Polymer Surfaces*, ACS Symposium Series, v. 741, **2000**.

[3] I. Luzinov, S. Minko, and V. V. Tsukruk, *Prog. Polym. Sci.* **2004**, 29, 635.

[4] L. H. Sperling, *Polymeric Multicomponent Materials*, John Wiley & Sons, Inc., New York, **1997**.

[5] R. Mason, C. A. Jalbert, P. A. V. O'Rourke Muisener, J.T. Koberstein, J. F. Elman, T. E. Long, and B. Z. Gunesin, *Adv. Colloid Interface Sci.* **2001**, 94, 1.

[6] V. V. Tsukruk, *Prog. Polym. Sci.*, **1997**, 22, 247.

[7] C. Jiang, V. V. Tsukruk, *Adv. Mater.* **2006,** 18, 829.

[8] E. S. Gil, S. M. Hudson, *Prog. Polym. Sci.* **2004**, 29, 1173.

[9] S. Minko, Ed. Responsive Polymer Materials, Blackwell Publishing, Ames, **2006**.

[10] R. Yerushalmi, A. Scherz, M. E. van der Boom, and H.-B. Kraatz*, J. Mater. Chem.* **2005**, 15, 4480.

[11] H. Biederman, *Plasma Polymer Films*; Imperial College Press: London, **2004**.

[12] P. Tamirisa, K. C. Liddell, P. D. Pedrow, M. A. Osman, *J. Appl. Polym. Sci.* **2004**, 93, 131.

[13] H. Yasuda, *Plasma polymerization*; Academic Press, INC.: London, **1985**.

[14] H. Jiang, *Chem. Mater.* **2003**, 15, 340.

[15] S.Minko,; Ed.; *Responsive Polymer Materials: Design and Applications*; Blackwell Publishing: Ames, IA, **2006**.

[16]Bhushan, B., Ed., *Tribology Issues and Opportunities in MEMS*; Kluwer Academic Publishers: Dordrecht, **1997**.

[17] R.C. Advincula, W. J. Brittain, K. C. Caster, J. Ruhe, *J. Polymer Brushes.*; Wiley: Weinheim, **2004**.

[18] V. V. Tsukruk, *Adv. Mater.* **2001**, 13, 95.

[19] V.V. Tsukruk, *Prog. Polym. Sci.* **1997**, 22, 247.

[20] I. Luzinov, S. Minko, V. V. Tsukruk, *Prog. Polym. Sci.* **2004**, 29, 635.

[21] M. C. LeMieux, S. Minko, D. Usov, M. Stamm, V. V. Tsukruk, *Langmuir* **2003**, 19, 6126.

[22] D. Julthongpiput, M. C. LeMieux, V. V. Tsukruk, *Polymer* **2003**, 44, 4557.

[23] J. A. Forrest, K. Dalnoki-Veress, J. R. Dutcher, *Phys. Rev. E* **1997**, 56, 5705.

[24] V. V. Gorbunov, N. Fuchigami, V. V. Tsukruk, *High Perform. Polym.* **2000** 12, 603.

[25] K. Fakao, Y. Miyamoto, *Phys. Rev. E* **2000**, 61, 1743.

[26]J. A. Forrest, J. Mattsson, *Phys. Rev. E* **2000**, 61, R53.

[27] J. L. Lenhart, W. Wu, *Macromolecules* **2002**, 35, 5145.

[28] S. Kawana, R. A. L. Jones, *Phys. Rev. E.* **2001**, 63, 021501.

[29] J. A. Forrest, K. Dalnoki-Veress, J. R. Stevens, J. R. Dutcher, *Phys. Rev. Lett.* **1996**, 77, 2002.

[30] J. L. Keddie, R. A. L. Jones, R. A. Cory, *Faraday Discuss.* **1994**, *98*, 219.

[31] J. J. Zanten, W. E. Wallace, W. Wu, W. *Phys. Rev. E* **1996,** 53, R2053.

[32] C. L. Soles, J. F. Douglas, R. L. Jones, W. Wu, *Macromolecules* **2004**, 37, 2901.

[33] C. K. Ullal, M. Maldovan, M. Wohlgemuth, E. L. Thomas, *J. Opt. Soc. Am. A-Opt. Image Sci. Vis.* **2003**, 20, 948.

[34] G. Binnig, C. F. Quate, C. Gerber, *Phys. Rev. Lett.* **1986,** *56*, 930.

[35] S. Karrasch, R. Hegerl, J. H. Hoh, W. Baumeister, A. Engel, *Proc. Natl. Acad. Sci.* **1994**, *91*, 836.

[36] D. J. Muller, F. A. Schabert, G. Buldt, A. Engel, *Biophys J.* **1995,** *68*, 1681.

[37] J. K. Gimzewski, Ch. Gerber, E. Meyer, R. R. Schlittler, *Chem. Phys. Lett.* **1994**, *217*, 589.

[38] J. Hazel, V. V. Tsukruk, *J. Tribology* **1998***, 120,* 814.

[39] J. L. Hazel, V. V. Tsukruk, *Thin Solid Films* **1999**, *339,* 249.

[40] G. G. Stoney, *Proc. R. Soc. London, Ser. A* **1909**, *82*, 172.

[41] F. J. von Preissig, *J. Appl. Phys.* **1989**, *66*, 4262.

[42] C. A. Klein, *J. Appl.Phys.* **2000**, *88*, 5487.

[43] T. Thundat, R.J. Warmack, G.Y. Chen, D.P. Allison, *Appl. Phys. Lett.* **1994**, *64*, 2894.

[44] R. Berger, H. P. Lang, Ch. Gerber, J. K. Gimzewski, J. H. Fabian, L. Scandella, E. Meyer, H.-J. Güntherodt, *Chem. Phys. Lett.* **1998**, *294*, 363.

[45] T. P. Berg, M. Godin, S. M. Kundsen, W. Shem, G. Carlson, J. S. Foster, K. Babcock, S. R. Manalis, *Nature* **2007**, *446*, 1066.

[46] P.J. Shaver, *Rev. Sci. Instrum.* **1969,** *40*, 901.

[47] S. P. Timoshenko, *J. Opt. Soc. Am.* **1925**, *11*, 233.

[48] J. P. Cleveland, S. Manne, D. Bocek, P.K. Hansma, *Rev. Sci. Instrum.* **1993**, *64*, 403.

[49] T. Bachels, R. Schäfer, *Chem. Phys. Lett.* **1999**, *300*, 177.

[50] T. Bachels, F. Tiefenbacher, R. Schäfer, *J. Chem. Phys.* **1999**, *110*, 10008.

[51]S. Jeon, R. Desikan, F. Tian, T. Thundat, *Appl. Phys. Lett.* **2006**, *88*, 103118.

[52] G.Y. Chen, T. Thundat, E. A. Wachter, R. J. Warmack, *J. Appl. Phys.* **1995,** *77*, 3618.

[53] G. Meyer, N. M. Amer, *Appl. Phys. Lett.* **1988,** *53*, 1045.

[54]H.-P. Lang, M. Hegner, Ch. Gerber, *Mater. Today* **2005**, 30.

[55] H. P. Lang, R. Berger, C. Andreoli, J. Brugger, M. Despont, P. Vettiger, Ch. Gerber, J. K. Gimzewski, J.-P. Ramseyer, E. Meyer, H.-J. Güntherodt, *Appl. Phys. Lett.* **1998**, *72*, 383.

[56] H. J. Mamin, D. Rugar, *Appl. Phys. Lett.* **2001,** *79*, 3358.

[57] D. Rugar, H. J. Mamin, P. Guethner, *Appl. Phys. Lett.* **1989,** *55*, 2588.

[58] P. I. Oden, P. G. Datskos, T. Thundat, R. J. Warmack, *Appl. Phys. Lett.* **1996,** *69*, 3277.

[59] N. Abedinov, P. Grabiec, T. Gotszalk, T. Ivanov, J. Voigt, I. W. Rangelow, J. *Vac. Sci. Technol. A* **2001,** *19*, 2884.

[60] M. Tortonese, R. C. Barrett, C. F. Quate, *Appl. Phys. Lett.* **1996,** *62*, 834.

[61] Q. M. Wang, L. E. Cross, *Ferroelectrics* **1998,** *215*, 187.

[62] S. Zurn, M. Hseih, G. Smith, D. Markus, M. Zang, G. Hughes, Y. Nam, M. Arik, D. Polla, *Smart Mater. Struct.* **2001**, *10,* 252.

[63] J. D. Adams, B. Rogers, L. Manning, Z. Hu, T. Thundat, H. Cavazos, S. C. Minne, *Sens. Actuators A* **2005**, *121*, 457.

[64] C. L. Britton, R. L. Jones, P. I. Oden, Z. Hu, R. J. Warmack, S. F. Smith, W. L. Bryan, J. M. Rochelle, *Ultramicroscopy* **2000,** *82*, 17.

[65] R. Amantea, C. M. Knoedler, F. P. Pantuso, V. K. Patel, D. J. Sauer, J. R. Tower, *Proc. SPIE*, **1997**, *3061*, 210.

[66] G. Shekawat, S.-H. Tark, V. P. Dravid, *Science* **2006**, *311*, 1592.

[67] G. Harsanyi, *Polymer Films in Sensor Applications*, Technomic, Lancaster, **1995**.

[68] I. Tokareva, S. Minko, J. H. Fendler, E. Hutter, *J. Am. Chem. Soc.* **2004**, *126*, 15950.

[69] M. Motornov, R. Sheparovych, R. Lupitskyy, E. MacWilliams, S. Minko, *J. Collod. Interf. Sci.* **2007**, *310*, 481.

[70] K. L. Genson, J. Holzmueller, C. Jiang, J. Xu, J. D. Gibson, E. R. Zubarev, V. V. Tsukruk, *Langmuir* **2006**, *22*, 7011.

[71] Jiang, H. Ko, V. V. Tsukruk, *Adv. Mater.* **2005,** *17*, 2127

[72] C. Jiang, S. Markutsya, V. V. Tsukruk, *Langmuir* **2004**, *20*, 882.

[73] J. Li, H. Möhwald, Z. An, G. Lu, *Soft Matter* **2005**, *1*, 259.

[74] F. Caruso, *Adv. Mater.* **2001**, *13*, 11.

[75] C. Jiang, S. Markutsya, Y. Pikus, V. V. Tsukruk, *Nature Mater.* **2004,** *3*, 721

[76] X. Shi, M. Shen, H. Möhwald, *Prog. Polym. Sci.* **2004**, *29*, 987.

[77] H-L. Zhang, S. D. Evans, J. R. Henderson, R. E. Miles, T-H. Shen *Nanotechnology* **2002**, 13, 439.

[78] D. Li, Y. Jiang, Z. Wu, X. Chen, Y. Li, *Sens. Actuators B.* **2000**, *66*, 125.

[79] A. F. Revzin, K. Sirkir, A. Simonian, M. V. Pishoko, *Sens. Actuators* **2002**, *81*, 359.

[80] S. Myler, S. D. Collyer, K. A. Bridge, S. P. J. Higson, *Biosens. Bioelectron.* **2002**, *17*, 35.

[81] J. Amirola, A. Rodriguez, L. Casaner, J. P. Santos, J. Gutierrez, M. C. Horrillo, *Sens. Actuators B* **2005,** *111-112*, 247.

[82] D. Then, A. Vidic, Ch. Ziegler, *Sens. Actuators B* **2006**, *117*, 1.

[83] F. M. Battiston, J. –P. Ramseyer, H. P. Lang, M. K. Baller, Ch. Gerber, J. K. Gimzewski, E. Meyer, H. –J. Guntherodt, *Sens. Actuators B* **2001**, 77, 122.

[84] B. H. Kim, F. E. Prins, D. P. Kern, S. Raible, U. Weimer, *Sens. Actuators B* **2001**, *78*, 12.

[85] T. A. Betts, C. A. Tipple, M. J. Sepaniak, P. G. Datskos, *Anal. Chim. Acta* **2000,** *422*, 89.

[86] M. Li, H. X. Tang, M. L. Roukes, *Nature Nanotech.* **2007**, *2*, 114.

[87] A. Bietsch, J. Zhang, M. Hegner, H. P. Lang, Ch. Gerber, *Nanotechnology* **2004**, *15*, 873.

[88] M. K. Baller, H. P Lang, J. Fritz, Ch. Gerber, J. K. Gimzewski, U. Drechsler, H. Rothuizen, M. Despont, P. Vettinger, F. M. Battiston, J. P. Ramseyer, P. Fornaro, E. Meyer, H. –J. Guntherodt, *Ultramicroscopy* **2000**, *82*, 1.

[89] F. Lochon, L. Fadel, I. Dufour, D. Rebiere, J. Pistre, *Mater. Sci. Engg. C* **2006,** *26*, 348.

[90] J. Zhao, R. Berger, J. S. Gutmann, *Appl. Phys. Lett.* **2006**, *89*, 033110.

[91] M. C. LeMieux, M. E. McConney, Y. H. Lin, S. Singamaneni, H. Jiang, T. J. Bunning, V. V. Tsukruk, *Nano Lett.* **2006**, *6*, 730.

[92] Y. Zhang, H. –F. Ji, G. M. Brown, T. Thundat, *Anal. Chem.* **2003**, *75*, 4773.

[93] G-G. Bumbu, G. Kircher, M. Wolkenhauer, R. Berger, J. S. Gutmann, *Macomol. Chem. Phys.* **2004**, *205*, 1713.

[94] N. I. Abu-Lail, M. Kaholek, B. LaMattina, R. L. Clark, S. Zauscher, *Sens. Actuators B* **2006**, *114*,

371.

[95] R.Bashir, J. Z. Hilt, O. Eilbol, A. Gupta, N. A. Peppas, *Appl. Phys. Lett.* **2002**, *81*, 3091.

[96] Y. H. Lin, M. E. McConney, M. C. LeMieux, S. Peleshanko, C. Jiang, S. Singamaneni, V. V. Tsukruk, Adv. Mater. **2006**, *18*, 1157.

[97] L. A. Pinnaduwage, T. Thundat, J. E. Hawk, D. L. Hedden, P. F. Britt, E. J. Houser, S. Stepnowski, R. A. McGill, D. Bubb, *Sens. Actuators* B **2004**, *99*, 223.

[98] T. Thundat, G. Y. Chen, R. J. Warmack, D. P. Allison, E. A. Wachter, *Anal. Chem.* **1995**, *67*, 519.

[99] H. Jiang, W. E. Johnson, J. T. Grant, K. Eyink, E. M. Johnson, D. W. Tomlin, T. J. Bunning, *Chem. Mater.* **2003**, *15*, 340.

[100] P. Tamirisa, K. C. Liddell, P. D. Pedrow, M. A. Osman, *J. Appl. Polym. Sci.* **2004**, *93*, 1317.

[101] H. Biederman, *Plasma Polymer Films*, Imperial College Press, London, **2004**.

[102] S. Singamaneni, M. LeMieux, H. Jiang, T. J. Bunning, V. V. Tsukruk, *Chem. Mater.* **2007** *19*, 129.

[103] H. Biederman, Y. Osada, *Plasma Polymerization Processes*, Elsevier Science Publishers B.V , P.O. Box 211, 1000 AE Amsterdam, The Netherlands, **1992**.

[104] J. W. Grate, *Chem. Rev.* **2000,** *100*, 2627.

[105] A. Hierlemann, A. J. Ricco, K. Bodenho, A. Dominik, W. GoÈpel, *Anal. Chem.* **2000**, *72*, 3696.

[106] J. W. Grate, S. J. Patrash, M. H. Abraham, *Anal. Chem.* **1995**, *67*, 2162.

[107] A. R. McGill, M. H. Abraham, J. W. Grate, *Chemtech.* **1994**, *24*, 27.

[108] M. H. Abraham, J. Andonian-Haftvan, C. My Du, V. Diart, G. S. Whiting, J. W. Grate, R. A. McGill, *J. Chem. Soc., Perkin Trans.* **1995**, *2,* 369.

[109] J. W. Grate, M. H. Abraham, *Sens. Actuators B* **1991**, *3*, 85.

[110] T. A. Betts, C. A. Tipple, M. J. Sepaniak, P. G. Datskos, *Anal. Chim. Acta* **2000,** *422*, 89.

[111] F. Lochon, L. Fadel, I. Dufour, D. Rebiere, J. Pistre, *Mater. Sci. Engg. C* **2006,** *26*, 348.

[112] J. Zhao, R. Berger, J. S. Gutmann, *Appl. Phys. Lett.* **2006**, *89*, 033110.

[113] H. Jiang, K. OcNeill, J. T. Grant, S. Tullis, K. Eyink, W. E. Johnson, P. Fleitz, T. J. Bunning, T. J. *Chem. Mater.* **2004**, *16*, 1292.

[114] J. -H. Jang, C. K. Ullal, M. Maldovan, T. Gorishnyy, S. Kooi, C. Y. Koh, E. L. Thomas, E. L., *Adv. Func. Mater.* **2007**, *17*, 3027.

[115] M. Maldovan and E.L. Thomas, *Periodic Materials and Interference Lithography: For Photonics, Phononics and Mechanics*, (Wiley-VCH), **2008**

[116] J. L. Hazel, V. V. Tsukruk, Spring Constants of Composite Ceramic/Gold Cantilevers For Scanning Probe Microscopy, *Thin Solid Films*, **1999**, *339,* 249.

[117] R. M. A. Azzam and N. M. Bashara, *Ellipsometry and Polarized Light*, Elsevier Science Pub Co, **1987**

[118] H. G. Tompkins and W. A. McGahan, *Spectroscopic Ellipsometry and Reflectometry*, John Wiley & Sons Inc, **1999**

[119] H. G. Tompkins and E. A. Irene Eds., *Handbook of Ellipsometry* William Andrews Publications, Norwich, NY, **2005**

[120] www.veeco.com.

[121] B. Ratner, and V. V. Tsukruk, *Scanning Probe Microscopy of Polymers.* B. Ratner, V.V. Tsukruk, Eds.; ACS Symposium Series; American Chemical Society: Washington, D.C., **1998**; Vol. 694.

[122] V.V. Tsukruk, K. Wahl, *Microstructure and Microtribology of Polymer Surfaces.* Tsukruk, V.V.; Wahl, K., Eds. ACS Symposium Series: Washington, D.C., **1999**, Vol. 741.

[123] B. Cappella, G. Dietler, *Surface Science Reports* **1999**, *34*, 1.

[124] MMA Manual from the SEMA Lab

[125] V. V. Tsukruk, V.V. Gorbunov, *Probe Microscopy* **2002,** *3-4*, 241.

[126] J. L. Hazel, V. V. Tsukruk, *Thin Solid Films* **1999**, *339*, 249.

[127] J. L. Hazel, V.V. Tsukruk, *J. Tribol.* **1998**, *120*, 814.

[128] M. Radmacher, R. W. Tillmann, H. E. Gaub, *Biophys. J.* **1993**, *64*, 735.

[129] V. V. Tsukruk, V. V. Gorbunov, *Microsc. Today* **2001**, *1*, 8.

[130] N. Hayazawa, M. Motohashi, Y. Saito, S. Kawata, *Appl. Phys. Lett.* **2005**, *86*, 263114.

[131] H. Ko, Y. Pikus, C. Jiang, A. Jauss, O. Hollricher, V. V. Tsukruk, *Appl. Phys. Lett.* **2004**, *85,* 2598.

[132]Minko, S.; Ed. *Responsive Polymer Materials: Design and Applications;*; Blackwell Publishing: Ames, IA, **2006**.

[133] Bhushan, B., Ed. *Tribology Issues and Opportunities in MEMS*; Kluwer Academic Publishers: Dordrecht, **1997**.

[134] R.C. Advincula, W. J. Brittain, K. C. Caster, J. Ruhe, *Polymer Brushes*.; Wiley: Weinheim, **2004**.

[135] V. V. Tsukruk, *Adv. Mater.* **2001***, 13,* 95.

[136] V. V. Tsukruk, *Prog. Polym. Sci.* **1997**, *22*, 247.

[137] I. Luzinov, S. Minko, V. V. Tsukruk, *Prog. Polym. Sci.* **2004**, *29,* 635.

[138] M. C. LeMieux, S. Minko, D. Usov, M. Stamm, V. V. Tsukruk, *Langmuir* **2003**, *19*, 6126.

[139] D. Julthongpiput, M.C. LeMieux, V. V. Tsukruk, *Polymer* **2003**, *44*, 4557.

[140] J. A. Forrest, K. Dalnoki-Veress, J. R. Dutcher, *Phys. Rev. E* **1997**, *56*, 5705.

[141] V. V. Gorbunov, N. Fuchigami, V.V. Tsukruk, *High Perform. Polym.* **2000** *12*, 603.

[142] K. Fakao, Y. Miyamoto*, Phys. Rev. E* **2000**, *61*, 1743.

[143] J. A. Forrest, J. Mattsson, *Phys. Rev. E* **2000**, *61*, R53.

[144] J. L. Lenhart, W. Wu, *Macromolecules* **2002**, *35*, 5145.

[145] S. Kawana, R. A. L. Jones, *Phys. Rev. E.* **2001**, *63*, 021501.

[146] J. A. Forrest, K. Dalnoki-Veress, J. R. Stevens, J. R. Dutcher, *Phys. Rev. Lett.* **1996**, *77*, 2002.

[147] J. L. Keddie, R. A. L. Jones, R. A. Cory, Faraday Discuss. **1994**, *98*, 219.

[148] J. J. Zanten, W. E. Wallace, W. Wu, Phys. Rev. E **1996,** *53*, R2053.

[149] C. L. Soles, J. F. Douglas, R. L. Jones, W. Wu, Macromolecules **2004**, *37*, 2901.

[150] H. Yasuda, *Plasma Polymerization;* Academic Press,Inc: NewYork, 1985.

[151] P. Bruno, G. Cicala, F. Corsi, A. Dragone, A. M. Losacco, *Sensors and Actuators B* **2004**, *100*, 126.

[152] H. Jiang, W. E. Johnson, J. T. Grant, K. Eyink, E. M. Johnson, D. W. Tomlin, T. J. Bunning, *Chem. Mater.* **2003**, *15*, 340.

[153] J. J. Goodman, *Polym. Sci.* **1960**, *44*, 551.

[154] H. Jiang, K. O'Neill, J. T. Grant, S. Tullis, K. Eyink, W. E. Johnson, P. Fleitz, T. J. Bunning, *Chem. Mater*. **2004**, *16*, 1292.

[155] M. Shen, Y. V. Pan, M. S. Wagner, K. D. Hauch, D. G. Castner, B. D. Ratner, T. A. Horbett, *J. Biomater. Sci.-Polym Ed.* **2001**, *12*, 961.

[156] A. Grill, *Cold Plasma in Materials Fabrication*; IEEE Press, New York, **1994**.

[157] H. Biederman, *Plasma Polymer Films*; Imperial College Press, London, **2004**.

[158] H. Yasuda, T. Hirotsu, *J. Appl. Polym. Sci.* **1977**, *21*, 3179.

[159] H. Yasuda, *Plasma Proc. Poly.* **2005,** *2*, 293.

[160] H. Jiang, W. E. Johnson, J. T. Grant, K. Eyink, E. M. Johnson, D. W. Tomlin, T. J. Bunning, *Chem. Mater.* **2003**, *15*, 340.

[161] G. Socrates, *Infrared and Raman characteristic group frequencies Tables and Charts* 3rd Ed. Wiley, NY, **2001**.

[162] J. Brandrup, E. H. Immergut, E. A. Grulke, (Eds.) *Polymer Handbook*, 4th Ed., Wiley, NY, **1999**.

[163] P. Haaland, P. Targove, *J. Appl. Phys. Lett.,* **1992**, *61*, 34.

[164] V. V. Tsukruk, V. N. Bliznyuk, *Langmuir* **1998**, *14*, 446.

[165] V. V. Tsukruk, *Rubber Chem. Technol.* **1997**, *70*, 430.

[166] M. C. Lemieux, D. Usov, S. Minko, M. Stamm, H. Shulha, V. V. Tsukruk, *Macromolecules* **2003**, *36*, 7244.

[167] G. Socrates, *Infrared and Raman characteristic group frequencies Tables and Charts* 3rd Ed. Wiley, NY, **2001**.

[168] M. Mukherjee, M. Bhattacharya, M. K. Sanyal, Th. Geue, J. Grenzer, U. Pietsch, *Phys. Rev. E* **2002**, *66*, 061801.

[169] J. Thurn, R. F. Cook, *J. Appl. Phys.* **2002**, *91*, 1988.

[170] Z. Cao, X. Zhang, *Sensor. Actuator. A-Phys.* **2006**, *127*, 221.

[171]H. Yasuda, T. Hirotsu, H. G. OLF, *J. Appl. Poly. Sci.* **1977**, *21*, 3179.

[172] Q. S. Yu, H. K. Yasuda, *J. Poly. Sci.: Part A: Poly. Chem.* **1999**, *37*, 1577.

[173] G. K. White, C. L. Choy, *J. Polym. Sci. Polym. Phys. Ed.* **1984**, *22*, 835.

[174] D. J. Lacks, G. C. Rutledge, *Macromolecules* **1995**, *28***,** 1115.

[175] G. Reiter, P. G. de Gennes, *Eur. Phys. J. E*, **2001**, *6*, 25.

[176] M. Ulbricht, *Polymer* **2006**, 47, 2217.

[177] L. J. Gibson and M. F. Ashby, Cellular Solids Structure and Properties, 2nd Ed., Cambridge University Press, Cambridge, **1997**.

[178] V. S. Deshpande, N. A. Fleck, M. F. Ashby, *J. Mech. Phys. Solids.* **2001**, *41*, 1747.

[179] N. Wicks, J. W. Hutchinson, *Int. J. Solids and Struct.* **2001**, *38*, 5165.

[180] V. S. Deshpande, M. F. Ashby, N. A. Fleck, *Acta. Mater.*, **2001**, *49*, 1035.

[181] A.G. Evans, J.W. Hutchinson, N. A. Fleck, M. F. Ashby and H. G. Wadley, *Prog. Mater. Sci.* **2001**, *46*, 309.

[182] S. Yang, G. Chen, M. Megens, C. K. Ullal, Y. J. Han, R. Rapaport, E. L. Thomas, J. Aizenberg, *Adv. Mater.* **2005**, *17*, 435.

[183] M. Scheffler, P. Colombo, Eds. *Cellular Ceramics: Structure, Manufacturing, Properties and Applications*, Wiley, **2005**.

[184] S. Hyun, A. M. Karlsson, S. Torquato, A. G. Evans, *Int. J. Solids. Struct.* 2003, **40**, 6989.

[185] O. D. Velev, E. W. Kaler, *Adv. Mater.* **2000**, *12*, 531.

[186] M. L. Kai Hoa, M. Lu, Y. Zhang, *Adv. Colloid Interface Sci.* **2006**, *121*, 9.

[187] M. E. Leunissen, *Nature* **2005**, *437*, 235.

[188] E. V. Shevchenko, J. Kortright, D. V. Talapin, S. Aloni, A. P. Alivisatos, *Adv. Mater.* **2007**, *19*, 4183.

[189] S. A. Davis, S. L. Burkett, N. H. Mendelson, S. Mann, *Nature* **1997**, *385*, 420.

[190] G. Cook, P. L. Timms, C. G. Spickermann, *Angew Chem Int Ed Engl* **2003**, *42*, 557.

[191] Y.-H. Ha, R. A. Vaia, W. F. Lynn, J. P. Costantino, J. Shin, A. B. Smith, P. T. Matsudaira, E. L. Thomas, *Adv. Mater.* **2004**, *16*, 1091.

[192] J. Y. Huang, X. D. Wang, Z. L. Wang, *Nano Lett.* **2006**, *6*, 2325.

[193] M. Srinivasarao, D. Collings, A. Philips, S. Patel, *Science* **2001** *292*, 79.

[194] D. Zimnitsky, V. V. Shevchenko, V. V. Tsukruk, *Langmuir* **2008**, *24,* 5996.

[195] V. Z.-H. Chan, J. Hoffman, V. Y. Lee, H. Iatrou, A. Avgeropoulos, N. Hadjichristidis, R. D. Miller, E. L. Thomas, *Science* **1999**, *286*, 1716.

[196] J.-H. Jang, C. K. Ullal, M. Maldovan, T. Gorishnyy, S. Kooi, C. Koh, E. L. Thomas, *Adv. Func. Mater.* **2007**, *17*, 3027.

[197] J. H. Moon, J. Ford, S. Yang, *Polym. Adv. Technol.* **2006**, *17*, 83.

[198] J. H. Moon, S. Yang, *J. Macromol. Sci., Polym. Rev.* **2005**, *C45*, 351.

[199] M. Maldovan, C. K. Ullal,W. C. Carter, E. L. Thomas**,** *Nat. Mater.* **2003**, *2*, 664.

[200] C. K. Ullal, M. Maldovan, G. Chen, Y. Han, S. Yang, E. L. Thomas, *Appl. Phys. Lett.* **2004**, *84*, 5434.

[201] D. Mei, B. Cheng, W. Hu, Z. Li, D. Zhang, *Opt. Lett.* **1995**, *20*, 429.

[202] M. Campbell, D. N. Sharp, M. T. Harrison, R. G. Denning, A. J. Turberfield, *Nature* **2000**, *404*, 53.

[203] J.-H. Jang, C. K. Ullal1, T. Gorishnyy, V. V. Tsukruk, E. L. Thomas, *Nano Lett.* **2006**, *6*, 740.

[204] S. Yang, M. Megens, J. Aizenberg, P. Witzius, P. M. Chaikin, W. B. Russell, *Chem. Mater.* **2002**, *14*, 2831.

[205] B. Wagner, H. J. Quenzer, W. Henke, W. Hoppe, W. Pilz, *Sens. Actuators A.* **1995**, *A46*, 89.

[206] T. Mullin, S. Deschanel, K. Bertoldi, M. C. Boyce, *Phys. Rev. Lett.* **2007**, *99*, 084301.

[207] J.-H. Jang, C. K. Ullal, M. Maldovan, T. Gorishnyy, S. Kooi, C. Koh, E. L. Thomas, *Adv. Func. Mater.* **2007**, *17*, 3027.

[208]H. Ko, C. Jiang, V. V. Tsukruk, *Chem. Mater.* **2005**, *17*, 5489.

[209] F. Hua, Y. Sun, A. Gaur, M. A. Meitl, L. Bilhaut, L. Rotkina, J. Wang, P. Geil, M. Shim, J. A. Rogers, *Nano Lett.* **2004**, *4*, 2467.

[210] V. V. Tsukruk, Z. Huang, S. A. Chizhik, V. V. Gorbunov, *J. Mater. Sci.*, **1998**, *33*, 4905.

[211] H. Shulha, A. Kovalev, N. Myshkin, V. V. Tsukruk *Eur. Polym. J.*, **2004**, *40,* 949.

[212] V. V. Tsukruk and Z. Huang, *Polymer*, **2000**, *41*, 5541.

[213] T. Choi, J.-H. Jang, C. K. Ullal, M. C. Lemieux, V. V. Tsukruk, and E. L. Thomas, *Adv. Funct. Mater.*, **2006**, *16*, 1324.

[214] V. V. Tsukruk, V. V. Gorbunov, Z. Huang, S. A. Chizhik, *Polym. Int.*, **2000**, ***49***, 441.

[215] A. Kovalev, H. Shulha, M. LeMieux, N. Myshkin, V. V. Tsukruk, *J. Mater. Res.* **2004**, *19*, 716.

[216] S. Sarva, A.D. Mulliken, M.C. Boyce, *J. Phys. IV France*, **2006**, *134*, 95.

[217] R. Feng and R. J. Farris, *J. Mater. Sci.*, **2002**, *37*, 4793.

[218] R. V. Lewis, *Chem. Rev.,* **2006**, *106*, 3762.

[219] C. Jiang, X. Wang, R. Gunawidjaja, Y.-H. Lin, M. K. Gupta, D. L. Kaplan, R. R. Naik, V. V. Tsukruk, *Adv. Func. Mater.*, **2007**, *17*, 2229.

[220] J.-H. Jang, C. K. Ullal, T. Choi, M. C. Lemieux, V. V. Tsukruk, E. L. Thomas, *Adv. Mater.*, **2006**, *18*, 2123.

[221] L. H. Sperling, *Polymeric Multicomponent Materials*, John Wiley & Sons, Inc., New York, **1997**.

[222] M. Nordström, R. Marie, M. Calleja, A. Boisen, *J. Micromech. Microeng.*, **2004**, *14*, 1614.

[223] A. Kovalev, H. Shulha, M. Lemieux, N. Myshkin, V. V. Tsukruk, *J. Mater. Res.* **2004**, *19*, 716.

[224] A. S. Argon, R. E. Cohen, O. S. Gebizlioglu, C. E. Schwier, *Adv. Polym. Sci.*, **1983**, *52-3*, 275.

[225] N. Bowden, S. Brittain, A. G. Evans, J. W. Hutchinson, G. M. Whitesides *Nature* **1998,** *393*, 146.

[226] K. Efimenko, M. Rackaitis, E. Manias, A. Vaziri, L. Mahadevan, J. Genzer, *Nat. Mater.* **2005**, *4*, 293.

[227] L. Mahadevan, S. Rica, *Science* **2005**, *307*, 1740.

[228] J. Hiller, J. D. Mendelsohn, M. F. Rubner, *Nature Mater.* **2002**, *1*, 59.

[229] C. M. Stafford, C. Harrison, K. L. Beers, A. Karim, E. J. Amis, M. R. Vanlandingham, H.-C. Kim, W. Volksen, R. D. Miller, E. E. Simonyi, *Nature Mater.* **2004**, *3*, 545.

[230] C. Jiang, S. Singamaneni, E. Merrick, V. V. Tsukruk, *Nano Lett.* **2006**, *6*, 2254.

[231] Y. Sun, W. M. Chi, H. Jiang, Y. Y. Huang, J. A. Rogers, *Nature Nanotechnol.* **2006**, *1*, 201.

[232] R. Gunawidjaja, H. Ko, C. Jiang, V. V. Tsukruk, *Chem. Mater.* **2007**, *19,* 2007.

[233] D.-Y. Khang, J. Xiao, C. Kocabas, S. MacLaren, T. Banks, H. Jiang, Y. Y. Huang, J. A. Rogers, *Nano Lett.* **2008**, *8*, 124.

[234] J. Huang, M. Juszkiewicz, W. H. de Jeu, E. Cerda, T. Emrick, N. Menon, T. P. Russell *Science* **2007**, *317*, 650.

[235] K. Bertoldi, M. C. Boyce, S. Deschanel, S. M. Prange, T. Mullin, *J. Mech. Phys. Solid.* **2008**, 56, 2642.

[236] J.-T. Chen, M. Zhang, T. P. Russell, *Nano Lett.* **2007**, *7*, 183.

[237] E. P. Chan, E. J. Smith, R. C. Hayward, A. J. Crosby, *Adv. Mater.* **2008**, *20*, 711.

[238] P. Lin, S. Vajpayee, A. Jagota, C.-H. Hui, S. Yang**,** *Soft Matter*, **2008**, *4*, 1830.

[239] Y. Sun, and J. A. Rogers, *J. Mater. Chem.* **2007**, *17*, 832.

[240] Y. Sun, W. M. Choi, H. Jiang, Y. Y. Huang, J. A. Rogers, *Nat. Nanotech.* **2006**, *1*, 201.

[241] P. J. Yoo, K. Y. Suh, S. Y. Park, H. H. Lee, *Adv. Mater.* **2002**, *14*, 1383.

[242] M.-W. Moon, S. H. Lee, J.-Y. Sun, K. H. Oh, A. Vaziri, J. W. Hutchinson, *Proc. Natl. Acad. Sci.* **2007**, *104*, 1130.

[243] M. Campbell, D. N. Sharp, M. T. Harrison, R. G. Denning, A. J. Turberfield, *Nature* **2000**, *404***,** 53.

[244] S. John, *Phys. Rev. Lett.* **1987**, *58*, 2486.

[245] M. Ulbricht, *Polymer* **2006**, *47*, 2217.

[246] M. Théry, V. Racine, A. Pépin, M. Piel, Y. Chen, J.-B. Sibarita, M. Bornens, *Nature Cell Biol.* **2005**, *7*, 947.

[247] J.-H. Jang, C. K. Ullal, T. Gorishnyy, V. V. Tsukruk, E. L. Thomas, *Nano Lett.* **2006**, *6*, 740

[248] S. Hollister, *Nat. Mater.* **2005**, *4*, 518.

[249] X. Zhu, Y. Zhang, D. Chandra, S.-C. Cheng, J. M. Kikkawa, S. Yang**,** *Appl. Phys. Lett.* , **2008** , *93*, 161911.

[250] J. Genzer, J. Groenewold, *Soft Matt.* **2006**, *2*, 310.

[251] T. Mullin, S. Deschanel, K. Bertoldi, M. Boyce, *Phys. Rev. Lett.* **2007**, *99*, 084301.

[252] K. Bertoldi, M.C. Boyce, *Phys. Rev. B.* **2008**, *77*, 052105.

[253] S. Singamaneni, S. Chang, J.-H. Jang, W. Davis, E. L. Thomas, V. V. Tsukruk, *Phys. Chem. Chem. Phys.* **2008**, *10*, 4093.

[254] Y. Zhang, E. A. Matsumoto, A. Peter, P.-C. Lin, R. D. Kamien, S. Yang*, Nano Lett.* **2008**, 8, 1192.

[255] S. Singamaneni, K. Bertoldi, S. Chang, J.-H. Jang, E. L. Thomas, M. Boyce, V. V. Tsukruk, *ACS Appl. Mater. Interfaces*, in print

[256] J. H. Moon, S. Yang, *J. Macromol. Sci., Part C: Polym. Rev.* **2005** , *45*, 351.

[257] M. Nordström, R. Marie, M. Calleja, A. Boisen, *J. Micromech. Microeng.* **2004**, *14*, 1614.

[258] M. Danielsson, D. M. Parks, M.C. Boyce, *J. Mech. Phys. Solids.* **2002**, *50*, 351.

[259] C.-Y. Wen, W. S. Kim, and E. L. Thomas, *Adv. Mater.* **2008**., submitted.

[260] L. Wang, M. C. Boyce, C.-Y. Wen, E. L. Thomas, *Adv. Mater.* **2008**, submitted.

[261] V.V. Tsukruk, *Rubber Chem. Tech.* **1997**, *70*, 430.

[262] V.V. Tsukruk, D. H. Reneker, *Polymer* **1995**, *36*, 1791.

[263] C. K. Ullal, M. Maldovan, E. L. Thomas, G. Chen, Y.-J. Han, S. Yang, *Appl. Phys. Lett.* **2004**, 84, 5434.

[264] J.-H. Jang, C. K. Ullal, M. Maldovan, T. Gorishnyy, S. Kooi, C. Koh, E. L. Thomas, *Adv. Func. Mater.* **2007**, *17*, 3027.

[265] J. H. Moon, J. Ford, S. Yang, *Polym. Adv. Technol.* **2006**, *17*, 83.

[266] M. Maldovan, C. K. Ullal, W. C. Carter, E. L. Thomas, *Nature Mater.* **2003**, *2*, 664.

[267] T. Choi, J.–H. Jang, C. K. Ullal, M. C. Lemieux, V. V. Tsukruk, E. L. Thomas, *Adv. Func. Mater.* **2006**, *16*, 1324.

[268] J.-H. Jang, C. K. Ullal, T. Choi, M. C. Lemieux, V. V. Tsukruk, E. L. Thomas,, *Adv. Mater.* **2006,** *18,* 2123

[269] Y. Wang, M. Bachman, C. E. Sims, G. P. Li, N. L. Allbritton, *Langmuir* **2006,** *22,* 2719.

[270] N. Triantafyllidis, M. D. Nestorovic, M. W. Schraad, *Jnt. Appl. Mechanics* **2006**, *73*, 505.

[271] C.Jiang, H. Ko, V. V. Tsukruk, *Adv. Mater.* **2005**, *17,* 2127.

[272] G. Socrates, *Infrared and Raman characteristic group frequencies Tables and Charts* 3rd Ed. Wiley, NY (**2001**).

[273] Y.-T. Chen, D. Lee, *J. Micromech. Microeng.* **2007**, *17*, 1978.

[274] K. Y. Suh, Y. S. Kim, H. H. Lee, *Adv. Mater.* **2001**, *13*, 1386.

[275] H. Ko, C. Jiang, V. V. Tsukruk, *Chem. Mater.* **2005**, *17*, 5489.

[276] J. W. Grate, *Chem. Rev.* **2000**, *100***,** 2627.

[277] Z. M. Rittersma, *Sens. Actuators A* **2002,** *96,* 196.

[278] H. P. Penman, *Humidity,* Chapman and Hall, London, **1955**.

[279] Q. A. Shams, C. G. Burkett Jr., T. S. Daniels, G. Tsoucalas, T. Comeaux, B. S. Sealey, M. L. Fox, *NASA Report,* TP-213770, **2005**.

[280] H. Shibata, M. Ito, M. Asakursa, K. Watanabe, *IEEE Trans. Instrum. Meas.* **1996**, *45,* 564.

[281] C. Laville, C. Pellet, *IEEE Sens. J.* **2002,** *2,* 96.

[282] Z. Chen, C. Liu, *Sens. Lett.* **2005,** *3,* 274.

[283] A. Wu, M. J. Brett, *Sens. Mater.* **2001**, *13,* 399.

[284] J. Salonen, J. Tuura, M. Bjorkqvist, V.P. Lehto, *Sens. Actuators B* **2006,** *114*, 423.

[285] B. Bruno, G. Cicala, F. Corsi, A. Dragone, A. M. Losacco, *Sens. Actuators B* **2004,** *100*, 126.

[286] M. C. LeMieux, M. McConney, Y.-H. Lin, S. Singamaneni, H. Jiang, T.J. Bunning, V. V. Tsukruk *Nano Lett.* **2006**, *6*, 730.

[287] Y. Zhang, H.-F. Ji, G. M. Brown, T. Thundat, *Anal. Chem.* **2003,** *75,* 4773.

[288] H. Yasuda, *Plasma Polymerization,* Academic Press, Inc, NewYork, **1985**.

[289] H. Jiang, W. E. Johnson, J. T. Grant, K. Eyink, E. M. Johnson, D. W. Tomlin, T. J. Bunning, *Chem. Mater.* **2003,** *15,* 340.

[290] H. Jiang, K. O'Neill, J. T. Grant, S. Tullis, K. Eyink, W. E. Johnson, P. Fleitz, T. J. Bunning, *Chem. Mater*. **2004,** *16,* 1292.

[291] I. Luzinov, S. Minko, V. V. Tsukruk, *Prog. Polym. Sci.* **2004,** *29,* 635.

[292] V. V. Tsukruk, *Prog. Polym. Sci.* **1997,** *22,* 247.

[293] S. Singamaneni, M. C. LeMieux, H. Jiang, T. J. Bunning, V. V. Tsukruk, *Chem. Mater*. **2007,** *19,* 129.

[294] J. Mertens, M. Calleja, D. Ramos, A. Taryn, J. Tamayo, *J. Appl. Phys.* **2007**, *101*, 034904.

[295] S. A. Chizhik, Z. Huang, V. V. Gorbunov, N. K. Myshkin, V. V. Tsukruk, *Langmuir* **1998,** *14,* 2606.

[296] K. Kamagata, M. Toyama, *J. Appl. Polym. Sci.* **1974,** *18,* 167.

[297] J. T. Grant, H. Jiang, S. Tullis, W. E. Johnson, K. Eyink, P. Fleitz, T. J. Bunning, *Vacuum* **2005,** *80,* 12.

[298] F. M. Battiston, J. -P. Ramseyer, H. P. Lang, M. K. Baller, Ch. Gerber, J. K. Gimzewski, E. Meyer, H. -J. Güntherodt, *Sens. Actuators B* **2001,** *77,* 122.

[299] S. Jeon, R. Desikan, F. Tian, T. Thundat, *Appl. Phys. Lett.* **2006,** *88,* 103118.

[300] R. Raiteri, H.-J. Butt, M. Grattarola, *Scanning Microscopy* **1998,** *12,* 243.

[301] L. R. Fisher, R. A. Gamble, J. Middlehurst, *Nature* **1981,** *290,* 575.

[302] J. Chen, I. De Wolf, *Semicond. Sci. Technol.* **2003**, *18,* 261.

[303] D. W. Dareing, T. Thundat, *J. Appl. Phys.* **2005,** *97,* 043526.

[304] *Structural Mechanics Module Model User's Guide for COMSOL Multiphysics 3.2*; COMSOL AB, Stockholm, Sweden, **2004**.

[305] R. Berger, Y. Cheng, R. Fo¨rch, B. Gotsmann, J. S. Gutmann, T.Pakula, U. Rietzler, W. Scha¨rtl, M. Schmidt, A. Strack, J. Windeln, H.-J. Butt, *Langmuir* **2007,** *23,* 3150.

[306] L. A. Pinnaduwage, H.-F. Ji, T. Thundat, *IEEE Sensors J.* **2005,** *5,* 774.

[307] H. J. Butt, M. Jaschke, W. Ducker, *Bioelectrochem. Bioenerg.* **1995,** *38,* 191.

[308] T. Thundat, G. Y. Chen, R. J. Warmack, D. P. Allison, E. A. Wachter, *Anal. Chem.* **1995,** *67,* 519.

[309] H. F. Ji, R. Dabestani, T. G. Thundat, G. M. Gilbert, P. F. Britt, *Chem. Commun.* **2000,** *6,* 457.

[310] C. A. Tipple, N. V. Lavrik, M. Culha, J. Headrick, P. Datskos, M. J. Sepaniak, *Anal. Chem.* **2002,** *74*, 3118.

[311] D. R. Baselt, G. U. Lee, K. M. Hansen, L. A. Chrisey, R. J. A. Colton, *Proc. IEEE* **1997,** *85,* 672.

[312] N. I. Abu-Lail, M. Kaholek, B. LaMattina, R. L. Clark, S. Zauscher, *Sens. Actuators B* **2006,** *114***,** 371.

[313] Y. Yang, H.-F. Ji, T. Thundat, *J. Am. Chem. Soc.* **2003,** *125,* 1124.

[314] Y. Lam, N. I. Abu-Lail, M. S. Alam, S. Zauscher, *Nanomedicine: Nanotech. Biol & Med* **2006**, *2,* 222.

[315] G. Bumbu, M. Wolkenhauer, G. Kircher, J. S. Gutmann, R. Berger, *Langmuir* **2007,** *23*, 2203.

[316] S. Igarashi, A. N. Itakura, M. Toda, M. Kitajima, L. Chu, A. N. Chifen, R. Förch, R. Berger, *Sens. Actuators B* **2006,** *117,* 43.

[317] M. K. Baller, H. P. Lang, J. Fritz, Ch. Gerber, J. K. Gimzewski, U. Drechsler, H. Rothuizen, M. Despont, P. Vettiger, F. M. Battiston, J. P. Ramseyer, P. Fornaro, E. Meyer, H.-J. Güntherodt, *Ultramicroscopy*, **2000,** *82,* 1.

[318] Y-H. Lin, M. McConney, M. LeMieux, S. Peleshanko, C. Jiang, S. Singamaneni, V. V. Tsukruk, *Adv. Mater*. **2006,** *18,* 1157.

[319] J. K. Gimzewski, Ch. Gerber, E. Meyer, R. R. Schlittler, *Chem. Phys. Lett.* **1994,** *217,* 589.

[320] J. R. Barnes, R. J. Stephenson, M. E. Welland, Ch. Gerber, J. K. Gimzewski, *Nature* **1994, 372**, 79.

[321] R. Berger, E. Delamarche, H. P. Lang, Ch. Gerber, J. K. Gimzewski, E. Meyer, H.-J. Güntherodt, *Science* **1997,** *276,* 2021.

[322] T. Thundat, E. A. Wachter, S. L. Sharp, R. J. Warmack, *Appl. Phys. Lett.* **1995,** *66,* 1695.

[323] H. P. Lang, M. K. Baller, R. Berger, Ch. Gerber, J. K. Gimzewski, F. M. Battiston, P. Fornaro, J. P. Ramseyer, E. Meyer, H.-J. Güntherodt, *Anal. Chim. Acta* **1999**, *393*, 59.

[324] D. R. Baselt, B. Fruhberger, E. Klaassen, S. Cemalovic, C. L. Britton, S. V. Patel, T. E. Mlsna, D. McCorkle, B. Warmack, *Sens. Actuators B* **2003,** *88*, 120.

[325] B. C. Fagan, C. A. Tipple, Z. Xue, M. J. Sepaniak, P. G. Datskos, *Talanta* **2000,** *53,* 599.

[326] B. Yang, B. Aksak, Q. Lin, M. Sitti, *Sens. Actuators B* **2006,** *114*, 254.

[327] P. A. Tamirisa, D. W. Hess, *Macromolecules* **2006**, *39,* 7092.

[328] R. J. Colton, J. N. Russell, *Science* **2003,** *299***,** 1324.

[329] D. Ellis, M. R. Zakin, L. S. Bernstein, M. F. Rubner, *Anal. Chem.* **1996,** *68*, 817.

[330] S. W. Thomas III, T. M. Swager, *Adv. Mater.* **2006,** *18*, 1047.

[331] S. Virji, R. B. Kaner, B. H. Weiller, *Chem. Mater.* **2005,** *17,* 1256.

[332] D. V. Talapin, C. B. Murray, *Science* **2005,** *310*, 86.

[333] J. W. Gardner, P. N. Bartlett, *Electronic Noses,* OUP Press, Oxford, **1999**.

[334] A. J. Ricco, R. M. Crooks, G. C. Osbourn, *Acc. Chem. Res.* **1998,** *31,* 289.

VITA

SRIKANTH SINGAMANENI

Srikanth Singamaneni was born in Jammulapalem in Andhra Pradesh, India on April 9, 1981 to Venkateswarlu and Padma. He and his brother Sridhar grew up in Bapatla, a nearby town. He attended Bapatla Public School from 1st grade to 12th grade. He got a Bachelor degree in Electronics and Communication Engineering from Bapatla Engineering College in 2002. He received his M.S. degree (2004) in Electrical Engineering from Western Michigan University. He pursued a Ph.D. in Polymer Materials Science and Engineering at Georgia Institute of Technology with Prof. Vladimir V. Tsukruk. Sandhya Jetti (daughter of Krishna and Indumathi) and Srikanth were married on August 6th 2006 in Bapatla. After graduating, Srikanth will begin as an assistant professor in the Department of Mechanical, Aerospace and Structural Engineering at Washington University in St. Louis.